ESC-TR-92-132

Technical Report
966

The Application of Synthetic-Beacon Technology to Astronomy

R.R. Parenti
R.J. Sasiela

17 March 1993

Lincoln Laboratory
MASSACHUSETTS INSTITUTE OF TECHNOLOGY
LEXINGTON, MASSACHUSETTS

Prepared for the Department of the Air Force
under Contract F19628-90-C-0002.

This report is based on studies performed at Lincoln Laboratory, a center for research operated by Massachusetts Institute of Technology. The work was sponsored by the Department of the Air Force under Contract F19628-90-C-0002.

The ESC Public Affairs Office has reviewed this report, and it is releasable to the National Technical Information Service, where it will be available to the general public, including foreign nationals.

This report may be reproduced to satisfy needs of U.S. Government agencies.

FOR THE COMMANDER

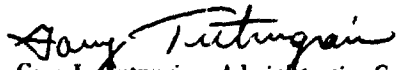

Gary L. Tutungian, Administrative Contracting Officer,
Directorate of Contracted Support Management

Non-Lincoln Recipients

PLEASE DO NOT RETURN

Permission is given to destroy this document when it is no longer needed.

MASSACHUSETTS INSTITUTE OF TECHNOLOGY
LINCOLN LABORATORY

THE APPLICATION OF SYNTHETIC-BEACON TECHNOLOGY TO ASTRONOMY

R.R. PARENTI
R.J. SASIELA
Group 54

TECHNICAL REPORT 966

17 MARCH 1993

LEXINGTON MASSACHUSETTS

EXECUTIVE SUMMARY

Introduction

The application of adaptive optics technology to laser-beam control has been under investigation within the military community since the early 1970s. This work has encompassed a wide range of theoretical investigations as well as an impressive suite of laboratory and field experiments. During this period a number of real-time systems incorporating several hundred degrees of freedom have been built and tested, and the technology to extend this number by at least an order of magnitude is now under development.

To exploit adaptive-optics concepts in the construction of astronomical telescopes, the budgetary restrictions under which this field of research operates must be considered and improvements in system performance must be carefully balanced against equipment complexity, reliability, and cost. To accomplish this design trade-off, a set of concise analytic models describing the essential properties of a laser guide-star phase-conjugation system has been assembled. With the aid of these models, an optimization strategy for mating adaptive optics to a 4-m-class optical telescope has been developed; research shows that such a system might be expected to improve the effective atmospheric seeing conditions by nearly a factor of 10 within the isoplanatic patch of the turbulence probe.

The Laser Guide-Star Concept

Few celestial objects are bright enough to permit accurate wavefront measurements by a phase sensor. A solution to this problem was first discovered in the early 1980s by investigators in the high-energy laser-beam-control community. The technique involves the use of a pulsed laser beam that is projected along the path to the target object; backscatter generated by molecules and particulates in the atmosphere provides a synthetic probe, which can be used to obtain reliable turbulence measurements. The quality of the data provided by this type of source is strongly affected by the altitude of the beacon and the size of the collection aperture. Residual phase errors due to focal anisoplanatism (which is related to the difference in range between the synthetic beacon and the target object) and offset anisoplanatism (which arises from the need to obtain tracking information from a bright neighboring star) represent driving factors in the overall performance of the adaptive-optics system.

An Analytical Treatment of Atmospheric Turbulence

To a large extent, the success of this investigation can be attributed to the extensive use of a new analytic model that accurately describes the principal anisoplanatic effects. This formulation incorporates the Rytov approximation (appropriate for slowly varying turbulence and low scintillation) in the development of integral expressions for the aperture-average phase error. In the most general case, the solution requires a six-fold integration, but four of these integrals are easily performed using standard mathematical techniques. Of the two remaining integrals, which involve the transverse spatial spectrum and the propagation path, the first is performed using an innovative approach that applies Mellin-transform theory. For most problems of interest, the final solution can be expressed as a rapidly converging series

expansion that incorporates the turbulence moments. A brief description of the approach and derivations of the most important phase-error formulas can be found in Appendix A.

An Optimized Design for Guide-Star Systems

For an adaptive-optics system to be useful in astronomical investigations, a significant improvement in resolution (in excess of a factor of 2) must be achieved over a large fraction of the nighttime sky. A series of computer simulations in which the quality of the phase correction was varied has determined that the high-spatial-frequency (figure) component of the phase error can be no more than 3 rad^2 if this goal is to be achieved. If this criterion is satisfied, the effective resolution of a long-exposure image will be determined by tracking jitter, which in most cases is dominated by anisoplanatic errors related to the angular offset between the target object and the tracking star. Therefore, resolution and sky coverage are intimately related; an improvement in one of these factors can only be achieved to the detriment of the other.

Figure ES-1 illustrates the relationship between achievable resolution and fractional sky coverage. Although it is theoretically possible to build an adaptive-optics system that provides a tenfold improvement in the resolution of a 4-m telescope operating in the visible, the probability of finding a suitable tracking star to maintain the requisite tilt jitter is predicted to be only 1 percent. On the other hand, a factor-of-4 improvement can be attained with near-unity probability. As discussed in Section 4, such a system would require approximately 300 actuators operating at a correction bandwidth of 20 Hz and a beacon laser capable of maintaining an average power level of 50 W.

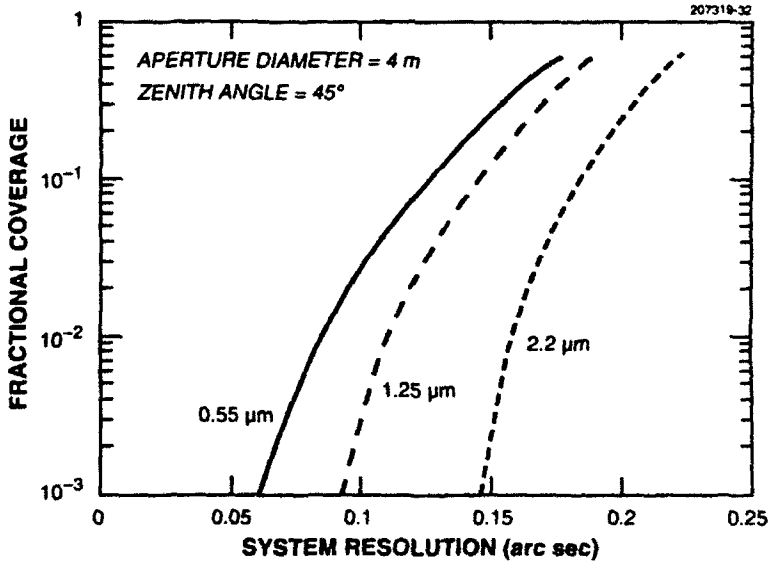

Figure ES-1. The fraction of the sky over which a given resolution can be attained for a laser guide-star compensation system. Effects of residual image motion due to finite tracker bandwidth, limited signal, and offset anisoplanatism have been included. The uncorrected seeing at 0.55 μm is 0.85 arc sec for the atmospheric conditions used in this study.

ACKNOWLEDGMENTS

This work is the culmination of a lengthy investigation, during which the assistance of several individuals proved to be invaluable. We are particularly grateful to Daniel Murphy and Byron Zollars for supplying the experimental data that appears in this report. We would also like to thank Robert Kramer for contributing to the development of the servo system model, and Jan Herrmann for his frequent involvement in discussions of anisoplanatic effects. Finally, we wish to express our gratitude to Charles Primmerman and Darryl Greenwood for their constant encouragement and support.

TABLE OF CONTENTS

TABLE OF CONTENTS (Continued)

LIST OF ILLUSTRATIONS

LIST OF ILLUSTRATIONS (Continued)

LIST OF TABLES

1. INTRODUCTION

The application of adaptive optics to laser-beam control problems has been under investigation within the military community since the early 1970s. This work has encompassed a wide range of theoretical investigations as well as an impressive suite of laboratory and field experiments. During this period a number of real-time systems incorporating several hundred degrees of freedom have been built and tested, and the technology to extend this number by at least an order of magnitude is now under development.

The designers of laser-propagation systems are frequently concerned with uncooperative-target engagements in which the target return is either too weak or improperly positioned to be used effectively as a turbulence probe. A potential solution, which involves the use of backscatter from laser beams focused in the atmosphere, was first proposed to the defense community by Feinleib in 1982 [1] and later independently published by Foy and Labeyrie in 1985 [2]. Since that time, a number of alternative schemes have been considered to achieve near-diffraction-limited beam profiles; these schemes include arrays of low-altitude sources and high-altitude beacons formed within the earth's sodium layer.

This report presents an overview of a body of theoretical work that has been the foundation for several laser guide-star experiments conducted by Lincoln Laboratory [3–5]. Although the original intent of this investigation was to develop a means to propagate near-diffraction-limited laser beams through the atmosphere, recent changes in classification guidelines have made it possible to apply these techniques to ground-based astronomical telescopes. In keeping with the original emphasis on near-perfect turbulence compensation for short wavelengths and marginal seeing conditions, however, the actuator densities and correction bandwidths discussed are generally much higher than those recommended by other authors [6].

To lay the proper groundwork for the design guidelines presented at the end of this report, it is necessary to first review the inherent limitations of the phase-conjugation process and justify the need for synthetic-beacon turbulence probes. Section 2 of this report concentrates on conventional adaptive-optics systems; in this context, the term "conventional" refers to systems having access to a real beacon located within the isoplanatic patch of the target object. Section 2 also introduces the turbulence- and wind-profile models that are the basis for all the numerical calculations that follow. The isoplanatic errors associated with the deployment of synthetic beacons are the main topic of Section 3, where a brief comparison of single- and multiple-beacon geometries is also presented.

The main thrust of this investigation is presented in Section 4, in which a methodology is proposed for balancing the major sources of compensation error to optimize the performance of an adaptive-optics system. Recognizing that constructs exploiting natural-star beacon illumination are highly desirable from a cost perspective, Section 4 contains a quantitative discussion of fractional sky coverage for both natural- and synthetic-beacon systems. In conclusion, significant benefits accrue with the use of laser guide stars, but the development of more compact and less expensive laser sources will be necessary before this approach becomes practical for widespread application.

2. FUNDAMENTAL CONCEPTS

To avoid ambiguity in the systems analyses that follow, a brief discussion of some of the more important turbulence issues is given in this section. Of particular interest is the treatment of Strehl ratio (on-axis intensity relative to a diffraction-limited image) and resolution for systems capable of partial phase compensation.

2.1 STATISTICAL DESCRIPTION OF ATMOSPHERIC TURBULENCE

A quantitative treatment of optical turbulence usually begins with a statistical description of the index of refraction. A useful quantity is the structure function, which represents the expected variance in refractive index between two points

$$D_n \equiv \left\langle \left(n(\vec{r}_1) - n(\vec{r}_2) \right)^2 \right\rangle \quad , \tag{2-1}$$

where $\vec{r}_1$ and $\vec{r}_2$ are three-dimensional vectors. Kolmogorov [7] has shown that in the inertial subrange this function is isotropic and proportional to the 2/3 power of the scalar distance, r;

$$D_n(r) = C_n^2(h)\, r^{2/3} \quad . \tag{2-2}$$

The C_n^2 parameter characterizes the strength of the refractive index fluctuations as a function of the altitude, h. From this expression, Fried [8] derived the form of the phase structure function at the surface of a collection aperture

$$D_\phi(r) = 2.91\, k^2\, r^{5/3} \sec(\zeta) \int C_n^2(h)\, dh \quad , \tag{2-3}$$

where $k = 2\pi/\lambda$ is the optical wavenumber, ζ is the zenith angle, and the integral is performed over the beam path. (MKS units have been assumed in computing the leading constant.) Fried found it convenient to define a turbulence coherence length, r_0, over which the gross wavefront distortion can be described as a uniform tilt. Thus,

$$D_\phi(r) = 6.88 \left(r / r_0 \right)^{5/3} \quad , \tag{2-4}$$

where

$$r_0 = \left\{ 0.423 k^2 \sec(\zeta) \int C_n^2(h)\, dh \right\}^{-3/5} \quad . \tag{2-5}$$

An aperture of dimension r_0 will produce a nearly diffraction-limited far-field image that will appear to change position as the atmosphere evolves with time. This parameter establishes the critical spatial dimension of a subaperture, within which a unique phase error can be measured and subsequently corrected by the movement of a single mechanical actuator.

2.2 TURBULENCE AND WIND-VELOCITY MOMENTS

Turbulence calculations make widespread use of turbulence-profile integrals of the type indicated in Equation (2-3). The n^{th} moment is defined in the following manner:

$$\mu_n = \int C_n^2(h) h^n \, dh \quad , \tag{2-6}$$

where the integral is taken over the entire turbulence region. The low-order moments are most sensitive to ground-level turbulence, whereas the high-order moments are more heavily influenced by upper-altitude turbulence. Using this notation, the expression for the coherence length would be

$$r_0 = \left\{0.423 k^2 \sec(\zeta) \mu_0\right\}^{-3/5} \quad . \tag{2-5'}$$

The isoplanatic patch, which defines the angle within which the distortion over the turbulence path will be essentially unchanged, can be shown to depend on the 5/3 moment

$$\theta_0 = \left\{2.91 k^2 \sec^{8/3}(\zeta) \int C_n^2(h) h^{5/3} \, dh\right\}^{-3/5} = \left\{2.91 k^2 \sec^{8/3}(\zeta) \, \mu_{5/3}\right\}^{-3/5} \quad . \tag{2-7}$$

The temporal characteristics of turbulence-induced phase perturbations are often modeled on the assumption that turbulence can be described as a set of frozen layers, each of which moves across the aperture at speeds that vary as a function of altitude. For simplicity, the direction of motion is assumed to be perpendicular to the plane containing the zenith angle. The velocity moments have the following form:

$$v_n = \int C_n^2(h) \, v^n(h) \, dh \quad , \tag{2-8}$$

where $v(h)$ is the wind-velocity function. A critical time constant specifying the interval over which turbulence remains essentially unchanged derives from Greenwood [9], and can be expressed as a function of the 5/3 velocity moment

$$\tau_0 = \left\{2.91 k^2 \sec(\zeta) \int C_n^2(h) v^{5/3}(h) \, dh\right\}^{-3/5} = \left\{2.91 k^2 \sec(\zeta) \, v_{5/3}\right\}^{-3/5} \quad . \tag{2-9}$$

To attach numerical values to these critical system parameters, baseline profiles must be established for turbulence and wind velocity. During the past two decades, several dozen models have been developed in an attempt to describe refractive-index measurements made at a variety of locations throughout the world. For daytime conditions at inland sites, the SLC-Day (standardized under the Submarine-Laser Communications program) and the Hufnagel-Valley turbulence models are frequently used for systems analysis. [See Equations (C-1) and (C-2) in Appendix C.] To the best of our knowledge, however, there are no standard turbulence profiles for good astronomical sites and nighttime viewing conditions where the seeing, defined as

$$\theta_{\text{seeing}} = 1.22 \frac{\lambda}{r_0} \quad , \tag{2-10}$$

is often better than 0.5 arc-seconds [10]. Therefore, the authors have elected to assemble a modified version of the Hufnagel-Valley profile that yields a 20-cm r_0 and a 20-μrad θ_0 for 0.55 μm radiation at zenith

$$C_n^2(h) = 8.16\times10^{-54}\, h^{10} \exp(-h/1000) + 3.02\times10^{-17} \exp(-h/1500) + 1.90\times10^{-15} \exp(-h/100) \tag{2-11}$$

Note that the altitude is given in meters and the units of C_n^2 are $m^{-2/3}$.

Temporal fluctuations in the cumulative phase distortion are somewhat less critical to this analysis; therefore, for the wind profile a standard form proposed by Bufton is used:

$$v(h) = 5 + 30 \exp\left\{-\left[(h-9400)/4800\right]^2\right\} . \tag{2-12}$$

The units for this expression are m/sec.

The turbulence and wind models are plotted as a function of altitude in Figures 1 and 2, respectively. A comparison of key turbulence parameters can be found in Table 1.

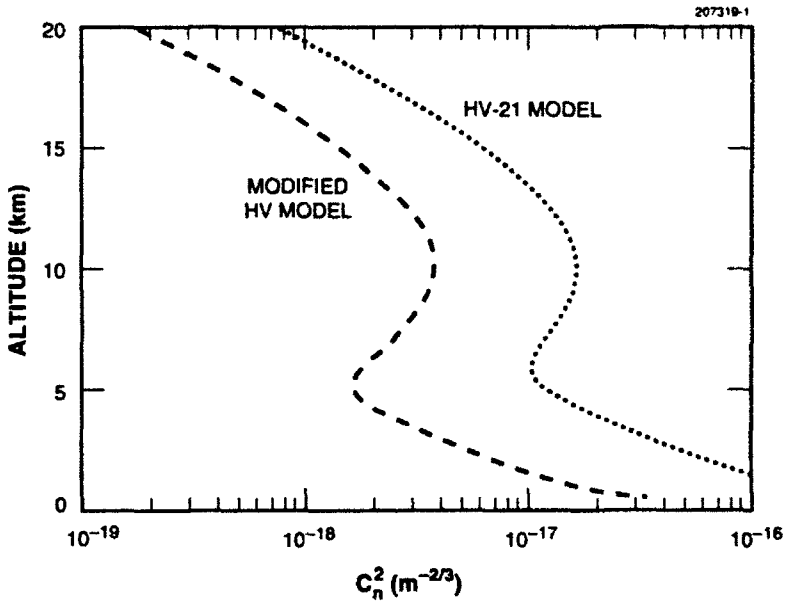

Figure 1. Comparison of the HV-21 model typically used for calculations of daytime turbulence and the modified HV model developed by the authors to represent nighttime turbulence conditions at good seeing locations.

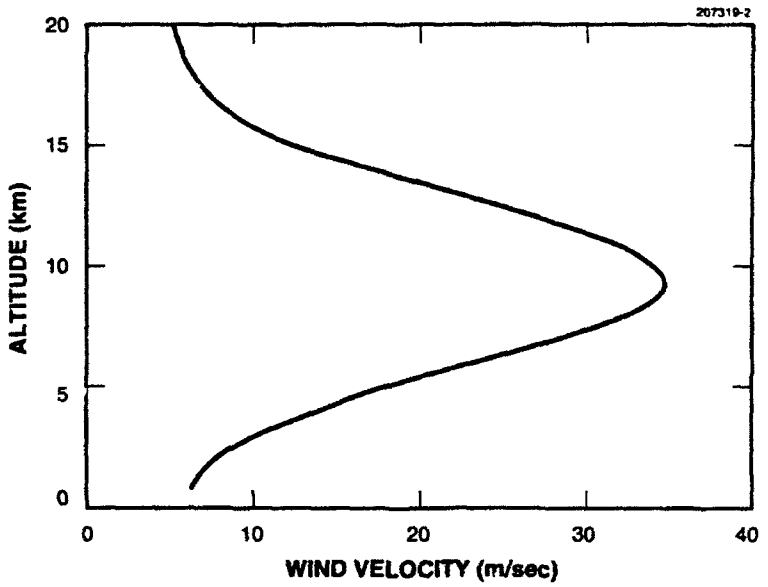

Figure 2. The Bufton wind-velocity profile.

TABLE 1

Summary of Turbulence Parameters for Imaging Systems Operating at 0.55 μm

		r_0 (cm)	θ_{seeing} (arc-sec)	θ_0 (mrad)	τ_0 (msec)
SLC-Day Model	0° Zenith	5.7	2.4	13.8	2.7
	45° Zenith	4.6	3.0	8.0	2.2
HV-21 Model	0° Zenith	5.6	2.5	7.8	2.1
	45° Zenith	4.5	3.1	4.5	1.7
Modified HV Model	0° Zenith	20.0	0.69	20.0	6.3
	45° Zenith	16.2	0.85	11.5	5.1

2.3 PERFORMANCE MODELS FOR CONVENTIONAL ADAPTIVE-OPTICS SYSTEMS

An adaptive-optics system for real-time phase conjugation can be characterized as a highly-parallel servo device capable of sensing and correcting the incoming wavefront at the pupil plane of an imaging sensor. Performance close to the diffraction limit of the input aperture can be achieved in the limit that the angular separation between the turbulence probe and the target object is small ($<\theta_0$), the spacing between control elements on the active optical element is well matched to the turbulence coherence length ($<r_0$), and a sufficiently high update rate is maintained ($>1/\tau_0$). In most practical implementations of this concept, however, performance compromises are necessary to reduce component costs and maximize the sensitivity of the wavefront sensor. At this point, a brief description of the architecture of an adaptive-optics system is appropriate. A more detailed discussion of the basic components and an interesting overview of the early history of this field can be found in John Hardy's classic paper on this subject [11].

The four essential elements of a conventional adaptive-optics system are shown in Figure 3. Light originating from an exoatmospheric source is corrupted in both amplitude and phase as a result of random fluctuations in the refractive index of the intervening air. The quality of the image formed at the focus

of a ground-based telescope is largely driven by phase distortions, which can be corrected through the insertion of an optical surface having the conjugate optical path difference (OPD). Most compensation systems apply this conjugate phase with a pair of active elements consisting of a high-speed tilt mirror and a deformable mirror that removes the figure (tilt-removed) component of the distortion. Error signals are generated by the phase sensor, which actually measures the first derivative of the phase of the incoming wavefront. A phase-computation device, referred to as a reconstructor, transforms the output of the wavefront sensor into a set of drive signals that control the active optical elements.

Each of these components has a unique set of error mechanisms that together establish the overall effectiveness of the adaptive-optics system. In the following sections, the first-order effects of these errors are quantified; the most important effects are then combined in a servo-loop model that provides a concise description of the dynamic performance characteristics.

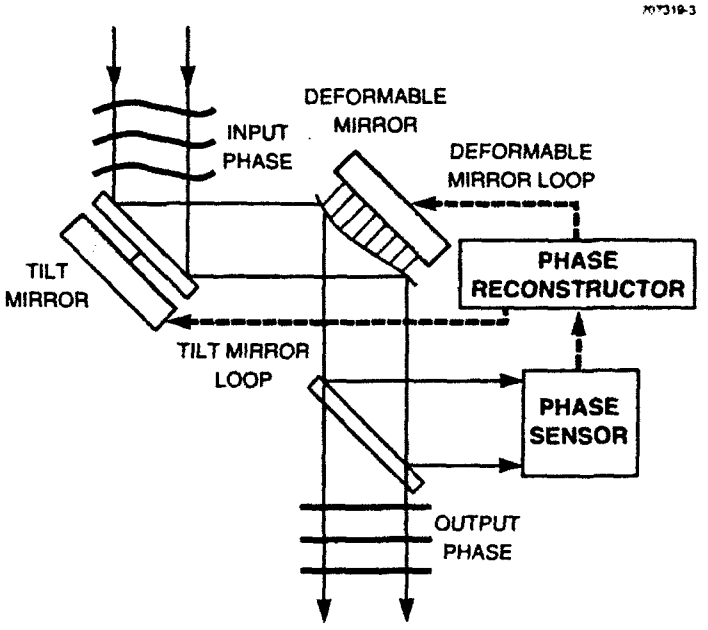

Figure 3. Essential components of an adaptive-optics phase-compensation system. Error signals developed from the phase difference between the incoming wavefront and the deformable mirror are measured by the phase sensor and subsequently applied to the two active optical elements.

2.3.1 The Wavefront Sensor

Essentially all wavefront-sensing instruments in current use measure local changes in the pupil-plane phase function; a direct determination of phase is difficult because a coherent full-aperture reference

would be required. At least three sensing techniques have been successfully demonstrated: Hartmann sensors, in which the input pupil is segmented by a set of lenslets that form separate images of the source in the Fourier plane [11]; shearing sensors that convert phase gradients into intensity variations [11]; and sensors that measure local wavefront curvature [12]. The noise characteristics of the Hartmann and shearing sensors are similar and reasonably well understood, although the former is more easily described. For this reason, the Hartmann design will be used as the prototype in this analysis.

The sensor model used in this study is based on the realization illustrated in Figure 4. A lenslet array placed at an image of the pupil plane is used to generate a set of independent far-field images; the positions of these images are linearly related to the wavefront tilt over the lenslets' diameter. An array of sensors is then employed to measure the centroid position of each of the focused spots.

Although the first detector arrays were composed of discrete photomultiplier tubes, these were later replaced by image intensifiers mated to solid-state cameras and, more recently, by high-quantum-efficiency CCDs [13]. Because the noise level of a CCD camera is proportional to the square root of the readout bandwidth, it is often advantageous to use separate imagers to perform the x- and y-gradient measurements. This configuration allows on-chip data summation to be performed in the direction perpendicular to the gradient measurement and reduces the number of data points from n^2 to $2n$ per subaperture. Under these conditions, a one-dimensional sensor model incorporating a linear subarray of n pixels is sufficient to describe all relevant effects. The size of the subarray will depend on the required dynamic range, although a pair of elements per subaperture per camera should be adequate for continuous wave (CW) operation under benign turbulence conditions.

To simplify this discussion of phase-sensor performance, it will be assumed that the lenslets divide the pupil plane into an array of subapertures of dimension d_s. (The physical components are generally much smaller than the collection aperture and would be placed in a collimated region of the optical path at the output of the telescope.) For a phase change of one wave across the subaperture, the Hartmann spot will experience a linear translation of $\lambda f/d_s$, where f is the lenslet focal length and λ is the wavelength of the turbulence probe. Near the null position of a two-element centroid detector, an appropriate linear algorithm for determining the local gradient would be

$$g = 2\pi\left(\frac{d_s}{2\lambda f \Gamma(0)}\right)\frac{-\Gamma_L + \Gamma_R}{\Gamma_L + \Gamma_R} \quad \text{(rad / subaperture)} \ , \tag{2-13}$$

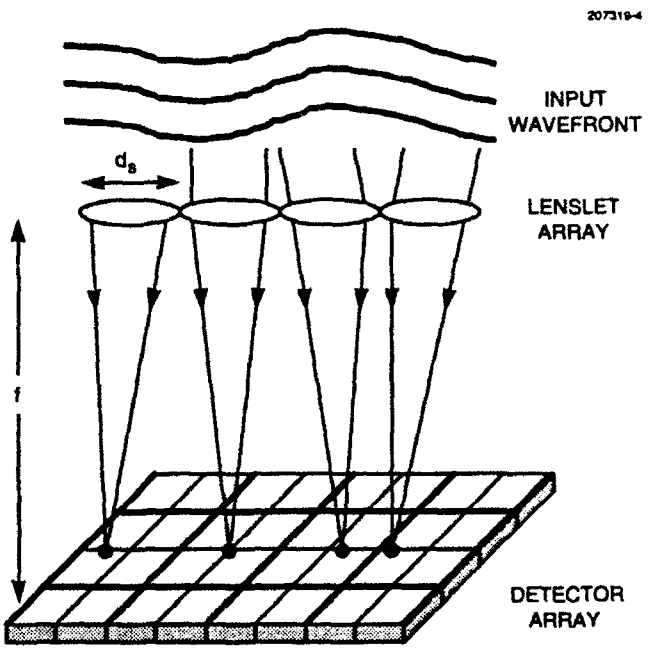

Figure 4. Schematic description of a Hartmann wavefront sensor. The incoming wavefront is divided into a matrix of subapertures by a lenslet array, which produces a set of focused spots onto a detector array. The displacement of the spots from their local null position provides a measure of the local phase gradient.

where $\Gamma(x)$ is the normalized intensity distribution of the Hartmann spot and the symbols Γ_L and Γ_R represent the number of photoelectrons collected by the left and right detector elements, respectively. If the spot is diffraction-limited,

$$\Gamma(x) = \left(\frac{d_s}{\lambda f}\right)\left\{\frac{\sin(\pi d_s x/\lambda f)}{\pi d_s x/\lambda f}\right\}^2 \tag{2-14}$$

for a square lenslet, where $\Gamma(0)$ is simply the inverse of the spot diameter, d_{spot}. When the subaperture becomes much larger than r_0, the spot diameter will be roughly proportional to $\lambda f/r_0$. Yura [14] suggests the following profile for the general case:

$$d_{spot} \approx \frac{f\lambda}{d_s}\sqrt{1+\left(\frac{d_s}{r_0}\right)^2\left[1-0.37\left(\frac{r_0}{d_s}\right)^{1/3}\right]} \approx \frac{f\lambda}{d_s}\sqrt{1+\left(\frac{d_s}{r_0}\right)^2} \quad . \tag{2-15}$$

Combining Equations (2-13) and (2-15) yields the following result:

$$g = \pi \sqrt{1 + \left(\frac{d_s}{r_0}\right)^2} \, \frac{-\Gamma_L + \Gamma_R}{\Gamma_L + \Gamma_R} \quad . \tag{2-16}$$

The photon noise associated with the centroid detector characterized by Equation (2-16) is readily developed by applying Poisson statistics to the detector outputs, so that the count variance in each pixel is equal to the absolute number of photoelectrons. Using $N_{pe} = 2(\Gamma_L + \Gamma_R)$ to represent the total number of photoelectrons collected by the x and y sensors within a single subaperture, an expression for the gradient variance for a beam near the null position is derived:

$$\sigma_g^2 \approx \frac{2\pi^2 \left[1 + \left(d_s/r_0\right)^2\right]}{N_{pe}} \quad . \tag{2-17}$$

The second major error is a result of random signal fluctuations generated by the transfer of photoelectrons through the detector array, off-chip preamplifiers, and digitizers. This uncorrelated noise variance, represented by N_{rms}^2, can be reduced relative to the photon-noise contribution if an optical intensifier having a net photoelectron gain of G_e is placed at the entrance aperture of the wavefront sensor. Assuming that each pixel has an identical noise contribution, the following expression is obtained from Equation (2-16):

$$\sigma_g^2 \approx 2\left(\frac{2\pi}{G_e N_{pe}} \sqrt{1 + \left(\frac{d_s}{r_0}\right)^2}\right)^2 N_{rms}^2 = \frac{8\pi^2 \left[1 + \left(d_s/r_0\right)^2\right] N_{rms}^2}{\left(G_e N_{pe}\right)^2} \quad . \tag{2-18}$$

A more general expression for subapertures that incorporate more than two elements is derived in Section C.2 of Appendix C.

Equations (2-17) and (2-18) provide an accurate description of the performance of a Hartmann sensor; to maintain generality, however, a few additional concepts will be introduced at this time. To allow for the possibility that the compensation wavelength, λ_c, differs substantially from the phase sensor wavelength, λ_p, the multiplicative factor $\left(k_c/k_p\right)^2$ must be inserted to convert the error expression to rad^2 of phase error at λ_c. Furthermore, because it is convenient to define the fundamental turbulence parameters (r_0, θ_0, and τ_0) at the compensation wavelength, it can be seen from Equation (2-5) that the turbulence coherence length at λ_p is properly given by $(k_p/k_c)^{6/5} r_0$. Finally, the following representation will be applied for the number of collected photoelectrons:

$$N_{pe} = \left(\frac{2\pi}{hc\,k_p}\right) \eta \, \tau_d \, d_s^2 \, I_p \quad , \tag{2-19}$$

where I_p (W/m^2) is the irradiance at the entrance of the wavefront sensor, η is the sensor quantum efficiency, τ_d is the sensor dwell time, and d_s^2 is the subaperture collection area. The final result is

$$\left(\sigma^2_{\text{figure}}\right)_{\text{noise}} \approx \underbrace{\frac{\pi hc\left(\frac{k_c^2}{k_p}\right)\left[1+\left(\frac{k_p}{k_c}\right)^{12/5}\left(\frac{d_s}{r_0}\right)^2\right]}{\eta\,\tau_d\,d_s^2\,I_p}}_{\text{photon noise}} + \underbrace{\frac{2\left(hck_c\right)^2\left[1+\left(\frac{k_p}{k_c}\right)^{12/5}\left(\frac{d_s}{r_0}\right)^2\right]N_{\text{rms}}^2}{\left(G_e\,\eta\,\tau_d\,d_s^2\,I_p\right)^2}}_{\text{sensor noise}} . \tag{2-20}$$

Notice that the photon-noise term is independent of the subaperture size when d_s is much larger than the coherence length for λ_p. In this regime, the noise reduction expected with an increased subaperture diameter (due to the larger number of detected photons) is directly offset by a reduction in sensitivity to wavefront gradients.

The motivation for using low-noise CCD arrays as opposed to intensified cameras for wavefront sensing is addressed in Figure 5. Although the gain of an intensifier can always be made high enough to obtain photon-noise-limited operation, the quantum efficiency of these devices seldom exceeds 10 percent. In contrast, backside-illuminated CCD cameras are now available that are better than 80 percent efficient in the visible and can operate at high frame rates with transfer noise levels in the 20–40-electron range. Within the normal range of operation for high-quality turbulence compensation (where the average gradient error would be lower than $\lambda/10$), the performance of a well-designed CCD system is expected to surpass that of the intensified camera. For this reason, the wavefront sensor in current use at Lincoln Laboratory incorporates a pair of custom-built 64 × 64-CCD focal planes.

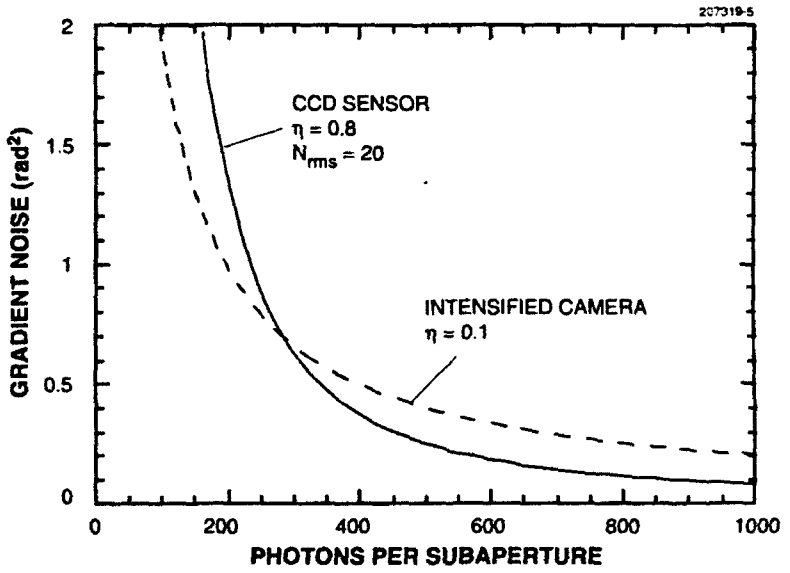

Figure 5. Performance comparison of the two major types of Hartmann-sensor cameras. This calculation was performed for a phase sensor having two pixels per subaperture subarray and a subaperture dimension smaller than r_o.

2.3.2 The Phase Reconstructor

In the limit of infinite measurement resolution, the relationship between the phase, ϕ, and the phase gradient, g, is given by the Poisson equation, with Neumann boundary conditions,

$$\nabla^2 \phi = \text{div}\, g \quad . \tag{2-21}$$

For a discrete-measurement system, this relationship can be represented by a linear process

$$\vec{g} = A\vec{\phi} \quad , \tag{2-22}$$

in which $\vec{g}$ and $\vec{\phi}$ are vectors and A is a two-dimensional matrix. The least-square solution to this equation can be recovered from the generalized inversion of the A matrix

$$\vec{\phi} = \left\{\left(A^t A\right)^{-1} A\right\}\vec{g} = B\vec{g} \quad . \tag{2-23}$$

Because B is invariant for a given sensor configuration, the matrix inversion only needs to be performed once and can be preprogrammed into the computational device.

Modern reconstructors employ digital processors that can perform the matrix operation indicated in Equation (2-23) within a time period much smaller than the turbulence time constant. For example, the reconstructor built by Lincoln Laboratory for a set of recent field experiments performs a 241 × 436 matrix calculation with 8-bit precision in less than 50 μsec; this corresponds to an average computational rate of the order of 10^9 operations per second [15]. Mathematical techniques are currently under development that would permit much larger arrays to be processed even more efficiently.

The noise characteristics of a reconstructor are defined by its error propagator, which is a multiplicative constant that relates the variance of the input gradient measurements to the variance of the output phase estimates. Herrmann [16] has shown that the error propagator for a compensation system that has a few hundred actuators is approximately unity.

In summary, a well-designed reconstruction system will introduce no significant temporal delay or excess noise into the phase-compensation process.

2.3.3 The Deformable Mirror

Several innovative mirror designs have been developed in the last ten years that incorporate either modal (Zernike deconvolution) [12] or zonal control of the mirror surface [17,18]; both continuous-surface and segmented-mirror designs have been successfully demonstrated. The 14-cm deformable mirror in current use at Lincoln Laboratory is an Itek design that incorporates a set of 241 discrete actuators mated to a thin glass facesheet, as illustrated in Figure 6. The characteristics of the facesheet have been chosen to provide a smooth transition between actuator drive points under normal turbulence conditions and to yield a fitting error of better than 1/20 wave rms over a 60-cm telescope aperture. The actuators are made by stacking thin sections of lead magnesium niobate (PMN), which is a low-voltage electrostrictive material. A deflection of ±1.5 μm has been measured with a drive voltage of ±150 volts; the average full-stroke settling time is on the order of 200 μsec. At this speed, the temporal characteristics of the mirror have a negligible effect on the overall system performance.

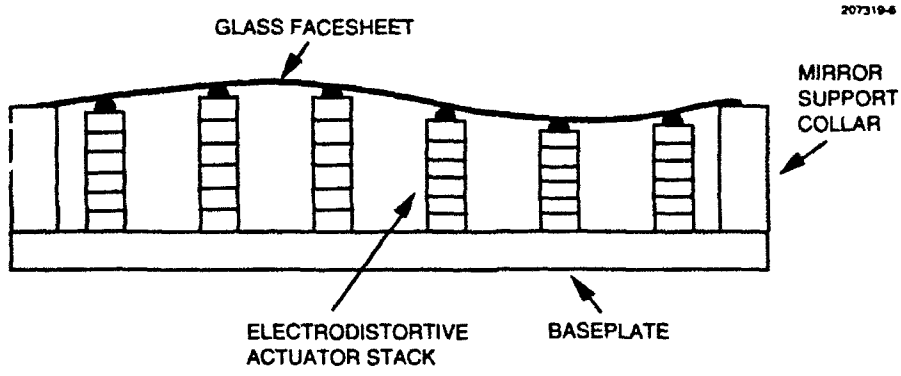

Figure 6. Cross-section of a typical deformable mirror employing a flexible facesheet and a two-dimensional array of actuator stacks. The actuators are cemented to the facesheet so that the surface can be deformed by either extending or contracting the actuator dimension.

The major degrading effect associated with a deformable mirror is fitting error, which occurs whenever the actuator spacing in the pupil plane exceeds the turbulence coherence length. Greenwood [19] has derived a relationship between the error variance and the number of actuators, N_a ;

$$\left(\sigma^2_{\text{figure}}\right)_{\text{fitting}} \approx 0.274\left(D/r_0\right)^{5/3} N_a^{-5/6} \quad , \tag{2-24}$$

which can be rewritten to reflect the error associated with a subaperture spacing of d_s :

$$\left(\sigma^2_{\text{figure}}\right)_{\text{fitting}} \approx 0.34\left(d_s/r_0\right)^{5/3} \quad . \tag{2-24'}$$

The general form of this equation has been verified in simulation studies using the measured parameters of Lincoln's deformable mirror, although the leading constant has been found to vary between 0.4 and 0.8, depending on how the outer edge of the flexible mirror surface is constrained. These effects can be minimized by employing at least one ring of active actuators outside the illuminated region of the aperture to provide a smooth transition between the mirror interior and the support collar. For the purpose of this study, the following, somewhat more conservative, estimate will be adopted:

$$\left(\sigma^2_{\text{figure}}\right)_{\text{fitting}} \approx 0.5\left(d_s/r_0\right)^{5/3} \quad . \tag{2-25}$$

2.3.4 A Time-Dependent Model of the Phase-Compensation Process

The individual characterizations of component performance provide no information about the dynamic effects that drive the update rate of an adaptive-optics system. This issue is perhaps best addressed

by constructing a servo-loop model for each of the active control elements. Thus, two classes of models will be required—one to describe the movement of the actuators on the deformable mirror and one for the control of the tilt mirror. The final result will be a set of error expressions, the first of which describes the total figure distortion:

$$\left(\sigma^2_{\text{figure}}\right)_{\text{servo}} = \underbrace{\int_0^\infty T_f(f)F_f(f)df}_{\text{turbulence-induced figure error}} + \underbrace{\int_0^\infty T_{fn}(f)F_{fn}(f)df}_{\text{figure noise}} \quad (\text{rad}^2 \text{ of phase}), \quad (2\text{-}26)$$

and similarly for the overall tilt error,

$$\left(\sigma^2_{\text{tilt}}\right)_{\text{servo}} = \underbrace{\int_0^\infty T_t(f)F_t(f)df}_{\text{turbulence-induced tilt error}} + \underbrace{\int_0^\infty T_{tn}(f)F_{tn}(f)df}_{\text{tilt noise}} \quad (\text{rad}^2 \text{ of tilt}). \quad (2\text{-}27)$$

The first term in each of these equations is the residual error due to uncompensated turbulence, whereas the second term is the noise associated with a finite signal into the sensor. The parameters $T(f)$ and $F(f)$ represent servo transmission functions and signal power spectra, respectively. Because the power spectra for figure and tilt are quite different, the bandwidth requirements for each must be developed separately.

A schematic diagram of the servo system is provided in Figure 7. The wavefront sensor measures the difference between the optical phase of the incoming wavefront and the phase applied to the deformable mirror. This error signal is averaged over a dwell time, τ_d, and subsequently passed to an accumulator that adds the measured error to the previous mirror-drive position. For simplicity, the mirror update is assumed to occur as a step input at the end of each integration cycle, and each mirror correction is held until the next update. This quasi-CW representation accurately describes the operation of modern digital-control architectures.

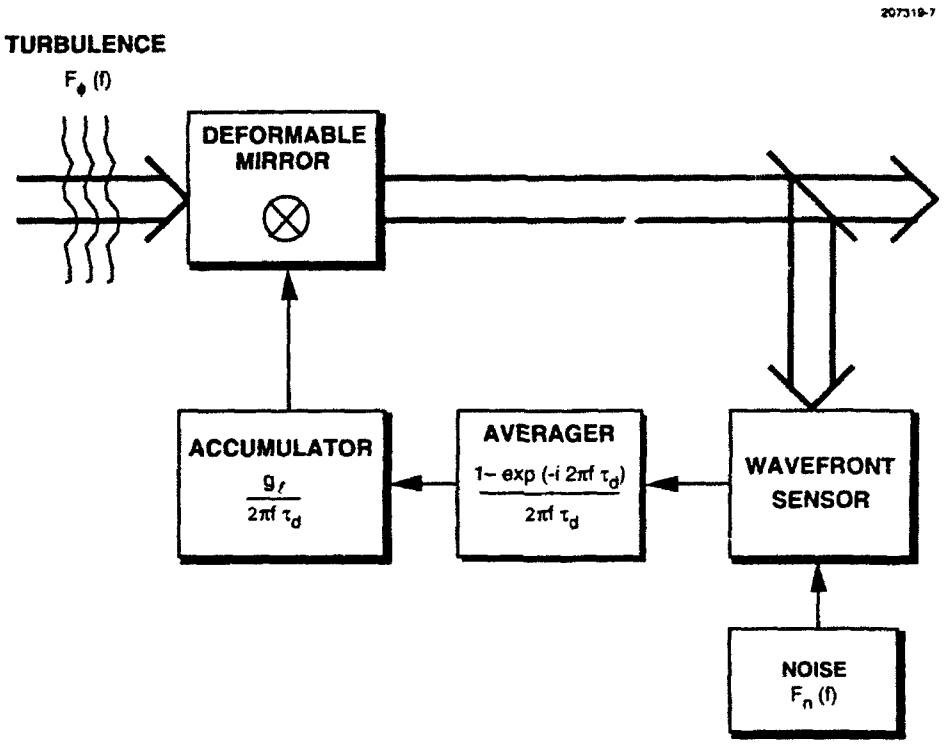

Figure 7. Servo-loop diagram for a digital control system employing a boxcar averaging device and a digital accumulator. The error signal at the wavefront sensor is averaged for a period of τ_d. The accumulator provides the deformable mirror with an impulse drive signal at the end of each integration interval; this signal is subsequently held until the next drive signal.

Frequency-domain models for each of the components shown in Figure 7 can be found in a number of standard texts [20]. The phase error sampling system is described by the function

$$H_s(f) = \frac{\sin(\pi f \tau_d)}{\pi f \tau_d} \times \exp(-i\pi f \tau_d) = \frac{1-\exp(-i2\pi f \tau_d)}{2\pi f \tau_d}, \tag{2-28}$$

which includes an integration period of τ_d and an average delay time of $\tau_d/2$ between the input and output signals. The digital accumulator, which adds the incremental error signal to the current mirror position, is represented by

$$H_a(f) = \frac{g_\ell}{2\pi f \tau_d}, \tag{2-29}$$

where g_ℓ is a normalized loop-gain constant. Finally, the drive response for a mirror time constant, τ_m, would be

$$H_m(f) = \frac{1}{i2\pi f\,\tau_m + 1}\,. \tag{2-30}$$

Generally, $\tau_m \ll \tau_d$ for state-of-the-art hardware, so this term can be safely ignored.

From the component transfer functions given above, an equivalent control-circuit description can be developed for the propagation of optical turbulence and electrical noise through the system. The net loop response to atmospheric turbulence is found to be

$$T_\phi(f) = \left|\frac{1}{1 + H_s(f)\,H_a(f)}\right|^2 = \frac{(2\pi f\,\tau_d)^2}{4\sin^2(\pi f\,\tau_d)\left[\dfrac{g_\ell^2}{(2\pi f\,\tau_d)^2} - g_\ell\right] + (2\pi f\,\tau_d)^2}\,. \tag{2-31}$$

The noise transfer function obtains from the assumption that electrical noise originates in the sensing device and is transferred to the control elements through the signal averager and accumulator. Therefore,

$$T_n(f) = \left|\frac{H_s(f)\,H_a(f)}{1 + H_s(f)\,H_a(f)}\right|^2 = \frac{1}{1 - \dfrac{(2\pi f\,\tau_d)^2}{g_\ell} + \dfrac{(2\pi f\,\tau_d)^4}{4g_\ell^2\sin^2(\pi f\,\tau_d)}}\,. \tag{2-32}$$

These two equations are plotted as a function of normalized frequency and gain in Figures 8 and 9. The transfer curve for turbulence has the characteristics of a high-pass filter, whose shape most closely matches an ideal step function when the gain is approximately equal to one. By contrast, the noise transfer curve for this system is a low-pass filter, which is also optimized when $g_\ell \approx 1$. Both of these expressions are greatly simplified for gain of unity, resulting in the approximations

$$T_\phi(f) \approx \frac{(2\pi f\,\tau_d)^2 + (2\pi f\,\tau_d)^4/12}{1 + (2\pi f\,\tau_d)^4/12}\,, \tag{2-33}$$

and

$$T_n(f) \approx \frac{1}{1 + (2\pi f\,\tau_d)^4/12}\,. \tag{2-34}$$

The turbulence-rejection bandwidth of the first of these functions is approximately $1/10\tau_d$, whereas the integral of the noise transfer function is about $1/3\tau_d$.

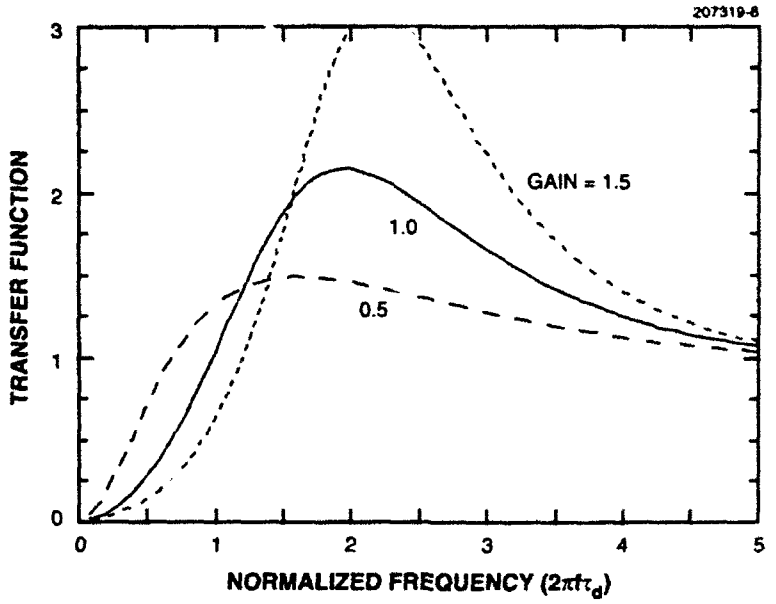

Figure 8. Turbulence transfer function for a quasi-CW closed-loop compensation system as a function of loop gain.

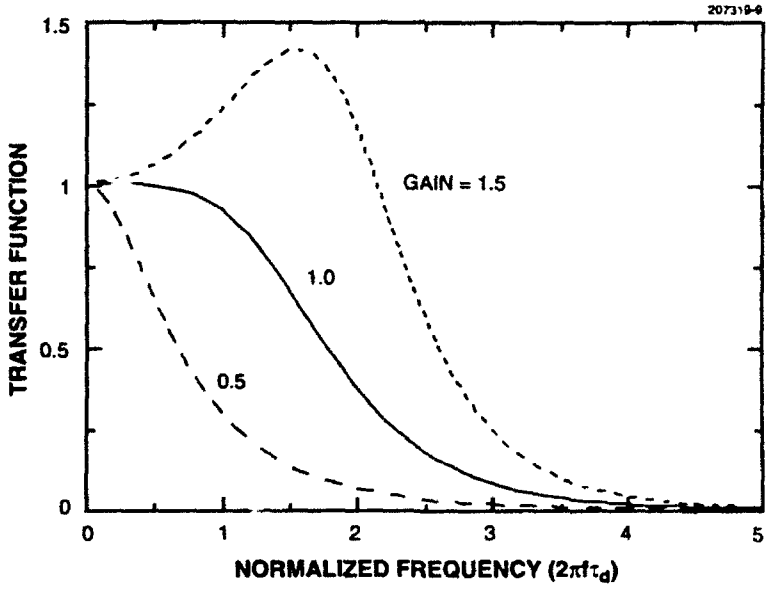

Figure 9. Noise transfer function for a quasi-CW closed-loop compensation system as a function of loop gain.

To complete this analysis, four sets of signal spectra are required to describe the effects of turbulence and noise on both the figure- and tilt-compensation systems. The figure component of turbulence is developed from a paper by Greenwood and Fried [21], which is discussed in more detail in Section C.3 of Appendix C. This spectrum, which is plotted in Figure 10, can be approximated by a function having two segments

$$F_f(f) = \begin{cases} 0.132\sec(\zeta) k_c^2 D^4 \mu_0^{12/5} v_{5/3}^{-7/5} f^{4/3} & : f \le 0.705 D^{-1} \mu_0^{-3/5} v_{5/3}^{3/5} \\ 0.0326\sec(\zeta) k_c^2 v_{5/3} f^{-8/3} & : f \ge 0.705 D^{-1} \mu_0^{-3/5} v_{5/3}^{3/5} \end{cases} \quad (2\text{-}35)$$

The units are rad^2 of phase error per Hz. A concise treatment of full-aperture tilt was recently published by Tyler [22]. This spectrum also has a simple form in its low- and high-frequency limits that can be joined at their intersection to give

$$F_t(f) = \begin{cases} 1.60\sec(\zeta) v_{-1/3} f^{-2/3} & : f \le 0.445 D^{-1} v_{-1/3}^{-1/5} v_{14/3}^{1/5} \\ 0.028\sec(\zeta) D^{-5} v_{14/3} f^{-17/3} & : f \ge 0.445 D^{-1} v_{-1/3}^{-1/5} v_{14/3}^{1/5} \end{cases} \quad (2\text{-}36)$$

where the units here are rad^2 of single-axis tilt per Hz and normalized for integration over positive values of f. A plot of this function for a 4-m aperture is given in Figure 11.

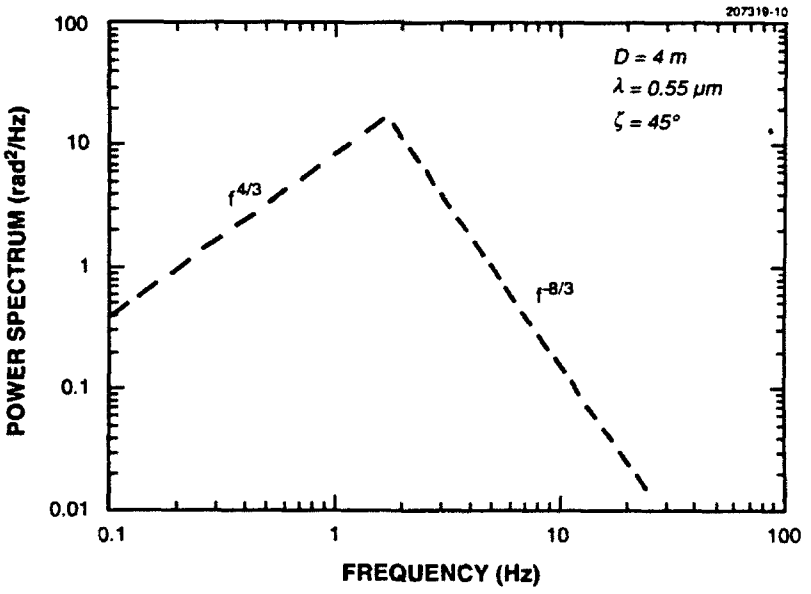

Figure 10. Power spectrum for turbulence-induced figure error. This model incorporates atmospheric moments developed from the modified Hufnagel-Valley turbulence profile and the Bufton wind profile.

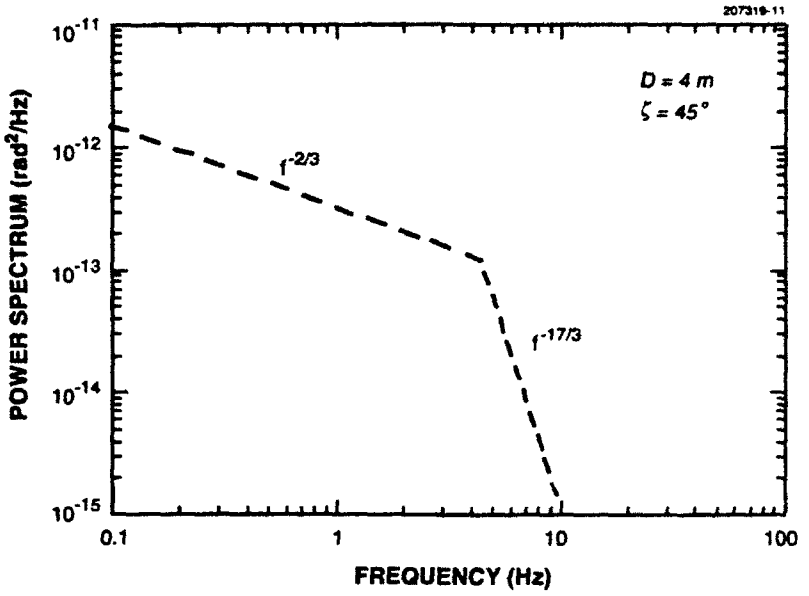

Figure 11. Power spectrum for turbulence-induced tilt error, given in units of rad² of single-axis tilt per Hz. This model incorporates atmospheric moments developed from the modified Hufnagel-Valley turbulence profile and the Bufton wind profile.

The figure component of the noise power spectrum can be obtained from Equation (2-20) by assuming that the noise is white and passes through a filter having the form

$$H_{\text{avg}}(f) = \left[\frac{\sin(\pi f \tau_d)}{\pi f \tau_d}\right]^2 , \tag{2-37}$$

which is the transfer function for a boxcar averager with a time constant, τ_d. The integral of this transfer function introduces a normalization factor of $2\tau_d$, so that

$$F_{fn}(f) = 2\tau_d \left(\sigma^2_{\text{figure}}\right)_{\text{noise}}$$

$$= \frac{2\pi hc\left(\frac{k_c^2}{k_p}\right)\left[1+\left(\frac{k_p}{k_c}\right)^{12/5}\left(\frac{d_s}{r_0}\right)^2\right]}{\eta\, d_s^2\, I_p} + \frac{2\left(hck_c\right)^2\left[1+\left(\frac{k_p}{k_c}\right)^{12/5}\left(\frac{d_s}{r_0}\right)^2\right]N^2_{\text{rms}}}{\left(G_e\,\eta\, d_s^2\, I_p\right)^2 \tau_d}$$

$$(\text{rad}^2 \text{ of phase / Hz}) \ . \tag{2-38}$$

A Hartmann sensor can also be viewed as a tracking device in which a phase shift of 1 rad over a receiver diameter D corresponds to a $1/kD$ angular displacement of the focal spot. Thus the noise spectrum for tracking can be obtained from Equation (2-38) by converting the collection area to $\frac{\pi}{4}D^2$, the wavenumber to k_t, the dwell time to τ_{dt}, the irradiance to I_t, and multiplying by $(1/k_cD)^2$;

$$F_{tn}(f) = \frac{8hc\left[1+\left(\frac{k_t}{k_c}\right)^{12/5}\left(\frac{D}{r_0}\right)^2\right]}{k_t\,\eta\,D^4\,I_t} + \frac{32\,(hc)^2\left[1+\left(\frac{k_t}{k_c}\right)^{12/5}\left(\frac{D}{r_0}\right)^2\right]N_{\text{rms}}^2}{\pi^2\,D^6\left(G_e\,\eta\,I_t\right)^2\,\tau_{dt}}$$

$$(\text{rad}^2 \text{ of tilt / Hz}) \ . \qquad (2\text{-}39)$$

An evaluation of all the individual error sources is now possible by combining the last six equations and performing the integrations indicated in Equations (2-26) and (2-27). The noise terms are straightforward, because the integrals of the figure and tilt transfer functions are $1/3\tau_d$ and $1/3\tau_{dt}$, respectively. The turbulence integrals are somewhat more complicated, but are amenable to a few simplifying assumptions. For high-bandwidth figure compensation, accurate results are obtained by using the high-frequency form of the figure spectrum over the entire frequency range, so that

$$\int_0^\infty T_f(f)F_f(f)\,df \approx 0.0326\sec(\zeta)k_c^2\,v_{5/3}\int_0^\infty \frac{(2\pi f\,\tau_d)^2+(2\pi f\,\tau_d)^4/12}{1+(2\pi f\,\tau_d)^4/12}\,f^{-8/3}\,df$$

$$\approx 2.80\sec(\zeta)k_c^2\,v_{5/3}\,\tau_d^{5/3} \qquad (\text{rad}^2 \text{ of phase}) \ . \qquad (2\text{-}40)$$

Therefore, the figure error associated with the operation of the servo system is found to be

$$\left(\sigma^2_{\text{figure}}\right)_{\text{servo}} = 0.962\left(\tau_d/\tau_0\right)^{5/3}$$

$$+\frac{2\pi\,hc\left(\frac{k_c^2}{k_p}\right)\left[1+\left(\frac{k_p}{k_c}\right)^{12/5}\left(\frac{d_s}{r_0}\right)^2\right]}{3\,\eta\,\tau_d\,d_s^2\,I_p} + \frac{2\left(hck_c\right)^2\left[1+\left(\frac{k_p}{k_c}\right)^{12/5}\left(\frac{d_s}{r_0}\right)^2\right]N_{\text{rms}}^2}{3\left(G_e\,\eta\,\tau_d\,d_s^2\,I_p\right)^2}$$

$$(\text{rad}^2 \text{ of phase}) \ . \qquad (2\text{-}41)$$

The total figure error is obtained by adding the deformable mirror fitting error [specified in Equation (2-25)] to this result.

The computation of the turbulence-induced tilt error is performed by first recognizing that the high-frequency roll-off in the tilt spectrum is sufficiently rapid to allow contributions beyond the low-frequency cut-off to be ignored. In this range, the transfer function is proportional to the square of the frequency. From Equations (2-33) and (2-36),

$$\int_0^\infty T_t(f)\,F_t(f)\,df \approx 1.60\sec(\zeta)\,v_{-1/3}^{0.445\,D^{-1}\,v_{-1/3}^{-1/5}\,v_{14/3}^{1/5}} \int_0^{} (2\pi f\,\tau_{dt})^2\,f^{-2/3}\,df$$

$$\approx 4.09\sec(\zeta)\,D^{-7/3}\,v_{-1/3}^{8/15}\,v_{14/3}^{7/15}\,\tau_{dt}^2 \qquad (\text{rad}^2 \text{ of tilt}), \tag{2-42}$$

which leads to the following expression for the total single-axis tilt jitter:

$$\left(\sigma_{\text{tilt}}^2\right)_{\text{servo}} \approx 4.09\sec(\zeta)\,D^{-7/3}\,v_{-1/3}^{8/15}\,v_{14/3}^{7/15}\,\tau_{dt}^2$$

$$+\frac{8\,hc\left[1+\left(\frac{k_t}{k_c}\right)^{12/5}\left(\frac{D}{r_0}\right)^2\right]}{3\,k_t\,\eta\,\tau_{dt}\,D^4\,I_t}+\frac{32\,(hc)^2\left[1+\left(\frac{k_t}{k_c}\right)^{12/5}\left(\frac{D}{r_0}\right)^2\right]N_{\text{rms}}^2}{3\pi^2\,D^6\left(G_e\,\eta\,\tau_{dt}\,I_t\right)^2}$$

$$(\text{rad}^2 \text{ of tilt}). \tag{2-43}$$

Equations (2-41) and (2-43) provide a reasonably complete and accurate description of the dynamic characteristics of an adaptive-optics servo system.

2.4 WORKING DEFINITIONS OF ERROR VARIANCE, STREHL, AND IMAGING RESOLUTION

Quantitative estimates of overall system performance are notoriously difficult to achieve, particularly when the cumulative errors are large. The usual approach is to compute the phase error in the pupil plane due to each source, then develop a total error by adding the variances

$$\sigma_{\text{total}}^2 = \sum_i \sigma_i^2 \quad . \tag{2-44}$$

This will result in an over-estimate of the error unless the individual effects are statistically independent.

For laser-beam propagation, the quantity of interest is the Strehl ratio, which is defined as the relationship between the measured on-axis intensity and the peak intensity of a diffraction-limited beam. It is observed that when the rms pupil-plane phase distortion is much smaller than one wave, the width

of the short-exposure beam will remain essentially unchanged but the peak energy will degrade exponentially according to the expression

$$\text{Strehl} \approx \exp\left(-\sigma^2\right) , \tag{2-45}$$

which is known as the extended Maréchal approximation. The energy lost from the main beam will appear as a set of diffraction-limited "speckles" that are randomly distributed over a region that is inversely proportional to the turbulence coherence diameter. As the distortion level is increased, the main beam will eventually become so depleted that it becomes indistinguishable from the rest of the speckle field. In this regime it is more difficult to establish an unambiguous definition of Strehl, but the form suggested by Yura [14] is probably appropriate;

$$\text{Strehl} \approx \frac{1}{1+\left[D/\rho_0\right]^2} . \tag{2-46}$$

ρ_0 is a characteristic coherence length that can be computed for either short or long exposures; for uncorrected turbulence both of these quantities are approximately equal to r_0.

No single strategy for specifying Strehl or sensor resolution is suitable for all situations. In many cases, however, a reasonably accurate estimate of these quantities can be obtained by combining the Strehl expressions given by Maréchal and Yura, under the assumption that the energy lost from the main peak is distributed over a beam profile characterized by λ_c/ρ_0. The resulting beam profile for short exposure would be

$$[\text{Strehl}]_{\text{SE}} \approx \exp\left(-\sigma^2_{\text{figure}}\right) + \frac{1-\exp\left(-\sigma^2_{\text{figure}}\right)}{1+\left[D/\rho_0^{\text{SE}}\right]^2} , \tag{2-47}$$

where the short-exposure coherence length, ρ_0^{SE}, may also depend on σ^2_{figure}. From this description of the Strehl, a form for the composite system resolution is evolved that incorporates a weighted average of the diffraction-limited resolution, $1.22\lambda_c/D$, and the resolution in the limit of large phase error, $\left(1.22\lambda_c/D\right)\sqrt{1+\left[D/\rho_0^{\text{SE}}\right]^2}$. The following expression is the rms of the product of the Strehl and the resolution for the two limiting cases:

$$[\text{Resolution}]_{\text{SE}} \approx 1.22\left(\frac{\lambda_c}{D}\right) \frac{\sqrt{\exp\left(-2\sigma^2_{\text{figure}}\right) + \dfrac{\left[1-\exp\left(-\sigma^2_{\text{figure}}\right)\right]^2}{1+\left[D/\rho_0^{\text{SE}}\right]^2}}}{[\text{Strehl}]_{\text{SE}}} . \tag{2-48}$$

An equivalent equation for the long-exposure Strehl can be developed by increasing the short-exposure beam profile to reflect the addition of a single-axis tilt jitter (rads of angle) of σ^2_{tilt}. Recognizing

that a Gaussian beam characterized by a standard deviation of $0.45\lambda_c/D$ accurately reproduces the core of the Airy function, it can be seen that

$$[\text{Strehl}]_{\text{LE}} \approx \frac{\exp\left(-\sigma^2_{\text{figure}}\right)}{1+4.94\left(\frac{D}{\lambda_c}\right)^2\sigma^2_{\text{tilt}}} + \frac{1-\exp\left(-\sigma^2_{\text{figure}}\right)}{1+\left[D/\rho_0^{\text{LE}}\right]^2} \tag{2-49}$$

and

$$[\text{Resolution}]_{\text{LE}} \approx 1.22\left(\frac{\lambda_c}{D}\right)\frac{\sqrt{\dfrac{\exp\left(-2\sigma^2_{\text{figure}}\right)}{1+4.94\left(\frac{D}{\lambda_c}\right)^2\sigma^2_{\text{tilt}}} + \dfrac{\left[1-\exp\left(-\sigma^2_{\text{figure}}\right)\right]^2}{1+\left[D/\rho_0^{\text{LE}}\right]^2}}}{[\text{Strehl}]_{\text{LE}}}, \tag{2-50}$$

where the tilt error for the large-phase error limit has been included in the long-exposure coherence length, ρ_0^{LE}. According to Yura [14], the long-exposure coherence length is approximately equal to r_0;

$$\rho_0^{\text{LE}} \approx r_0 \tag{2-51}$$

and the short-exposure coherence length is always somewhat larger;

$$\rho_0^{\text{SE}} \approx r_0\left[1+0.37\left(r_0/D\right)^{1/3}\right] . \tag{2-52}$$

The application of this somewhat unorthodox approach to beam characterization can be demonstrated in a short discussion of fitting error effects resulting from low-resolution phase conjugation. Several investigators have claimed that near diffraction-limited resolution can be achieved with only a few actuators [6], arguing that the long-exposure beam profile will always consist of a sharp central peak surrounded by a diffuse background. This statement is valid as long as the tracking system can reliably discriminate between the main lobe of the beam and the competing speckles in the short-exposure image. Consider, for example, the two short-exposure profiles shown in Figure 12, which represent the output of a ray-trace simulation incorporating a compensation system in which the ratio of the actuator spacing to the turbulence coherence length was changed from 1.8 to 2.5. In the latter case, the transition out of the Maréchal regime has begun; it is much more difficult to unambiguously locate and track the central lobe. As indicated in Figure 13, the effective short-exposure beamwidth is clearly turbulence-dominated as soon as the phase error exceeds 4 rad^2 ($d_s/r_0 \approx 3.5$). Note that the simulation results are in good agreement with Equation (2-48).

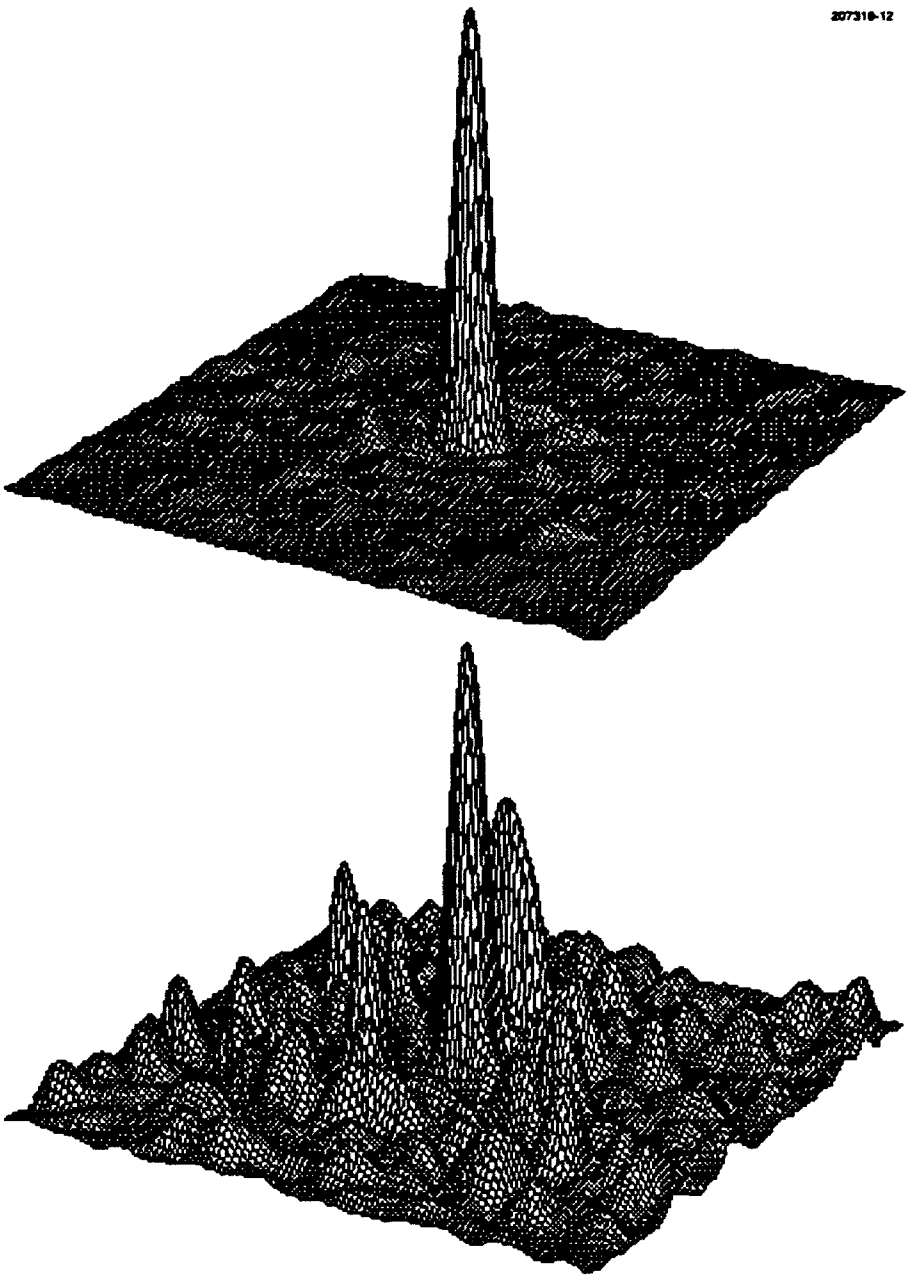

Figure 12. Comparison of short-exposure beam profiles near the transition to strong phase distortion. This simulation was performed for an aperture diameter of 4 m and an r_0 of 16 cm. The upper figure represents a d_f/r_0 of 1.8, for which a Strehl of 0.2 was obtained. The lower figure corresponds to a d_f/r_0 of 2.5 and a Strehl of 0.03. (The vertical scale for the lower figure has been multiplied by a factor of 5.)

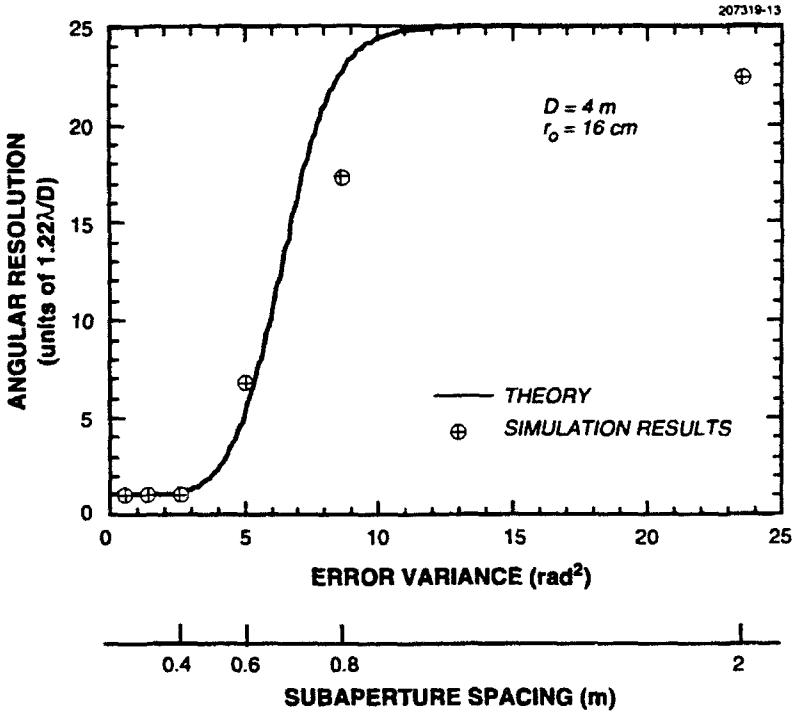

Figure 13. Comparison of the predicted short-exposure resolution with far-field beam-profile measurements derived from a ray-trace simulation; Kolmogorov phase screens were compensated with a zonal-type adaptive element having a variable actuator spacing. Each simulation result represents the average over 5 independent screens that were each adjusted to produce an r_0 of 16 cm over a 4-m aperture.

3. LASER GUIDE-STAR CONCEPTS

The efficacy of adaptive optics has been repeatedly demonstrated in laboratory and field experiments conducted within the defense community over the last 15 years. At this point there is little doubt that well-compensated images can be obtained with ground-based telescopes, provided that the object is bright enough to supply a few hundred photoelectrons to each subaperture per dwell time. For a nominal set of conditions (a 16-cm subaperture, 5-msec dwell time, and a 20 percent throughput), this corresponds to an input flux of order 10^7 photons/m^2-sec, which is roughly equivalent to a magnitude 7 object for visible observations. This limitation would obviously exclude many objects of interest to astronomers.

The concept of using synthetic sources for turbulence sensing was first proposed to the high-energy-laser beam-control community in 1982 [1]. Shortly thereafter, a classified program was initiated to investigate the theory and implementation of adaptive-optics devices incorporating artificial beacons. Lincoln Laboratory was one of several organizations involved in that effort and, to the best of our knowledge, obtained the first experimental evidence of laser guide-star compensation in the summer of 1988 [4]. By the spring of 1991, Strehl ratios exceeding 0.3 were routinely obtained in the visible with a 60-cm telescope and a 241-actuator adaptive-optics system. Figure 14 shows an example of pre- and post-compensation data of the star Procyon. In this experiment the wavefront sensor was driven by a beacon produced by a 512-nm dye laser, the return from which was range-gated at 6 km.

Within the astronomy community, an independent research effort has been active since 1985 [2], and in the last few years the literature on this subject has expanded considerably [23–31]. Although many of the important system design considerations have already been discussed in these articles, the previous treatments have been largely qualitative. This section will provide a quantitative treatment of the performance limitations that arise from a variety of anisoplanatic effects.

3.1 FOCAL ANISOPLANATIC ERRORS PRODUCED BY A SINGLE ARTIFICIAL BEACON

Anisoplanatic errors will occur in any sampling geometry in which the measured turbulence path does not coincide with the path followed by the image radiation. As indicated in Figure 15, light rays originating from a distant source propagate along parallel lines to the receiver aperture. The measurement of accumulated phase distortion afforded by a laser guide star is inherently imperfect as a result of unsampled turbulence above the beacon and incorrectly sampled turbulence below the beacon. This form of error is referred to as focal anisoplanatism, because it results from a difference in range between the beacon and the celestial object.

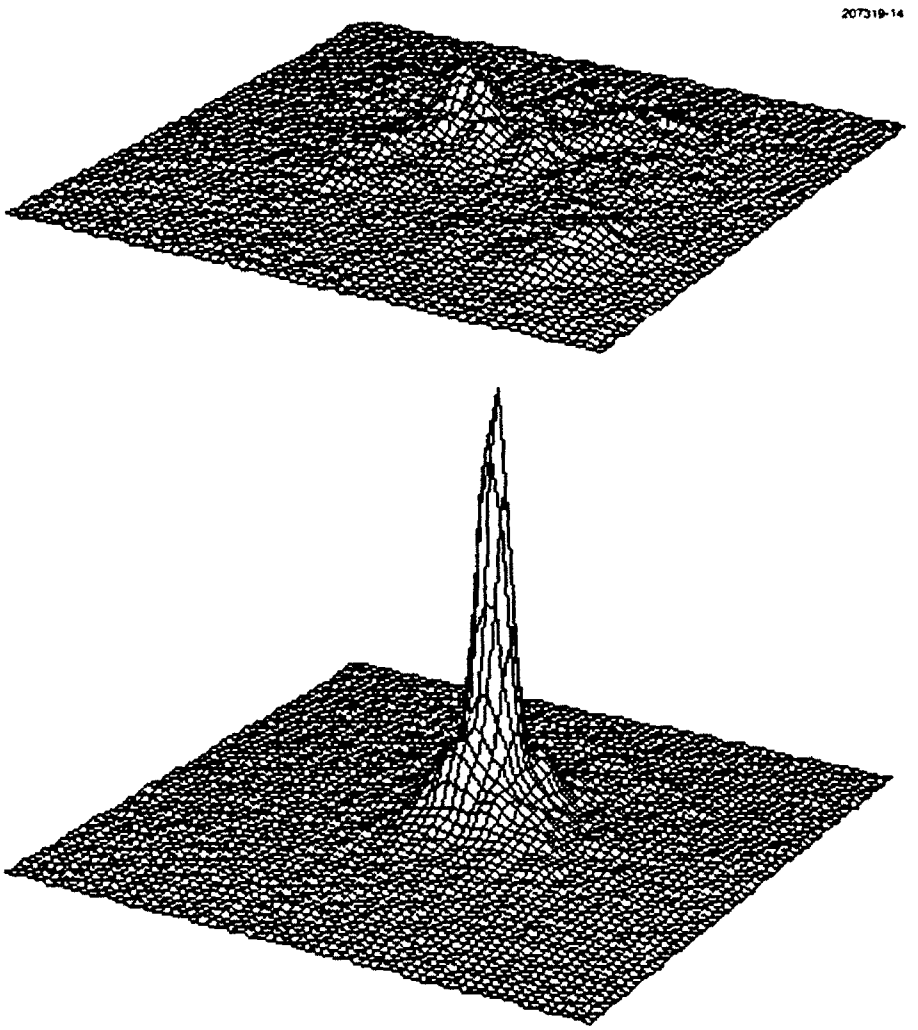

Figure 14. Short-exposure visible-wavelength images of Procyon taken in February 1991 with the 60-cm telescope operated by Lincoln Laboratory at Maui. The upper picture is a 1-msec exposure taken with a CCD camera having a 19-μrad field of view. The lower image was collected a millisecond later after the phase distortion had been corrected with a 241-actuator deformable mirror. A 512-nm synthetic probe placed at an altitude of 6 km was used to measure the turbulence-induced phase distortion. The estimated Strehl ratios for the uncompensated and compensated images are 0.05 and 0.4, respectively.

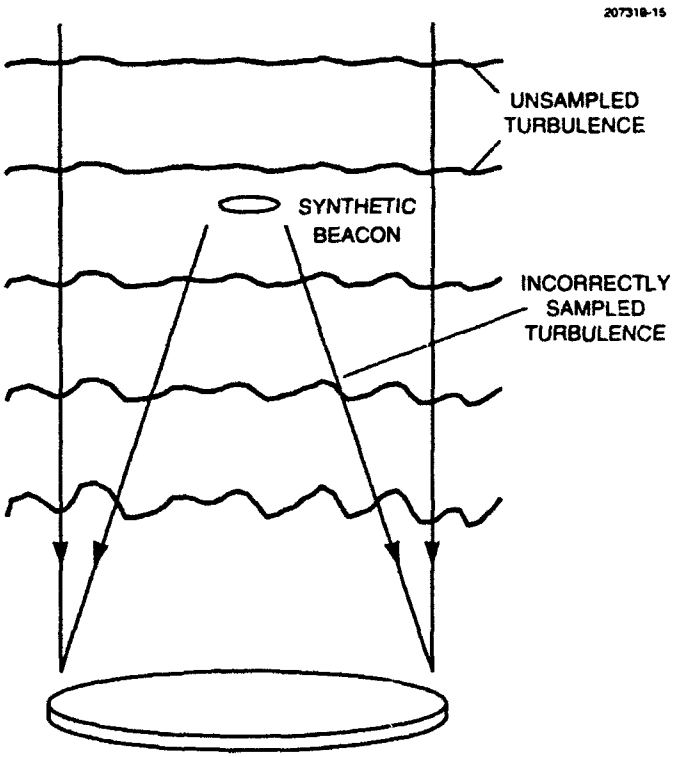

Figure 15. Illustration of the two major sources of phase error introduced by laser guide-star sources. The vertical rays represent light originating from a distant source that accumulates phase error in traveling through the atmosphere. The beacon rays follow slightly different paths to the receiver and are unable to sample the turbulence above the beacon or to properly sample the turbulence below the beacon.

An analytic description of phase errors associated with anisoplanatic effects is most easily obtained by developing the appropriate ensemble averages of the phase structure function in the pupil plane of the receiver. An approach developed by Sasiela [32] leads to error-variance expressions having the following general form:

$$\sigma^2 = 0.207 k_c^2 \int_0^\infty C_n^2(z) \left\{ \int f(\kappa) g(\bar{\kappa}, z) d\bar{\kappa} \right\} dz \quad , \tag{3-1}$$

where the z integration is performed over the slant range from the receiver to the object and the κ integration is taken over the entire two-dimensional space of the pupil plane. $f(\kappa)$ is the turbulence spectrum, which, for most problems, is assumed to be the normalized Kolmogorov spectrum

$$f(\kappa) = \kappa^{-11/3} \quad . \tag{3-2}$$

The turbulence-sensing geometry is characterized by the filter function, $g(\bar{\kappa}, z)$, and will be unique to each problem. As an example, consider the residual phase error for a system in which the aperture-averaged tilt is removed. The filter function that eliminates the average phase (piston) and the x- and y-tilt over an aperture of diameter D is

$$g(\kappa)_{\text{figure}} = 1 - \left[\frac{2J_1(\kappa D/2)}{\kappa D/2}\right]^2 - \left[\frac{4J_2(\kappa D/2)}{\kappa D/2}\right]^2 , \tag{3-3}$$

from which the following expression is obtained:

$$\begin{aligned}\sigma^2_{\text{figure}} &= 1.30 k_c^2 \int_0^\infty C_n^2(z)dz \int_0^\infty \kappa^{-8/3}\left\{1 - \left[\frac{2J_1(\kappa D/2)}{\kappa D/2}\right]^2 - \left[\frac{4J_2(\kappa D/2)}{\kappa D/2}\right]^2\right\} d\kappa \\ &= 0.057 \sec(\zeta) k_c^2 D^{5/3} \mu_0 = 0.134\left(D/r_0\right)^{5/3}\end{aligned} \tag{3-4}$$

The figure error associated with the uncorrected turbulence above the beacon is derived directly from Equation (3-4) by setting the lower limit of the integral over z to the beacon altitude, H. If the n^{th} upper turbulence moment is defined to be

$$\mu_n^{\uparrow}(H) = \int_H^\infty h^n C_n^2(h)dh , \tag{3-5}$$

the error due to the unsampled turbulence can be written as

$$\sigma^2_{\text{upper}} = 0.057 D^{5/3} k_c^2 \sec(\zeta) \mu_0^{\uparrow}(H) . \tag{3-6}$$

The phase error below the beacon arises from the difference between the parallel rays traveling between the scattering altitude and the ground and the rays originating from the beacon. In this case, the filter function is somewhat more complicated and leads to the expression

$$\begin{aligned}\sigma^2_{\text{lower}} = 1.30 k_c^2 \sec(\zeta) \int_0^\infty dz C_n^2(z) \int_0^H d\kappa\, \kappa^{-8/3} \Bigg\{ 2\left[1 - \frac{J_1(\kappa D(H-z)/2H)}{\kappa D(H-z)/2H}\right] \\ - \left[\frac{2J_1(\kappa D/2)}{\kappa D/2} - \frac{2J_1(\kappa D(H-z)/2H)}{\kappa D(H-z)/2H}\right]^2 - \left[\frac{4J_2(\kappa D/2)}{\kappa D/2} - \frac{4J_2(\kappa D(H-z)/2H)}{\kappa D(H-z)/2H}\right]^2 \Bigg\} .\end{aligned} \tag{3-7}$$

The solution is most easily expressed as a series expansion involving the low-altitude turbulence moments, $\mu_n^{\downarrow}(H)$, computed from ground level to the beacon. An accurate representation can be obtained with the first two expansion terms

$$\sigma^2_{\text{lower}} \approx D^{5/3} k_c^2 \sec(\zeta) \left\{ 0.500 \frac{\mu_{5/3}^{\downarrow}(H)}{H^{5/3}} - 0.452 \frac{\mu_2^{\downarrow}(H)}{H^2} + \cdots \right\} . \tag{3-8}$$

Note that both the low- and high-altitude equations exhibit an explicit $D^{5/3} k_c^2 \sec(\zeta)$ dependence that is decoupled from the beacon altitude and turbulence profile dependencies contained in the expansion series.

The predicted focal anisoplanatic error for visible imaging with a 4-m aperture is plotted as a function of beacon altitude in Figure 16. A single beacon placed at 10 km should reduce the figure error to about 3 rad^2, which (based on the analysis of resolution shown earlier in Figure 13) is just within the range in which a unique diffraction-limited central lobe would be formed. A 90-km source would yield an image having a much higher signal-to-clutter ratio and would produce a Strehl ratio of approximately 0.6.

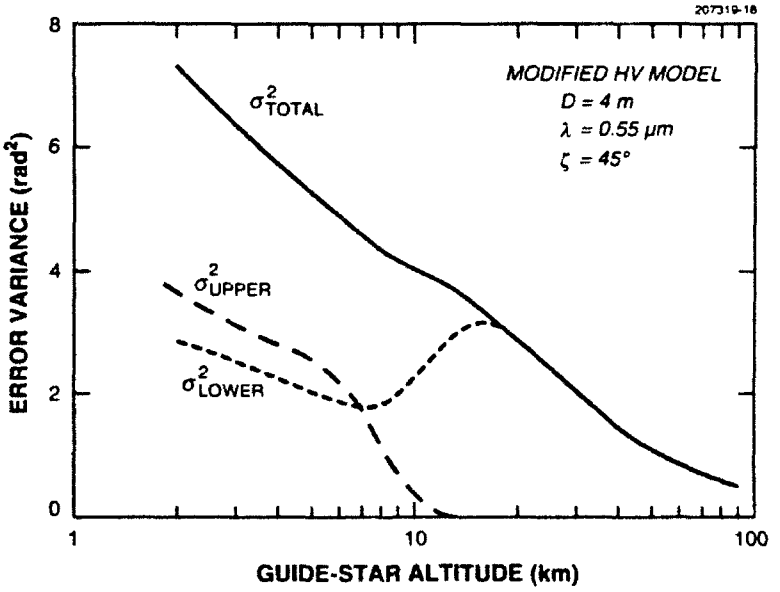

Figure 16. Comparison of phase variance contributions due to turbulence lying above and below the synthetic beacon. The shape of the low-altitude curve is complicated by the inclusion of a larger fraction of the atmosphere as the beacon is raised.

3.2 IMPLEMENTATION AND PERFORMANCE OF MULTIPLE-BEACON SYSTEMS

The efficacy of systems employing a single synthetic beacon came into question fairly early in Lincoln's investigation of guide-star techniques and subsequently led to the development of a variety of alternate beacon geometries. Because the figure error due to focal anisoplanatism has been shown to have a $D^{5/3}$ dependence, there is a potential benefit in deploying multiple beacons, each of which would be devoted to correcting one section of the complete aperture. This concept is illustrated in Figure 17. If a total of N_b artificial sources were to be employed, the effective collection aperture for the residual turbulence below the beacons would be reduced by a factor of $N_b^{-1/2}$, so that

$$\sigma^2_{\text{lower}} \approx N_b^{-5/6} D^{5/3} k_c^2 \sec(\zeta) \left\{ 0.500 \frac{\mu^{\downarrow}_{5/3}(H)}{H^{5/3}} - 0.452 \frac{\mu^{\downarrow}_{2}(H)}{H^{2}} + \cdots \right\}. \qquad (3\text{-}9)$$

Unfortunately, the practical implementation of this scheme is far from trivial, and the following issues are noted.

1) In order to mate the aperture sections to their respective beacons, a discrimination approach using time delay, color, polarization, or field-of-view must be employed so that the signals from the wavefront sensor can be correctly processed. If the beacons are launched sequentially in time, the entire pattern must be generated within the atmospheric time constant.

2) Because wavefront sensors measure phase gradients rather than absolute phase, a means must be developed to measure gradients across the seams between the aperture sections. To accomplish this "stitching" process, the detectors at the edges of the section seams must be capable of measuring the light from both of the neighboring sources. If the beacons are launched in parallel, this may necessitate the use of multiple sensors with overlapping fields-of-view.

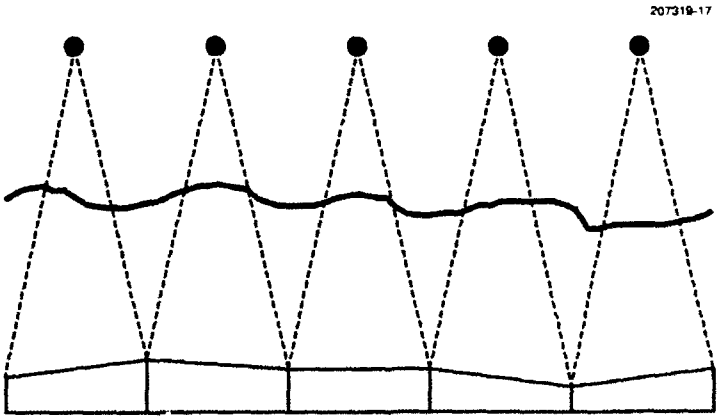

Figure 17. Multiple-beacon sampling geometry. Focal anisoplanatism is reduced by positioning a beacon over the center of each mirror section. "Stitching" errors occur when the relative source positions cannot be accurately determined and result in low spatial-frequency figure distortions.

The section-stitching issue has been studied at some length within the beam-control community, and there is still considerable doubt as to the ability of multiple-beacon arrays to produce results that are significantly better than those achievable with single-beacon systems. The basic problem arises from the need to accurately fix the relative positions of the sources at the scattering layer. Figure 17 illustrates the ideal geometry in which each of the beacons lies directly above the center of its respective section. If one of the spots were to be laterally displaced within this pattern, however, all the subapertures within its section would measure an anomalous tilt that would result in a low spatial-frequency distortion of the reconstructed phase. Such displacements can be expected to occur as a result of imperfections in the beacon-projection system; on a more fundamental level, fluctuations in position are unavoidable due to the the fact that each beam is projected through a slightly different turbulence path. The use of overlapping gradient measurements can reduce this effect, but there will always be a non-correctable error component.

The uncorrectable part of the stitching error is best described in the context of a measurement process that attempts to map the actual beacon positions by allowing each section to simultaneously view every source. In the absence of turbulence, this mapping process would be error-free. When the atmosphere is present, however, non-zero tilt measurements resulting from source displacements become confused with turbulence-induced tilt differences.

A detailed evaluation of the multiple-beacon phase-reconstruction process shows that the net residual is related to the difference between the section tilts obtained from the artificial beacon array and the target object. To perform this calculation, the section-tilt variance due to focal anisoplanatism must be determined and the cumulative effect of this error over an aperture having a large number of sections must be estimated. The first of these calculations is performed by applying the filter function for aperture-tilt to Equation (3-1). For a section having a diameter, D_s, the appropriate filter function is

$$g(\kappa)_{\text{tilt phase}} = \left[\frac{4J_2(\kappa D_s/2)}{\kappa D_s/2}\right]^2 , \tag{3-10}$$

which leads to the following expansion for the tilt error due to turbulence below the beacon:

$$\sigma^2_{\text{tilt phase}} \approx D_s^{5/3} k_c^2 \sec(\zeta)\left\{0.368\frac{\mu_2^{\downarrow}(H)}{H^2} + \cdots\right\} . \tag{3-11}$$

An evaluation of the net error over the full aperture requires knowledge of the correlation statistics of these fluctuations. (If the section-tilt errors were perfectly correlated, no high spatial-frequency distortions would be produced and the figure error would be unaffected.) This correlation matrix has been evaluated, and in Section B.3 of Appendix B the error propagator for a system having a large number of beacons is shown to be approximately equal to $0.11(D/D_s)^{5/3}$. Therefore, the stitching component of the figure error is

$$\sigma^2_{\text{stitching}} \approx D^{5/3} k_c^2 \sec(\zeta)\left\{0.040\frac{\mu_2^{\downarrow}(H)}{H^2} + \cdots\right\} , \tag{3-12}$$

which has the same $D^{5/3} k_c^2 \sec(\zeta)$ dependence found in the previous error-variance expressions and is independent of the number of sections.

As suggested by Equation (3-9), it is possible in principle to reduce the low-altitude anisoplanatism term to a negligible level by deploying a sufficient number of synthetic beacons. In the limiting case, the major contributors to the total error would be upper-altitude anisoplanatism and section-stitching noise. This result is shown in Figure 18, and in comparison with Figure 16 it can be seen that a significant error reduction is predicted for all beacon altitudes. However, this improvement must be carefully balanced against the increased complexity of the laser system, wavefront sensor, and phase reconstructor.

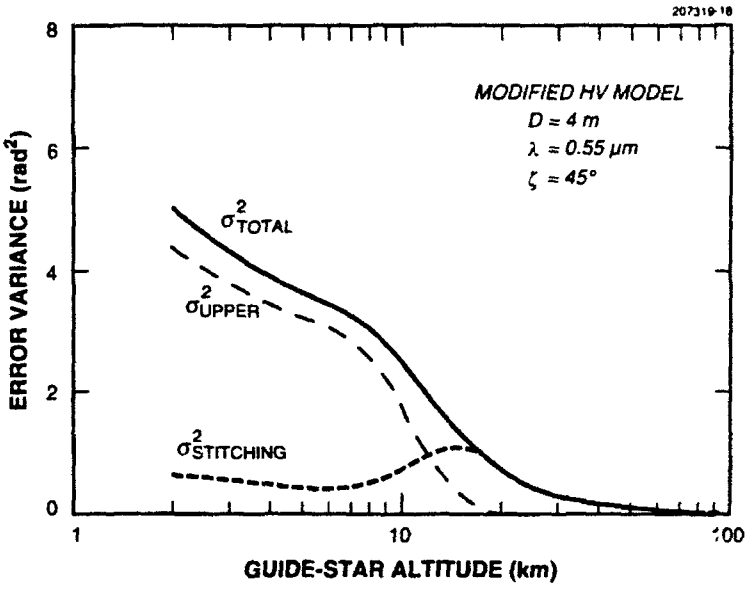

Figure 18. Figure error expected for the combination of unsampled upper-altitude turbulence and aperture-section stitching with multiple beacons.

The practical implementation of the stitching concepts just described has been demonstrated by Lincoln Laboratory in a four-beacon laboratory simulation performed in 1988 and in a two-beacon field experiment in November 1990 [5]. In the latter experiment, a pair of pulsed dye lasers was used to generate sources that were separated in time by approximately 1 msec and displaced laterally by half the diameter of the aperture. In both of these tests, a small improvement in the far-field Strehl was recorded when the multiple-beacon images were compared with the single-beacon results

3.3 LONG-EXPOSURE TRACKING CONSIDERATIONS

All synthetic-beacon concepts suffer from a common deficiency—because the laser radiation follows the same turbulence path in both the transmit and backscatter directions, no information can be gained about the probe position relative to the target object. Unless the error due to turbulence-induced tilt jitter can be sensed and eliminated, the long-exposure image obtained with guide-star figure correction will be no better than that produced by an uncompensated receiver.

For imaging engagements in which exposures much longer than the atmospheric time constant are required, it will be necessary to stabilize the imaging system on an exoatmospheric fiducial object that is within the isoplanatic angle for overall tilt. Recall that the standard definition for isoplanatic angle is

$$\theta_0 = \left\{2.91 k_c^2 \sec^{8/3}(\zeta) \mu_{5/3}\right\}^{-3/5}, \tag{3-13}$$

which is based on the following description of the phase error resulting from two beam paths separated by an angle θ:

$$\left(\sigma^2_{\text{figure}}\right)_{\text{beacon offset}} = \left(\theta/\theta_0\right)^{5/3}. \tag{3-14}$$

Sasiela [32] has derived an expression for the error variance associated with overall tilt, where in this case the aperture filter function is

$$g(\kappa, z)_{\text{tilt anisoplanatism}} = \left[\frac{8}{(k_c D)^2}\right]\left[\frac{4J_2(\kappa D/2)}{\kappa D/2}\right]^2 \left[2 - 2J_0(\kappa\theta z)\right]. \tag{3-15}$$

This expression represents the product of three terms: the first is a conversion from phase variance to single-axis angular tilt, the second is the tilt filter function introduced in Equation (3-10), and the third is the function for angular offset. The resulting error (in units of rad^2 of single-axis tilt) is approximately given by

$$\left(\sigma^2_{\text{tilt}}\right)_{\text{beacon offset}} \approx \sec(\zeta) D^{-1/3}\left\{5.34 \mu_2^{\downarrow}(H_c)\left(\frac{\theta \sec(\zeta)}{D}\right)^2 + 6.08 \mu_0^{\uparrow}(H_c)\right\}, \tag{3-16}$$

where $H_c = D/\theta \sec(\zeta)$ is the altitude at which the two beam paths no longer overlap. The first term of this series is usually adequate as long as H_c is greater than 10 km.

Combining the first term of Equation (3-16) with Equation (2-50) yields the long-exposure resolution for tilt anisoplanatism:

$$[\text{Resolution}]_{\text{LE}} = 1.22\left(\frac{\lambda_c}{D}\right)\sqrt{1 + 4.94\left(\frac{D}{\lambda_c}\right)^2 \left(\sigma^2_{\text{tilt}}\right)_{\text{beacon offset}}} \approx 1.22\left(\frac{\lambda_c}{D}\right)\sqrt{1 + \left[\frac{\theta}{(\theta_0)_{\text{tilt}}}\right]^2}, \tag{3-17}$$

where the isoplanatic angle for tilt is defined to be

$$(\theta_o)_{tilt} = \left\{0.668 k_c^2 \sec^3(\zeta) \mu_2 D^{-1/3}\right\}^{-1/2} \quad . \tag{3-18}$$

For a set of nominal system parameters (D = 4 m, λ_c = 0.55 μm, and ζ = 45°) and the modified HV turbulence model, $(\theta_0)_{tilt} \approx 40$ μrad; this number is only a factor of 3.5 larger than θ_0 for these conditions.

A plot of the long-exposure resolution, developed from Equations (3-16) and (3-17), is given in Figure 19. This curve displays a linear dependence on the separation angle when $\theta/(\theta_0)_{tilt}$ is between 1 and 6, but for larger values of θ an asymptotic limit is reached that is $\sqrt{2}$ larger than the single-beam tilt jitter for uncompensated turbulence.

This research indicates that a guide-star compensation system must comprise two separate, and equally essential, servo elements—a deformable mirror controlled by the laser beacon and a tracking mirror slaved to a bright fiducial star. The probability of finding a suitable fiducial object within the tilt isoplanatic angle will be addressed in the next section.

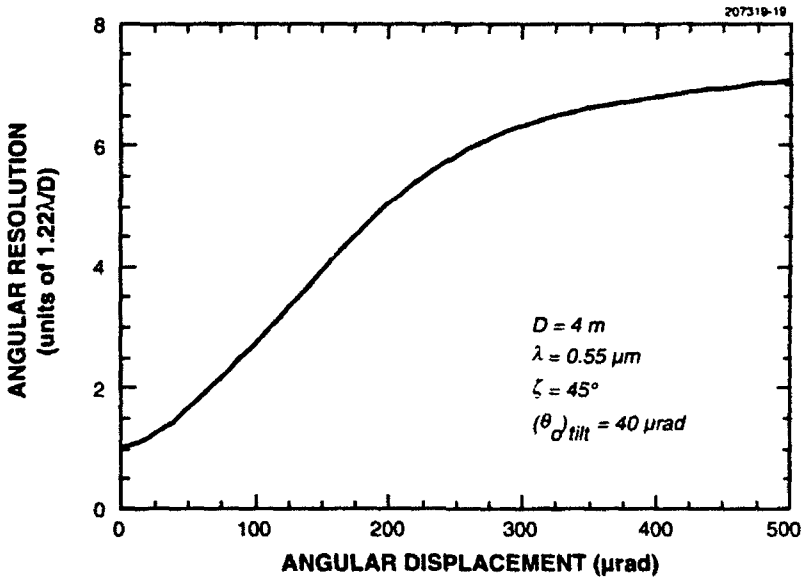

Figure 19. Resolution as a function of angular displacement between the target object and the fiducial star. This function is approximately linear between 50 and 250 μrad.

4. OPTIMIZATION AND PERFORMANCE ANALYSIS FOR A 4-m SYSTEM

At this point, an optimized telescope design may be proposed and its performance characteristics analyzed. To motivate the need for synthetic beacons, brightness requirements will also be developed for celestial objects.

To simplify this analysis, a baseline system configuration will be used for all calculations that follow. The list of parameters, given in Table 2, includes a 4-m aperture, a viewing angle of 45°, and a common wavelength of 0.55 μm for wavefront sensing, tracking, and imaging. The sensor characteristics of an 80 percent quantum efficiency and 20 noise electrons are nominal for high-frame-rate CCD camera systems.

Note also that a total throughput parameter, γ, will appear in all of the error expressions in this section so that the computed irradiance values can be referenced to the top of the atmosphere. Estimates of throughput can vary greatly and will depend on the complexity of the collection system and the manner in which the light is apportioned between the various sensors. For the purpose of this study a value of 20 percent will be used for both the phase sensor and tracking systems.

Unless otherwise stated, the parameters listed in Table 2 should be assumed for all numerical results.

4.1 OPTIMIZATION OF SUBAPERTURE DIMENSION AND DWELL TIME

The three most important sources of error for conventional (non-guide-star) adaptive-optics systems have been shown to be fitting error, phase-sensor noise, and finite-bandwidth error. By combining Equations (2-25) and (2-41), the residual figure distortion for a system that senses wavefront phase at a wavelength λ_p and images at wavelength λ_c is obtained. Thus,

$$\left(\sigma^2_{\text{figure}}\right)_{\text{system}} \approx \underbrace{0.5\left(d_s/r_0\right)^{5/3}}_{\text{fitting error}} + \underbrace{0.962\left(\tau_d/\tau_0\right)^{5/3}}_{\text{finite bandwidth error}} + \underbrace{\frac{2\left(hck_c\right)^2\left[1+\left(\frac{k_p}{k_c}\right)^{12/5}\left(\frac{d_s}{r_0}\right)^2\right]N^2_{\text{rms}}}{3\left(\gamma_p\,\eta\,\tau_d\,d_s^2\,I_p\right)^2}}_{\text{sensor noise}}$$

$$(\text{rad}^2 \text{ of phase}) . \qquad (4\text{-}1)$$

TABLE 2

Baseline System Parameters for Optimization Study

Aperture Diameter	$D = 4$ m
Wavelength	$\lambda_p = \lambda_t = \lambda_c = 0.55$ μm
Zenith Angle	$\zeta = 45°$
Total System Throughput	$\gamma_p = \gamma_t = 0.2$
Detector Quantum Efficiency	$\eta = 0.8$
Detector Noise Level	$N_{rms} = 20$
Turbulence Parameters	$r_0 = 16.2$ cm $\theta_0 = 11.5$ μrad $\tau_0 = 5.1$ msec $(\theta_0)_{tilt} = 40.3$ μrad $(\tau_0)_{tilt} = 12.3$ msec
Turbulence Moments	$\mu_0 = 2.65 \times 10^{-13} m^{1/3}$ $\mu_{5/3} = 1.78 \times 10^{-7} m^2$ $\mu_2 = 3.96 \times 10^{-6} m^{7/3}$
Wind Velocity Moments	$\upsilon_{-1/3} = 1.40 \times 10^{-13} sec^{1/3}$ $\upsilon_{5/3} = 1.23 \times 10^{-11} m^2\text{-}sec^{5/3}$ $\upsilon_{14/3} = 2.28 \times 10^{-7} m^5\text{-}sec^{14/3}$

The optimization of the subaperture dimension and phase sensor dwell time is simplified if the third term in Equation (4-1) is rewritten for the limit $d_s \gg r_0$. A general treatment of this problem is given in Section C.4 of Appendix C, and from Equation (C-20) it can be shown that the relative contributions of the three error terms appearing in Equation (4-1) are $\frac{6}{17}$, $\frac{6}{17}$, and $\frac{5}{17}$, respectively. For a specified figure-variance design goal, the following set of system characteristics is developed:

$$d_s/r_0 = 0.811\left[\left(\sigma^2_{\text{figure}}\right)_{\text{system}}\right]^{3/5}, \tag{4-2}$$

$$\tau_d/\tau_0 = 0.548\left[\left(\sigma^2_{\text{figure}}\right)_{\text{system}}\right]^{3/5}, \tag{4-3}$$

and

$$I_p = \frac{3.39\, hc\, k_c^{-1/5}\, k_p^{6/5}\, N_{rms}}{\gamma_p\, \eta\, \tau_o\, r_o^2 \left[\left(\sigma^2_{\text{figure}}\right)_{\text{system}}\right]^{17/10}} \left\{1 + 1.52\left(\frac{k_c}{k_p}\right)^{12/5} \left[\left(\sigma^2_{\text{figure}}\right)_{\text{system}}\right]^{-6/5}\right\}^{1/2} . \quad (4\text{-}4)$$

The last of these equations can be rewritten to show the explicit dependence on the number of photoelectrons collected by each subaperture

$$\frac{\left(N_{pe}\right)_{\text{phase sensor}}}{N_{rms}} = 7.68\left(\frac{k_p}{k_c}\right)^{1/5} \left[\left(\sigma^2_{\text{figure}}\right)_{\text{system}}\right]^{1/10} \left\{1 + 1.52\left(\frac{k_c}{k_p}\right)^{12/5} \left[\left(\sigma^2_{\text{figure}}\right)_{\text{system}}\right]^{-6/5}\right\}^{1/2} .$$

(4-4')

These expressions indicate that d_s/r_0 and τ_d/τ_0 will typically be close to unity and that the number of photoelectrons that must be collected by each subaperture per measurement interval will be on the order of a few hundred. A plot of d_s and τ_d as a function of the allowed figure error is given in Figure 20.

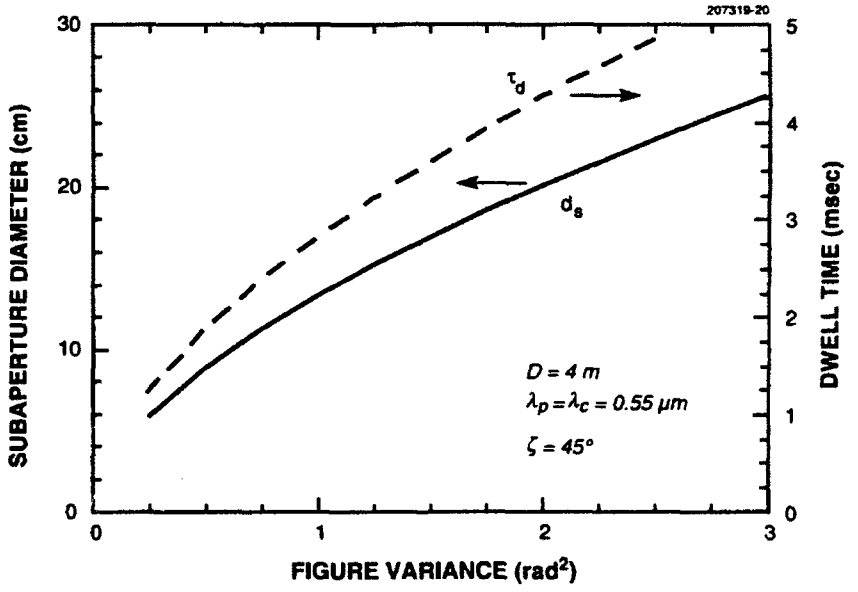

Figure 20. Optimization analysis of the phase-compensation system parameters as a function of figure variance. A total throughput value of 20 percent has been assumed in this calculation.

The tracking-system dwell time can be optimized in a similar fashion, although in this case it will be assumed that the bandwidth of the tilt sensor is low enough to permit photon-noise-limited operation. From Equation (2-43),

$$\left(\sigma^2_{\text{tilt}}\right)_{\text{system}} \approx \underbrace{0.202\left(\frac{\lambda_c}{D}\right)^2\left[\frac{\tau_{dt}}{\left(\tau_0\right)_{\text{tilt}}}\right]^2}_{\text{finite bandwidth error}} + \underbrace{\frac{8\,hc\,k_c^{-12/5}\,k_t^{7/5}}{3\,\gamma_t\,\eta\,\tau_{dt}\,r_0^2\,D^2\,I_t}}_{\text{photon noise}} \text{ (rad}^2 \text{ of single-axis tilt)}, \quad (4\text{-}5)$$

where a critical time constant for tilt has been defined following the procedure used earlier to develop the tilt isoplanatic angle:

$$\left(\tau_0\right)_{\text{tilt}} = \left\{0.512 k_c^2 \sec(\zeta) v_{-1/3}^{8/15} v_{14/3}^{7/15} D^{-1/3}\right\}^{-1/2} . \quad (4\text{-}6)$$

When the dwell time is properly adjusted, the relative contributions of the two error terms in Equation (4-5) will be $\frac{1}{3}$ and $\frac{2}{3}$, respectively. Thus,

$$\frac{\tau_{dt}}{\left(\tau_0\right)_{\text{tilt}}} = 0.784\left[\frac{\left(\sigma^2_{\text{tilt}}\right)_{\text{system}}}{\left(0.61\lambda_c/D\right)^2}\right]^{1/2} \quad (4\text{-}7)$$

represents the optimal setting, where the jitter radius has been normalized to the half-width of the diffraction-limited beam at the compensation wavelength. The tracker irradiance requirement is

$$I_t = 19.5\,\frac{hc\,k_c^{-17/5}\,k_t^{7/5}}{\gamma_t\,\eta\left(\tau_0\right)_{\text{tilt}}\,r_0^2\,D^3\left[\left(\sigma^2_{\text{tilt}}\right)_{\text{system}}\right]^{3/2}} , \quad (4\text{-}8)$$

and at this level the detector will collect the following number of photoelectrons within a single measurement cycle:

$$\left(N_{pe}\right)_{\text{tracker}} = 1.71\left(\frac{k_t}{k_c}\right)^{2/5}\left(\frac{D}{r_0}\right)^2\left[\frac{\left(\sigma^2_{\text{tilt}}\right)_{\text{system}}}{\left(0.61\lambda_c/D\right)^2}\right]^{-1} . \quad (4\text{-}8')$$

Once again the dwell time must be roughly matched to the atmospheric time constant if good performance is to be achieved and the requisite photoelectron count is of the order of a few hundred.

4.2 PERFORMANCE EXPRESSIONS FOR THE OPTIMIZED SYSTEM DESIGN

By reformulating the optimization equations to express them in terms of source irradiance and combining them with their respective error expressions, a compact set of variance relationships is obtained;

$$\left(\sigma^2_{\text{figure}}\right)_{\text{system}} \approx 2.05(hc)^{10/17}\, k_c^{-2/17}\, k_p^{12/17} \left(N_{\text{rms}}/\gamma_p\, \eta\, \tau_0\, r_0^2\, I_p\right)^{10/17}$$

$$(\text{rad}^2 \text{ of phase}), \tag{4-9}$$

and

$$\left(\sigma^2_{\text{tilt}}\right)_{\text{system}} \approx 7.25(hc)^{2/3}\, k_c^{-34/15}\, k_t^{14/15} \left(\gamma_t\, \eta \left(\tau_0\right)_{\text{tilt}}\, I_t\right)^{-2/3} r_0^{-4/3}\, D^{-2}$$

$$(\text{rad}^2 \text{ of single-axis tilt}). \tag{4-10}$$

Quantitative estimates of the long-exposure Strehl and resolution follow from Equations (2-49) and (2-50), which can be simplified if the system is assumed to operate in the range in which the extended Maréchal approximation is valid ($\sigma^2_{\text{figure}} < 3$ rad^2), with the result

$$[\text{Strehl}]_{\text{LE}} \approx \frac{\exp\left(-\sigma^2_{\text{figure}}\right)}{1 + 4.94\left(\dfrac{D}{\lambda_c}\right)^2 \sigma^2_{\text{tilt}}} \tag{2-49'}$$

and

$$[\text{Resolution}]_{\text{LE}} \approx 1.22\left(\frac{\lambda_c}{D}\right)\sqrt{1 + 4.94\left(\frac{D}{\lambda_c}\right)^2 \sigma^2_{\text{tilt}}}\ . \tag{2-50'}$$

A plot of these functions for $I_p = I_t$ is given in Figure 21. The equivalent stellar magnitude is also given for wideband sensing in the visible, where the relationship

$$m_v = -2.5 \log(I) - 21.2 \tag{4-11}$$

has been applied.

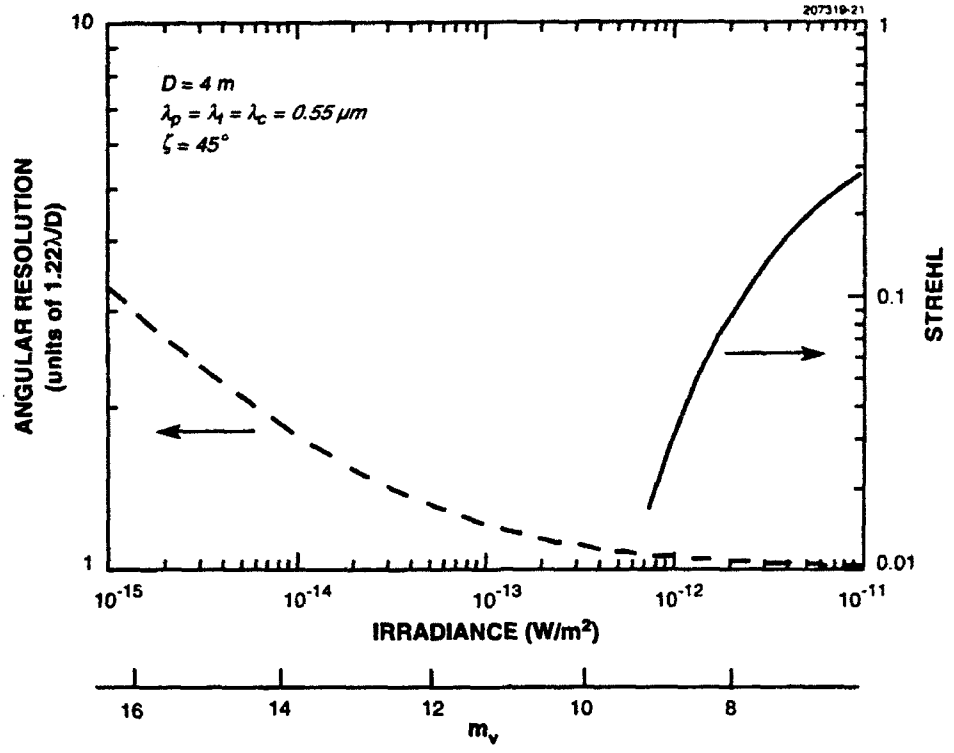

Figure 21. Performance analysis of the optimized figure- and tilt-compensation systems as a function of irradiance (referenced to the top of the atmosphere). A total throughput value of 20 percent has been assumed for both systems.

4.3 SKY-COVERAGE CALCULATIONS FOR NATURAL SOURCES

The conclusion that can be drawn from Figure 21 is that phase compensation at visible wavelengths requires relatively bright objects ($m_v < 9$), whereas high-precision tracking can be performed with stars much dimmer than 16th magnitude. In this context the advantage of guide-star compensation becomes obvious, as a natural source is only required to close the tracking loop. In order to quantify the expected improvement, it will be useful to obtain estimates of the fraction of the sky that can be covered with natural and synthetic beacons. The fractional sky coverage is defined to be

$$\text{Fractional Sky Coverage} = \pi \vartheta^2 \times \text{Average Star Density}\ , \qquad (4\text{-}12)$$

where ϑ represents a radius that can be drawn around each bright star within which the error due to tilt anisoplanatism will be tolerable according to some set of system performance goals.

Star density computations have been performed based on information extracted from the Infrared Handbook [33], which gives average population estimates as well as numbers for the galactic pole and

equator. The resulting density curves as a function of visual magnitude are given in Figure 22. For computational purposes it will be convenient to replace these curves with analytical functions; the following expressions provide an excellent fit for visual magnitudes less than 20:

$$\text{Average Density} = 1.45 \exp(0.96\, m_v) \quad (\text{stars/rad}^2)\,, \tag{4-13}$$

$$\text{Density at Pole} = 1.27 \times 10^{-4} m_v^{8.2} \quad (\text{stars/rad}^2)\,, \tag{4-14}$$

and

$$\text{Density at Equator} = 3.97 \exp(m_v) \quad (\text{stars/rad}^2)\,. \tag{4-15}$$

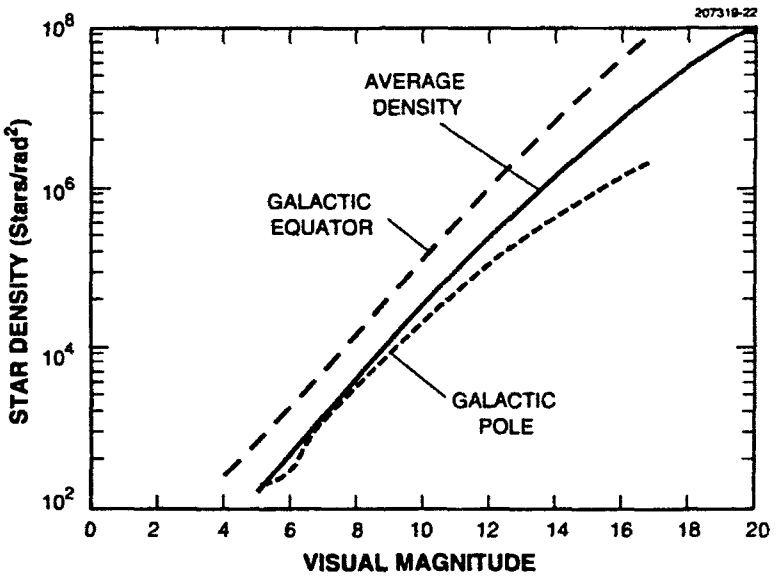

Figure 22. Comparison of stellar densities for the galactic pole, the galactic equator, and the average density as a function of visual magnitude.

Equations (4-11) and (4-13) can be combined to produce a first-order estimate of the average density as a function of irradiance:

$$\text{Average Density} = 2.02 \times 10^{-9}\, I^{-1.04} \quad (\text{stars/rad}^2)\,. \tag{4-16}$$

The area of coverage afforded by each bright star depends on the level of error due to tilt anisoplanatism that can be tolerated. From Equations (3-13) and (3-14) it can be seen that to maintain

a specified figure error of $\left(\sigma^2_{\text{figure}}\right)_{\text{beacon offset}}$, the angular displacement from the beacon must be less than

$$\vartheta_{\text{figure}} = \left[\left(\sigma^2_{\text{figure}}\right)_{\text{beacon offset}}\right]^{3/5} \theta_0 \,. \tag{4-17}$$

This equation is applicable when natural stars are used as the light source for both figure and tilt compensation. When a synthetic beacon is used to drive the wavefront sensor, the fiducial star must be close enough to the target object to sustain a tilt jitter of less than $\left(\sigma^2_{\text{tilt}}\right)_{\text{beacon offset}}$. From Equations (3-16) and (3-18),

$$\vartheta_{\text{tilt}} = 1.36\left[\frac{\left(\sigma^2_{\text{tilt}}\right)_{\text{beacon offset}}}{\left(0.61\lambda_c/D\right)^2}\right]^{1/2} \left(\theta_0\right)_{\text{tilt}} \,. \tag{4-18}$$

4.4 LASER REQUIREMENTS FOR GUIDE-STAR COMPENSATION

The final component of this discussion is an estimate of the power required to generate a laser guide star. The expressions for atmospheric backscatter are well known, and good tutorials on this subject can be found in texts by Hinkley [34] and Measures [35].

In Figure 16 strong evidence is presented for the use of sodium beacons to achieve high-quality phase compensation at visible wavelengths. To fully exploit resonance emission, however, the laser line width must be well matched to the D_2 absorption line (~3 GHz), and saturation effects resulting from the long natural decay time of the excited state (~16 nsec) must be avoided. The second of these parameters results in a limit of about 30 kW/m^2 on the peak-power density of the projected beam [30].

Saturation can be reduced by either increasing the length of the laser pulse or the size of the laser spot within the scattering region. In Lincoln's theoretical studies, virtually no degradation of the quality of the phase measurement was found as long as the projected beam was smaller than the aperture diameter (or the section diameter for a multiple-beacon system). To avoid any degradation of the phase sensor's sensitivity, however, the beacon must not be so large that it becomes resolved by a subaperture. For most scenarios of interest, this latter restriction will establish the practical upper limit on the laser-spot diameter.

Assuming a laser pulse width of 200 μsec and a 50-cm beacon diameter, the limit on the pulse energy would be approximately 1 J. This number is slightly greater than the energy requirement that is derived below for CW operation in the visible; therefore, saturation effects can be neglected for most first-order calculations.

For quasi-CW operation using a high rep-rate beacon laser, the backscattered irradiance from sodium layer measured at the entrance to the wavefront sensor is predicted to be

$$I_p \approx P_\ell \frac{\gamma_\ell C_s \left[d\sigma(\pi)/d\Omega\right]}{\left[\sec(\zeta) H_s\right]^2} \,, \tag{4-19}$$

where

I_p = average irradiance at the wavefront sensor (W/m^2),

P_ℓ = average laser power (W),

γ_ℓ = throughput of the laser beam to the scattering layer = 0.2,

ζ = zenith angle = 45°,

H_s = sodium layer altitude $\approx 9 \times 10^4$ m,

C_s = sodium column abundance $\approx 5 \times 10^{13}$ atoms/m^2, and

$d\sigma(\pi)/d\Omega$ = scattering cross-section $\approx 6.6 \times 10^{-17}$ m^2/sr.

The combination of Equations (4-4) and (4-19) produces an expression for the average power required for CW phase compensation;

$$P_\ell \approx \frac{3.39\left[\sec(\zeta) H_s\right]^2 hc\, k_c^{-1/5} k_p^{6/5} N_{rms}}{\gamma_\ell \gamma_p \eta \tau_0 r_0^2 C_s \left[d\sigma(\pi)/d\Omega\right]\left[\left(\sigma^2_{figure}\right)_{system}\right]^{17/10}} \left\{1+1.52\left(\frac{k_c}{k_p}\right)^{12/5}\left[\left(\sigma^2_{figure}\right)_{system}\right]^{-6/5}\right\}^{1/2} . \quad (4\text{-}20)$$

A plot of the average laser power and pulse repetition rate as a function of the allowable figure variance is given in Figure 23. A total two-way throughput of 4 percent was assumed in the development of these laser requirements.

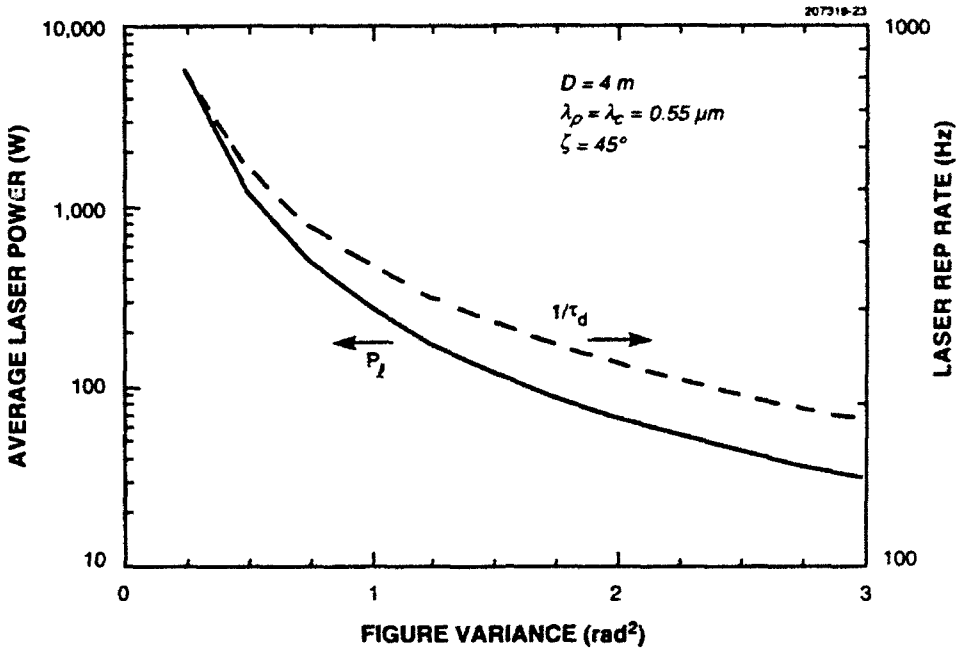

Figure 23. Beacon-laser specifications for resonance backscatter from the earth's sodium layer. A two-way throughput of 4 percent has been assumed in this calculation.

The development of sodium-frequency lasers has been active at Lincoln Laboratory for several years. The most recent efforts have focused on a solid-state design based on the sum-frequency mixing of two diode-pumped Nd:YAG lasers operating at 1.064 μm and 1.319 μm [36]. A 24-mJ 840-Hz laser was constructed in 1990, and it is predicted that this same technology could be used to build a device capable of generating several hundred watts of average power.

4.5 PERFORMANCE COMPARISONS FOR NATURAL-STAR AND LASER GUIDE-STAR SYSTEMS

All of the relationships crucial to the design of natural-star and synthetic-beacon adaptive-optics systems have now been assembled. A comparative evaluation of these two compensation approaches is most easily accomplished through a calculation of the achievable long-exposure Strehls. Recall that the Strehl for uncompensated turbulence is

$$[\text{Strehl}]_{\text{LE}} \approx \frac{1}{1+\left[D/r_o\right]^2} \quad . \tag{4-21}$$

A modest improvement to this number can be realized by incorporating a tracking system to remove the tilt component of turbulence, thus achieving an on-axis irradiance similar to the short-exposure Strehl. From Yura [14],

$$\rho_0^{SE} \approx r_0\left[1+0.37\left(r_0/D\right)^{1/3}\right] \quad ; \tag{4-22}$$

thus, for the aperture diameter and wavelengths of interest this relationship predicts a Strehl improvement of approximately 50 percent. To obtain more substantial gains, the high spatial frequency components must also be corrected. As discussed in Section 2.4, the long-exposure beam profile that results from partial phase compensation is predicted to have a residual background of width λ/r_0 and a diffraction-limited central core that is smeared as a result of tilt jitter. If the ratio between the uncorrected background and the central core is large, the Strehl ratio can be approximated by the following expression:

$$[\text{Strehl}]_{LE} \approx \frac{\exp\left\{-\left[\left(\sigma^2_{\text{figure}}\right)_{\text{system}} + \left(\sigma^2_{\text{figure}}\right)_{\text{focus anisoplanatism}} + \left(\sigma^2_{\text{figure}}\right)_{\text{beacon offset}}\right]\right\}}{1+4.94\left(\frac{D}{\lambda_c}\right)^2\left[\left(\sigma^2_{\text{tilt}}\right)_{\text{system}} + \left(\sigma^2_{\text{tilt}}\right)_{\text{beacon offset}}\right]} . \tag{4-23}$$

For natural beacons, the focus-anisoplanatism term in the numerator will be zero; in addition, tracking errors in the denominator can be ignored, as the constraints imposed by the wavefront sensor require a very bright reference having a small angular displacement. The beacon-offset term in the numerator will be zero for synthetic-beacon systems.

The strategy at this point will be to develop a balanced error budget based on Equation (4-23). In keeping with the relatively modest goals that are currently being discussed within the astronomy community, a set of design criteria will be used that results in a factor-of-10 ratio between the central core of the beam profile and the background and which limits the width of the central core to twice the diffraction limit. The corrected and uncorrected point-spread functions are compared in Figure 24 for imaging at 0.55 μm.

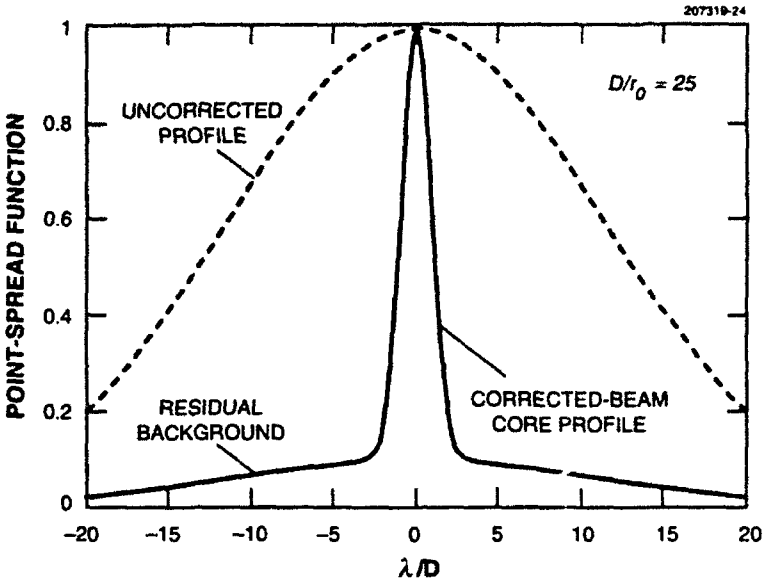

Figure 24. Comparison of the corrected and uncorrected beam profiles for a design criteria that restricts the tilt jitter to twice the diffraction-limited beam diameter and achieves a signal-to-background ratio of 10. This plot represents the point-spread function comparison for operation at 0.55 μm.

The final results of the analysis of a 4-m compensated-imaging system are summarized in Table 3. A total of six configurations are included, and the error budget for each can be found in the uppermost section of this chart. The corresponding component specifications are given in the next four rows, which show the required number of actuators, servo bandwidth, average laser power, and beacon brightness. It is not surprising that in each case the actuator spacing is closely matched to turbulence coherence length and that the servo bandwidth (defined as $1/10\tau_d$) is approximately equal to the Greenwood frequency. With the exception of the requirement on the laser output, all of the numbers listed are well within the current state of the art.

The bottom section of Table 3 contains a quantitative comparison of the long-exposure Strehl and resolution, as defined by Equations (2-49) and (2-50). In each case a substantial improvement in the effective seeing and image intensity is achieved. The motivation for pursuing synthetic-beacon constructs is clearly indicated in the comparison of operational utility listed in the last row of this summary. As a result of a lower irradiance requirement for full-aperture tracking (corresponding to 6 visual magnitudes) and a larger isoplanatic angle (by a factor of 3.5), the probability of finding a reference star for tilt stabilization in the visible is over 3 orders of magnitude greater than the likelihood of finding a beacon source for phase compensation. Although the absolute utility at 0.55 μm is only a fraction of a percent, because this number scales roughly as $\tau_0 r_0^2 \theta_0^2$, a slightly more benign turbulence model would result in a greatly improved estimate.

In closing, the system designer need not be constrained to precisely tailor the adaptive-optics equipment to the expected turbulence conditions or the correction wavelength. Through the use of interchangeable reconstruction operators and adjustable timing circuitry, it is always possible to modify both the effective actuator density and servo bandwidth to achieve maximum effectiveness. Thus, the short-wavelength capability of the system can steadily evolve as component technology improves without suffering a loss of performance in the infrared.

TABLE 3

Summary of Compensation-System Design Specifications and Operational Utility for a Factor-of-5 Improvement in the Long-Exposure Strehl for a 4-m Telescope

	Natural-Star System			Laser Guide-Star System		
	V Band 0.55 μm	J Band 1.25 μm	K Band 2.2 μm	V Band 0.55 μm	J Band 1.25 μm	K Band 2.2 μm
σ^2_{figure} (rad^2 of phase)	4.2	2.4	1.3	2.9	1.2	0.49
σ^2_{tilt} (rad^2 of tilt)	0	0	0	1.2×10^{-14}	5.9×10^{-14}	1.8×10^{-13}
Number of Actuators	290	85	45	250	90	65
Servo Bandwidth, $1/10\tau_d$ (Hz)	23	12	9	21	12	11
Sodium-Beacon Laser Power (W)	—	—	—	47	9	6
Beacon/Fiducial-Star Magnitude	8	10	11	13	16	18
Uncorrected Strehl	0.0016	0.012	0.044	0.0016	0.012	0.044
Corrected Strehl	0.016	0.11	0.32	0.015	0.082	0.17
Uncorrected Resolution ($\times1.22\lambda/D$)	25	9.2	4.8	25	9.2	4.8
Corrected Resolution ($\times1.22\lambda/D$)	2.6	1.3	1.0	3.1	2.0	2.0
Fractional Sky Coverage	3×10^{-6}	7×10^{-5}	3×10^{-4}	0.003	0.2	1

5. CONCLUSIONS

The analytical relationships developed in this optimization study are generally consistent with empirical design rules that have evolved over nearly three decades of research in the field of high-energy laser-beam control. For imaging applications, the requirements for phase correction can be relaxed somewhat, but to achieve a significant improvement in the short-exposure beam profile, the actuator spacing and correction bandwidth of an adaptive-optics system must be closely matched to the corresponding turbulence parameters.

At this point there is little doubt as to the applicability of adaptive optics to the field of astronomy. Experiments conducted by researchers at Lincoln Laboratory and other facilities have conclusively demonstrated the efficacy of both the wavefront-compensation technology and the laser guide-star concept. Much still needs to be done, however, before adaptive-optics technology is widely accepted as a tool for astronomical research. Effectively adapting this technology to astronomical telescopes will require an emphasis on reducing overall system complexity and cost while maintaining component reliability. The first step in this process is to establish acceptable criteria for performance, upon which a suitable balance between capability and design sophistication can be achieved. This issue has been the principal motivation in the analysis just presented.

APPENDIX A—AN ANALYTICAL TREATMENT OF TURBULENCE EFFECTS

Quantitative estimates of turbulence effects have traditionally been difficult to obtain because their analytic treatment involves complex integrals and fractional powers of the integration variable. As a result, most investigators have resorted to numerical integration techniques or Monte Carlo methods that use a large ensemble of individual turbulence realizations. Although these approaches give accurate results, parametric investigations are difficult and the underlying physics is often lost.

The general philosophy of the Lincoln approach is that far-field characteristics (such as Strehl and resolution) can be derived from residual phase error as measured in the pupil plane of the telescope. If an adaptive-optics system is used, residual phase error refers to the difference between the actual phase and the phase correction applied by the deformable mirror. These differences can arise from insufficient temporal or spatial resolution in the compensation system or differences between the beampath of the turbulence beacon and the object under investigation. All these effects can be studied using the approach described in this report.

A.1 STATISTICAL DESCRIPTION OF THE PUPIL-PLANE ELECTRIC FIELD

For imaging applications, the ultimate interest lies in the point-spread function of the collection system in the focal plane, but for turbulence calculations this quantity is most easily inferred from the residual phase error in the plane of the receiver aperture. Although amplitude fluctuations play a role in the distortion process, to a good approximation the far-field error can be accounted for by the average phase variance, σ_ϕ^2, of the electric field in the pupil plane of the telescope.

A.1.1 The Rytov Approximation

The general form of the wave equation for propagation through turbulence cannot be solved in closed form, but through the judicious application of approximations an approximate form can be developed that is amenable to solution. The usual starting point is a form introduced by Tatarski [37] that expresses the electric field as a function of the three-dimensional position vector, $\vec{r}$, and time, t, in the presence of turbulence:

$$E(\vec{r},t) = \underbrace{\overline{E}^{1/2} \exp\left[i\vec{k}_0 \cdot \vec{r} - i\omega t\right]}_{E_0} \underbrace{\exp\left[\chi(\vec{r},t) + i\phi(\vec{r},t)\right]}_{E_1}, \tag{A-1}$$

where
- E_0 = unperturbed radiation,
- E_1 = perturbation component,
- $\overline{E}^{1/2}$ = average irradiance,
- ω = temporal frequency of the electromagnetic field,
- $\vec{k}_0$ = wave vector of magnitude $2\pi/\lambda$, and
- λ = wavelength of light.

The real parameters $\chi(\vec{r},t)$ and $\phi(\vec{r},t)$ define the log-amplitude and phase components of a multiplicative perturbation that is introduced when light is diffracted as a result of changes in the index of refraction along the propagation path. This form, known as the Rytov approximation, is valid as long as the perturbation is small. From Equation (A-1) it follows that

$$\chi + i\phi = \ln\left(1 + \frac{E_1}{E_0}\right) \approx \frac{E_1}{E_0} \quad . \tag{A-2}$$

It will be assumed that χ and ϕ are statistically independent random variables having Gaussian probability distributions and zero mean.

A detailed derivation of the perturbation equation can be found in several excellent texts [38]; therefore, only a brief outline of the standard treatment of this problem will be given. As indicated in Figure A-1, light passing through a turbulent medium is assumed to diffract from a set of phase sheets aligned in planes perpendicular to the propagation axis. If the z axis is taken as the propagation direction and the effect in the plane of the origin of the coordinate system at time $t = 0$ is measured, the perturbation component of the electric field can be obtained directly from the equation for Fresnel diffraction:

$$E_1(x,y,0) = \frac{k_0^2}{2\pi}\int_{-\infty}^{\infty} dx' \int_{-\infty}^{\infty} dy' \int_{0}^{\infty} dz' \frac{1}{z'} \exp\left\{-ik_0\left[z' + \frac{\left[(x-x')^2 + (y-y')^2\right]}{2z'}\right]\right\} n_1(x',y',z') E_0(x',y',z') \, . \tag{A-3}$$

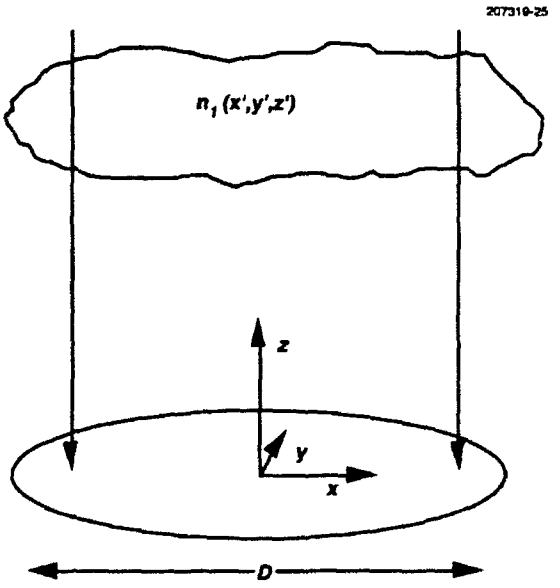

Figure A-1. Propagation of light through a single phase screen at range z′ to an aperture of diameter D centered at the origin of the coordinate system.

The function $n_1(x',y',z')$ represents the perturbation component of the refractive index, and the volume integration is performed over the entire space between the origin and the source. By combining this expression with Equations (A-1) and (A-2), the following pair of equations is obtained:

$$\chi(x,y,0)=\frac{k_0^2}{2\pi}\int_0^{\infty}dz'\int_{-\infty}^{\infty}dx'\int_{-\infty}^{\infty}dy'\frac{1}{z'}\cos\left\{\frac{k_0\left[(x-x')^2+(y-y')^2\right]}{2z'}\right\}n_1(x',y',z'), \tag{A-4}$$

and

$$\phi(x,y,0)=\frac{k_0^2}{2\pi}\int_0^{\infty}dz'\int_{-\infty}^{\infty}dx'\int_{-\infty}^{\infty}dy'\frac{1}{z'}\sin\left\{\frac{k_0\left[(x-x')^2+(y-y')^2\right]}{2z'}\right\}n_1(x',y',z') \ . \tag{A-5}$$

The integrals over x' and y' are recognized as the convolution of a filter function with the random variable n_1. For a linear transformation of this form, the power spectral density of the output variable is equal to the product of the squared modulus of the transfer function of the filter and the spectral density function of the input variable. The transfer functions of the filter expressions are obtained from their Fourier transforms

$$\left|\mathcal{F}\left\{\frac{k_0^2}{2\pi z'}\cos\left[\frac{k_0\left(x^2+y^2\right)}{2z'}\right]\right\}\right|^2=k_0^2\sin^2\left[\frac{\left(\kappa_x^2+\kappa_y^2\right)}{2k_0}z'\right] \tag{A-6}$$

and

$$\left|\mathcal{F}\left\{\frac{k_0^2}{2\pi z'}\sin\left[\frac{k_0\left(x^2+y^2\right)}{2z'}\right]\right\}\right|^2=k_0^2\cos^2\left[\frac{\left(\kappa_x^2+\kappa_y^2\right)}{2k_0}z'\right], \tag{A-7}$$

where $\kappa_x \equiv 2\pi/x$ and $\kappa_y \equiv 2\pi/y$ are the spatial wavenumbers. From this result the power spectral density functions of χ and ϕ are seen to be

$$\Phi_\chi(\kappa_x,\kappa_y) = k_0^2 \int_0^\infty dz' \sin^2\left(\frac{\kappa_x^2+\kappa_y^2}{2k_0}z'\right)\Phi_n(\kappa_x,\kappa_y;z') \tag{A-8}$$

and

$$\Phi_\phi(\kappa_x,\kappa_y) = k_0^2 \int_0^\infty dz' \cos^2\left(\frac{\kappa_x^2+\kappa_y^2}{2k_0}z'\right)\Phi_n(\kappa_x,\kappa_y;z') \ . \tag{A-9}$$

Notice that the spectral density function, $\Phi_n(\kappa_x,\kappa_y;z')$, that appears in the last two equations is only defined within the κ_x,κ_y plane in κ space. The z parameter is explicitly included in the variable list because the strength of the refractive index fluctuations are typically dependent on position along the propagation path.

A.1.2 Three-Dimensional Spectral Density Function Normalization

At this point in the derivation it becomes necessary to develop a relationship between the two-dimensional spectral density function and its three-dimensional form, $\Phi_n(\kappa_x,\kappa_y,\kappa_z;z')$, in which the refractive-index spectral density is typically presented. In this representation it is assumed that turbulence is constant locally, and its average properties change slowly in the propagation direction. This is accomplished by taking a careful look at the manner in which the z integral is performed and the effect of correlation along the z axis.

When z-axis correlation effects are included in Equations (A-4) and (A-5), the power spectral density of an output variable, α, is properly written as the convolution of the filter function, $F_\alpha(\kappa_x,\kappa_y;z')F_\alpha^*(\kappa_x,\kappa_y;z'')$, with the cross-spectral density function, $\tilde{\Phi}_n(\kappa_x,\kappa_y;z',z'')$, of the refractive index

$$\Phi_\alpha(\kappa_x,\kappa_y) = \int_0^\infty dz' \int_0^\infty dz'' F_\alpha(\kappa_x,\kappa_y;z')F_\alpha^*(\kappa_x,\kappa_y;z'')\tilde{\Phi}_n(\kappa_x,\kappa_y;z',z'') \ . \tag{A-10}$$

By making the variable substitutions $z = (z'+z'')/2$ and $\Delta z = z' - z''$, this expression can be rewritten

$$\begin{aligned}\Phi_\alpha(\kappa_x,\kappa_y) &= \int_0^\infty dz \int_{-z}^{z} d\Delta z\, F_\alpha(\kappa_x,\kappa_y;z+\Delta z/2)F_\alpha^*(\kappa_x,\kappa_y;z-\Delta z/2)\tilde{\Phi}_n(\kappa_x,\kappa_y;\Delta z,z) \\ &\approx \int_0^\infty dz \left|F_\alpha(\kappa_x,\kappa_y;z)\right|^2 \int_{-\infty}^{\infty} d\Delta z\, \tilde{\Phi}_n(\kappa_x,\kappa_y;\Delta z,z)\end{aligned} \ , \tag{A-11}$$

where the interchange of the order of integration and the modification of integration limits is possible because the correlation length of $\tilde{\Phi}_n$ is short with respect to functional changes with respect to z. This equation is similar in form to Equations (A-8) and (A-9), and the cross-spectral density integral, $\int_{-\infty}^{\infty} d\Delta z\, \tilde{\Phi}_n(\kappa_x, \kappa_y; \Delta z, z)$, is seen to be equivalent to the two-dimensional spectral density function. The desired result is obtained by noting that Φ_n and $\tilde{\Phi}_n$ are Fourier-transform pairs with respect to Δz, so that

$$\mathcal{F}\left[\tilde{\Phi}_n(\kappa_x, \kappa_y; \Delta z, z)\right] = \frac{1}{2\pi} \int_{-\infty}^{\infty} d\Delta z\, \tilde{\Phi}_n(\kappa_x, \kappa_y; \Delta z, z) \cos(\Delta z\, \kappa_z) = \Phi_n(\kappa_x, \kappa_y, \kappa_z; z) \tag{A-12}$$

and

$$\Phi_n(\kappa_x, \kappa_y; z) = \int_{-\infty}^{\infty} d\Delta z\, \tilde{\Phi}_n(\kappa_x, \kappa_y; \Delta z, z) = 2\pi\, \Phi_n(\kappa_x, \kappa_y, 0; z) \ . \tag{A-13}$$

From Equation (A-13) it can be seen that the expressions for log-amplitude and phase can be rewritten in a form that is compatible with a three-dimensional refractive-index spectrum by inserting the multiplicative constant 2π

$$\Phi_\chi(\kappa_x, \kappa_y) = 2\pi k_0^2 \int_0^{\infty} dz \sin^2\left(\frac{\kappa_x^2 + \kappa_y^2}{2k_0} z\right) \Phi_n(\kappa_x, \kappa_y, 0; z) \tag{A-14}$$

and

$$\Phi_\phi(\kappa_x, \kappa_y) = 2\pi k_0^2 \int_0^{\infty} dz \cos^2\left(\frac{\kappa_x^2 + \kappa_y^2}{2k_0} z\right) \Phi_n(\kappa_x, \kappa_y, 0; z) \ . \tag{A-15}$$

A.1.3 The Kolmogorov Turbulence Spectrum

The power spectral density function of the index of refraction can be derived from well-established physical laws relating to the turbulent flow of air. For spatial frequencies within a region known as the inertial subrange, Kolmogorov [7] showed that the structure function is proportional to the 2/3 power of the scalar distance. From Kolmogorov's observation, it follows that

$$\Phi_n(\bar{\kappa}, z) = 0.033 C_n^2(z) \kappa^{-11/3} \ , \tag{A-16}$$

where $\kappa^2 = \kappa_x^2 + \kappa_y^2 + \kappa_z^2$, and $C_n^2(z)$ is the strength of the turbulence fluctuations along the propagation path. As shown in Figure A-2, at large spatial frequencies the spectrum decays more rapidly than predicted by Equation (A-16) due to the dissipation of small eddies by viscous forces. Furthermore, at small spatial frequencies the function does not become infinite but approaches a constant value. A more precise representation is given by the von Kármán spectrum

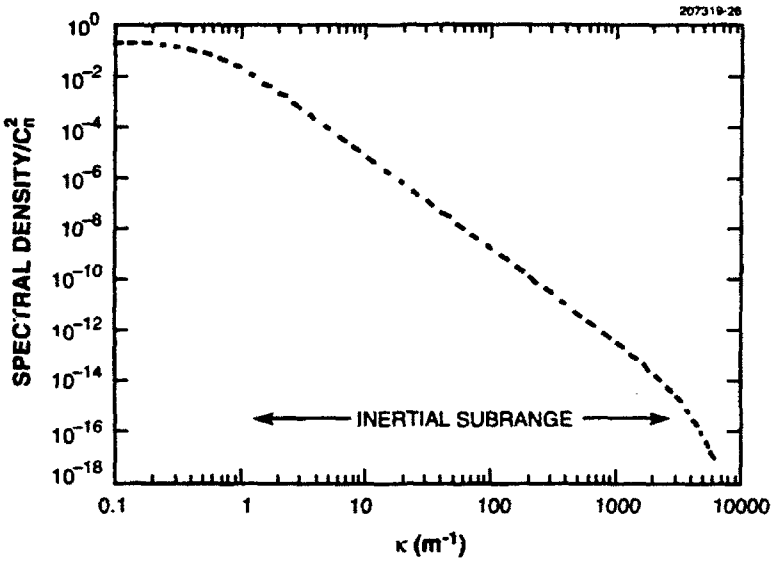

Figure A-2. The von Kármán turbulence spectrum. The Kolmogorov spectrum is valid within the inertial subrange.

$$\Phi_n(\vec{\kappa},z) \approx \frac{0.033 C_n^2(z)}{\left(\kappa^2+\kappa_o^2\right)^{11/6}} \exp\left(\frac{-\kappa^2}{\kappa_i^2}\right) , \tag{A-17}$$

where $L_o = 2\pi/\kappa_o$ represents the outer scale of the inertial subrange and κ_i is related to the inner scale. This particular form for the inner scale effect was suggested by Tatarski; other models, such as the Hill spectrum [39,40], can also be used. For most ground-to-space applications, however, sufficient accuracy is achieved with the simpler Kolmogorov spectrum.

A.1.4 Log-Amplitude Variance and Phase Variance of Uncorrected Turbulence

By combining Equations (A-14), (A-15), and (A-16), expressions for the net variance of the pupil-plane phase and log amplitude fluctuations due to turbulence are obtained;

$$\sigma_\chi^2 = 0.207 k_0^2 \int_0^\infty dz \int_{-\infty}^{\infty} d\kappa_x \int_{-\infty}^{\infty} d\kappa_y \, C_n^2(z) \kappa^{-11/3} \sin^2\left(\frac{\kappa^2 z}{2k_0}\right) \tag{A-18}$$

$$\sigma_\phi^2 = 0.207 k_0^2 \int_0^\infty dz \int_{-\infty}^{\infty} d\kappa_x \int_{-\infty}^{\infty} d\kappa_y \, C_n^2(z) \kappa^{-11/3} \cos^2\left(\frac{\kappa^2 z}{2k_0}\right) , \tag{A-19}$$

where $\kappa^2 = \kappa_x^2 + \kappa_y^2$. (In all subsequent calculations the κ-space integration will be confined to the κ_x, κ_y plane.) These two equations represent the standard representation of the total variance due to uncorrected turbulence. The following section will show how this formalism can be extended to address a much broader range of turbulence problems.

A.2 A GENERALIZED APPROACH TO TURBULENCE CALCULATIONS

The essential contribution of this work derives from two important observations. The first discovery is that a wide variety of turbulence-related problems can be treated analytically by inserting an appropriate multiplicative filter function, $F(\bar{\kappa};z)$, into Equations (A-18) and (A-19). When a single beam is involved, the general expression for phase variance has the form

$$\sigma_\phi^2 = 0.207 k_0^2 \int_0^\infty dz\, C_n^2(z) \int d\bar{\kappa}\, \kappa^{-11/3} F(\bar{\kappa};z) \quad , \tag{A-20}$$

where the approximation $\cos^2(x) \approx 1$ can be made for most problems in which the wave propagates from space to ground without introducing significant error.

The integrand of the triple integral indicated in the previous expression will usually have a very complicated structure that includes fractional powers of κ and Bessel functions of κ and z. Our second observation is that the κ integration can be treated as a Mellin transform, tables of which can be found in standard mathematical handbooks [41]. The Mellin transform of $g(x)$ is defined as

$$G(s) \equiv \mathcal{M}[g(x)] \equiv \int_0^\infty dx\, x^{s-1} g(x) \quad . \tag{A-21}$$

Thus an integral over κ that contains the term κ^p is equal to the Mellin transform of the remaining integrand evaluated for $s = p+1$;

$$\int_0^\infty d\kappa\, \kappa^p g(\kappa) \equiv G(s)\big|_{s=p+1} \quad . \tag{A-22}$$

The application of these computational techniques is best illustrated by a few simple examples. For simplicity, only the phase component of the electric field will be explicitly treated in the next section. However, the extension of these methods to calculations involving the log-amplitude component is straightforward.

A.2.1 Zernike Components of the Phase Variance

The Zernike modes of a circular aperture are incorporated in virtually all calculations of turbulence distortion. The expression for the variance of the i^{th} Zernike component of the phase function over an aperture of diameter D is

$$\left\{\sigma_\phi\right\}_i = \left| \int_0^{2\pi} d\theta \int_0^{D/2} d\rho \rho Z_i(\rho,\theta)\phi(\rho,\theta) \right|^2 , \tag{A-23}$$

where $Z_i(\rho,\theta)$ is the i^{th} Zernike polynomial. Because the statistical properties of the phase are defined by its power spectral density function, this integral is more easily evaluated in the Fourier domain. Fourier transforms of the Zernike polynomials evaluated for an aperture radius of unity are found in Noll [42]:

$$Q_i(k,\varphi) = \frac{1}{\pi} \int_0^{2\pi} d\theta \int_0^1 d\rho \rho Z_i(\rho,\theta) \exp\left(-2\pi i \vec{k}\cdot\vec{\rho}\right) . \tag{A-24}$$

These functions can be adapted to the notation used in this report by making the transformation $k = \kappa D/4\pi$, so that

$$\left\{\sigma_\phi^2\right\}_i = 0.207 k_0^2 \int_0^\infty dz C_n^2(z) \int_0^{2\pi} d\varphi \int_0^\infty d\kappa \kappa^{-8/3} \left| Q_i(\kappa D/4\pi,\varphi)\right|^2 . \tag{A-25}$$

As these components are orthogonal, the phase variances associated with different Zernike modes will add incoherently.

Piston-Removed Phase Error for Uncorrected Turbulence. The Kolmogorov spectrum is not only infinite at the origin, its total phase variance is also infinite. This result is non-physical and can be remedied by applying a finite outer scale; however, the more appropriate approach is to recognize that an average phase shift over the collection aperture will produce no net distortion in the far field and should therefore be ignored. The aperture-average phase is referred to as "piston" by the adaptive-optics community, and its value is derived from the product of the first Zernike polynomial and the pupil-plane phase. The filter function for piston removal over an aperture of diameter D is found to be

$$F(\vec{\kappa}) = 1 - \left| Q_1(\kappa D/4\pi)\right|^2 = 1 - \left[\frac{2J_1(\kappa D/2)}{\kappa D/2}\right]^2 . \tag{A-26}$$

The κ integration specified by Equation (A-20) is performed in the following manner:

$$\begin{aligned}
\int_{\vec{\kappa}} d\vec{\kappa} \kappa^{-11/3} \left\{1 - \left[\frac{2J_1(\kappa D/2)}{\kappa D/2}\right]^2\right\} &= 2\pi \int_0^\infty d\kappa \kappa^{-8/3} \left\{1 - \left[\frac{2J_1(\kappa D/2)}{\kappa D/2}\right]^2\right\} \\
&= \frac{32\pi}{D^2} \int_0^\infty d\kappa \kappa^{-14/3} \left\{\frac{(\kappa D/2)^2}{4} - J_1^2(\kappa D/2)\right\} \\
&= \frac{32\pi}{D^2} \mathcal{M}\left[\frac{(\kappa D/2)^2}{4} - J_1^2(\kappa D/2)\right]\Bigg|_{s=-11/3} .
\end{aligned} \tag{A-27}$$

The last expression is similar in form to a Mellin transform given in Appendix B:

$$\mathcal{M}\left[J_1^2(x)-\frac{x^2}{4}\right]=\frac{1}{2\sqrt{\pi}}\frac{\Gamma[1+s/2]\,\Gamma[1/2-s/2]}{\Gamma[2-s/2]\,\Gamma[1-s/2]} \quad . \tag{A-28}$$

By applying the transform identities

$$\mathcal{M}[-g(x)]\equiv-\mathcal{M}[g(x)] \text{ and } \mathcal{M}[g(ax)]\equiv a^{-s}\,\mathcal{M}[g(x)] \quad , \tag{A-29}$$

the following relationship is obtained:

$$\frac{32\pi}{D^2}\mathcal{M}\left[\frac{(\kappa D/2)^2}{4}-J_1^2(\kappa D/2)\right]\Bigg|_{s=-11/3}=-\frac{32\pi}{D^2}\left(\frac{D}{2}\right)^{11/3}\frac{1}{2\sqrt{\pi}}\frac{\Gamma[-5/6]\,\Gamma[14/6]}{\Gamma[32/6]\,\Gamma[17/6]}$$

$$=2.11\,D^{5/3} \quad . \tag{A-30}$$

Combining this expression with Equation (A-20) yields

$$\sigma_\phi^2=0.437k_0^2\,D^{5/3}\int_0^\infty dz\,C_n^2(z) \quad . \tag{A-31}$$

The final integration over z cannot be completed without specifying the turbulence profile; however, this calculation is easily performed for the standard turbulence models. It is common to characterize a turbulence model by its moments $\mu_n\equiv\int dh\,h^n\,C_n^2(h)$, which are computed at zenith. For an arbitrary zenith angle, ζ,

$$\int_0^\infty dz\,z^n\,C_n^2(z)\equiv\sec^{n+1}(\zeta)\int_0^\infty dh\,h^n\,C_n^2(h)\equiv\sec^{n+1}(\zeta)\mu_n \quad . \tag{A-32}$$

With the application of this identity,

$$\sigma_\phi^2=0.437k_0^2\,D^{5/3}\sec(\zeta)\mu_0 \quad , \tag{A-33}$$

which is the standard result. Although this particular expression can be easily obtained without the use of Mellin transforms, the benefit of this approach becomes obvious when more complicated filter functions are involved.

Figure and Tilt Calculations for Uncorrected Turbulence. Most adaptive-optics systems incorporate separate devices for tracking and high-spatial-frequency compensation; a typical configuration is shown in Figure A-3. For this reason it is convenient to develop individual expressions for each of these

turbulence components. The filter function for tilt is derived from the Fourier transforms of the second and third Zernike polynomials;

$$F_{\text{tilt}}(\vec{\kappa}) = \left|\mathcal{Q}_2(\kappa D/4\pi)\right|^2 + \left|Q_3(\kappa D/4\pi)\right|^2$$
$$= \left[\left(\frac{4J_2(\kappa D/2)}{\kappa D/2}\cos(\theta)\right)^2 + \left(\frac{4J_2(\kappa D/2)}{\kappa D/2}\sin(\theta)\right)^2\right] = \left[\frac{4J_2(\kappa D/2)}{\kappa D/2}\right]^2 , \quad \text{(A-34)}$$

and the associated Mellin transform is

$$\mathcal{M}\left[J_2^2(x)\right] = \frac{1}{2\sqrt{\pi}}\frac{\Gamma[2+s/2]\,\Gamma[1/2-s/2]}{\Gamma[3-s/2]\,\Gamma[1-s/2]} . \quad \text{(A-35)}$$

The tilt component of turbulence is usually given in units of rad^2 of single-axis tilt angle, and the conversion from rms phase to rms angle involves the multiplicative constant $8/(k_0 D)^2$. Combining this constant with Equation (A-35) and the variable change indicated in Equation (A-29) results in

$$\sigma_{\text{tilt}}^2 = 3.04\,D^{-1/3}\sec(\zeta)\mu_0 \quad (\text{rad}^2 \text{ of single-axis tilt}) . \quad \text{(A-36)}$$

The piston- and tilt-removed phase, also known as "figure," represents the high-spatial-frequency turbulence that must be corrected by the deformable mirror. The filter function for figure variance is the difference between Equations (A-26) and (A-34);

$$F_{\text{figure}}(\kappa) = 1 - \left[\frac{2J_1(\kappa D/2)}{\kappa D/2}\right]^2 - \left[\frac{4J_2(\kappa D/2)}{\kappa D/2}\right]^2 . \quad \text{(A-37)}$$

By applying the identity

$$\mathcal{M}\left[g_1(x) + g_2(x)\right] \equiv \mathcal{M}\left[g_1(x)\right] + \mathcal{M}\left[g_2(x)\right] , \quad \text{(A-38)}$$

the following result is obtained:

$$\mathcal{M}\left[\left(J_1^2(x) - \frac{x^2}{4}\right) + 4J_2^2(x)\right] = \frac{1}{2\sqrt{\pi}}\frac{\Gamma[1+s/2]\,\Gamma[1/2-s/2]}{\Gamma[2-s/2]\,\Gamma[1-s/2]} + \frac{2}{\sqrt{\pi}}\frac{\Gamma[2+s/2]\,\Gamma[1/2-s/2]}{\Gamma[3-s/2]\,\Gamma[1-s/2]} . \quad \text{(A-39)}$$

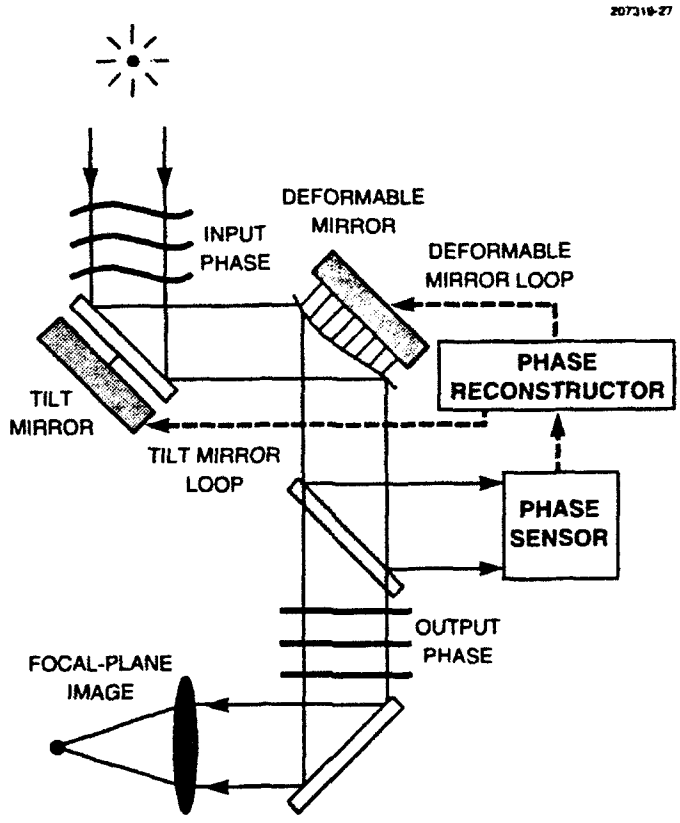

Figure A-3. Schematic presentation of a closed-loop adaptive-optics system. The first derivative of the phase difference between the incoming wavefront and the surface figure imposed by the tilt and deformable mirrors is measured by the phase sensor. The residual phase error is computed by the reconstructor and subsequently applied to the two active optical elements.

The final expression for figure variance is derived by following the steps outlined in the previous examples:

$$\sigma^2_{\text{figure}} = 0.207 k_0^2 \int_0^\infty dz\, C_n^2(z) \left(\frac{32\pi}{D^2}\right) \mathcal{M}\left[\left(J_1^2(\kappa D/2) - \frac{(\kappa D/2)^2}{4}\right) + 4J_2^2(\kappa D/2)\right]\Bigg|_{s=-11/3}$$

$$= 0.0567 k_0^2 D^{5/3} \sec(\zeta) \mu_0 \quad . \tag{A-40}$$

A.2.2 Phase Variance due to Anisoplanatic Effects

Most problems of interest for compensated-imaging applications involve a pair of beams, one which originates from the beacon that is viewed by the wavefront sensor and a second that passes through the correction system and is imaged onto the focal plane. Anisoplanatic effects occur whenever these two beams follow different paths through the atmosphere. Figure A-4 shows a simple geometry in which the rays impinging on a point in the pupil plane of the receiver pass through points in a single phase screen that differ by the vector displacement $\vec{d}$. If an adaptive-optics system is used to apply a correction based on the beacon information, the magnitude of the resulting error at point $\vec{\rho}$ will be proportional to

$$\left| n_1(\vec{\rho};z) - n_1\left(\vec{\rho} + \vec{d}(\vec{\rho};z);z\right)\right|^2 ,$$

where it is noted that $\vec{d}$ will be a function of both aperture position and the range to the phase screen. In κ space this displacement corresponds to a phase shift of $\vec{\kappa}\cdot\vec{d}$, so that the corresponding error expression would be

$$\left|1-\exp\left[i\left(\vec{\kappa}\cdot\vec{d}(\vec{\rho};z)\right)\right]\right|^2 \left|\mathcal{F}\left[n_1(\vec{\rho};z)\right]\right|^2 = 2\left[1-\cos\left(\vec{\kappa}\cdot\vec{d}(\vec{\rho};z)\right)\right]\Phi_n(\vec{\kappa};z) \quad . \qquad \text{(A-41)}$$

The term $2\left[1-\cos\left(\vec{\kappa}\cdot\vec{d}(\vec{\rho};z)\right)\right]$ can be viewed as a filter function associated with the displacement of the two rays. To obtain a function representative of the aperture-average error, the following integral must be performed:

$$F(\vec{\kappa};z) = \frac{4}{\pi D^2}\int_0^{2\pi} d\theta \int_0^{D/2} d\rho\,\rho\left[2-2\cos\left(\vec{\kappa}\cdot\vec{d}(\rho,\theta;z)\right)\right] . \qquad \text{(A-42)}$$

For some viewing geometries it may be possible to develop the filter function associated with a single component of an anisoplanatic effect by taking the product of Equation (A-42) and the appropriate Zernike-function filter. For the more general case illustrated in Figure A-5, however, the problem involves two beams that may have different diameters, intensity distributions, spatial offsets, and may originate from sources placed at different altitudes. The pupil-plane error variance results from the difference function

$$\begin{bmatrix}\sigma_\phi^2\\ \sigma_\chi^2\end{bmatrix} = 0.207k_0^2\int_0^\infty dz\int\frac{4}{\pi D^2}d\vec{\rho}\int d\vec{\kappa}\,\Phi_n(\vec{\kappa};z)$$
$$\times\left\{G_1(\gamma_1\vec{\kappa})\begin{bmatrix}\cos\left[P_1(\gamma_1,\kappa;z)\right]\\ \sin\left[P_1(\gamma_1,\kappa;z)\right]\end{bmatrix} - A(\vec{\kappa};\vec{\rho},z)G_2(\gamma_2\vec{\kappa})\begin{bmatrix}\cos\left[P_2(\gamma_2,\kappa;z)\right]\\ \sin\left[P_2(\gamma_2,\kappa;z)\right]\end{bmatrix}\right\}$$
$$\times\left\{G_1^*(\gamma_1\vec{\kappa})\begin{bmatrix}\cos\left[P_1(\gamma_1,\kappa;z)\right]\\ \sin\left[P_1(\gamma_1,\kappa;z)\right]\end{bmatrix} - A^*(\vec{\kappa};\vec{\rho},z)G_2^*(\gamma_2\vec{\kappa})\begin{bmatrix}\cos\left[P_2(\gamma_2,\kappa;z)\right]\\ \sin\left[P_2(\gamma_2,\kappa;z)\right]\end{bmatrix}\right\} , \qquad \text{(A-43)}$$

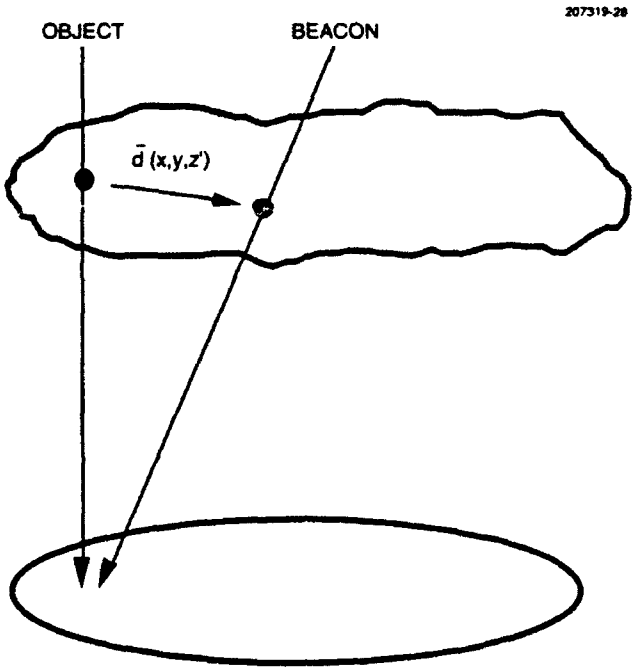

Figure A-4. Anisoplanatic error occurs when the beacon rays that impinge on a point in the collection aperture follow a different path than the rays from the object under observation. Within a phase screen at range z', the two rays pass through points that are separated by the vector displacement d.

which defines both the phase and log-amplitude error. For space-to-ground propagation, the following parametric definitions apply:

$$\begin{aligned}
\Phi_n(\vec{\kappa};z) &= \text{turbulence spectrum,} \\
A(\vec{\kappa};\vec{\rho},z) &= \text{amplitude ratio of the second beam relative to the first,} \\
P(\gamma, \kappa; z) &= \gamma\kappa^2 z/2k_0 = \text{propagation parameter,} \\
\gamma &= (L-z)/L \text{ for a source positioned at range } L, \text{ and} \\
G(\gamma\vec{\kappa}) &= \int d\vec{r}\,' g(\vec{r}\,')\exp[i\gamma\vec{\kappa}\cdot\vec{r}\,'] = \text{aperture filter function.}
\end{aligned}$$

It is important to recognize that the character of the the amplitude ratio will depend on the specification of the aperture filter function. When G_1 and G_2 are unity, $A(\vec{\kappa};\vec{\rho},z)$ describes the ratio between each pair of phase points at range z that lie along rays intersecting the collection aperture at point $\vec{\rho}$; in this case an integration over $\vec{\rho}$ is required to obtain the average variance. If filter functions representing an aperture-average Zernike component (such as piston or tilt) are used, however, the amplitude ratio is then computed only for the beam centroids, in which case $A(\vec{\kappa};z)$ will be a function of z but independent of $\vec{\rho}$.

With the introduction of Equation (A-43), two quantities can be computed that are of great interest to the astronomical community. The first relates to the issue of tracking stability, and the second defines the residual figure error that can be expected with the application of laser guide stars.

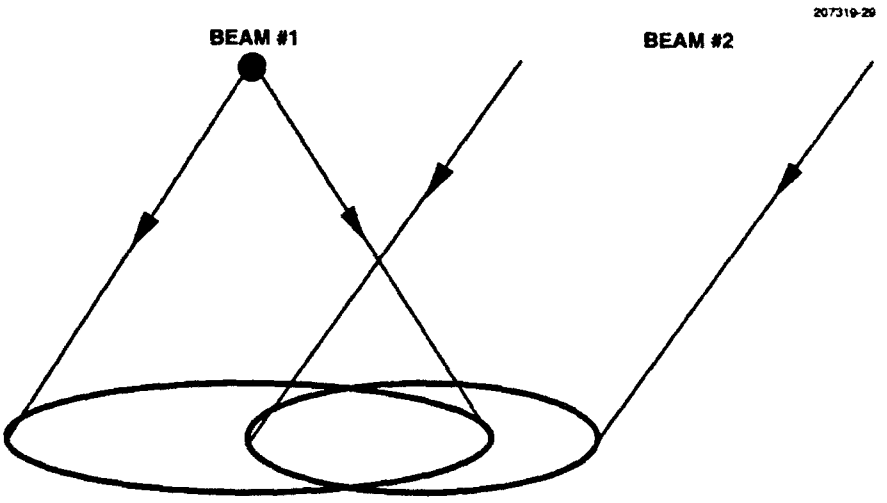

Figure A-5. Many turbulence calculations involve two separate beams. For adaptive-optics correction, one beam may represent the light from a beacon, whereas the second beam is the light received from a celestial object.

Tilt Component of Offset Anisoplanatism. For situations in which the object under observation is too dim to track directly, a bright neighboring star might be used as the reference beacon. However, this geometry will give rise to a differential tilt due to the angular displacement, ϑ, between the two objects.

As indicated in previous discussions, the aperture filter function for single-axis tilt is

$$G_{\text{tilt}}(\vec{\kappa}) = \left(\frac{8}{(k_0 D)^2}\right)\left[\frac{4J_2(\kappa D/2)}{\kappa D/2}\right]^2 . \tag{A-44}$$

The effect of an angular offset of ϑ is introduced into the variance expression through the amplitude function

$$A(\vec{\kappa};z) = \exp\left[i\vec{\kappa}\cdot\vec{\vartheta}\,z\right] , \tag{A-45}$$

which represents a phase shift due to a beam-centroid displacement that increases linearly with range. Combining the last two relationships with equation (A-43) produces the following expression for tilt variance for Kolmogorov turbulence:

$$\sigma_{\text{tilt}}^2 = 0.207 k_0^2 \int_0^\infty dz\, C_n^2(z) \int_0^{2\pi} d\varphi \int_0^\infty d\kappa\, \kappa^{-8/3} \left(\frac{8}{(k_0 D)^2} \right) \left[\frac{4 J_2(\kappa D/2)}{\kappa D/2} \right]^2 2\left[1 - \cos\left\{\kappa \vartheta z \cos(\varphi)\right\}\right]. \tag{A-46}$$

The integral over φ is accomplished through the application of the Bessel function identity

$$J_n(x) \equiv \frac{1}{2\pi} \int_0^{2\pi} d\varphi \cos\left[x \cos(\varphi) + n\varphi\right] , \tag{A-47}$$

which yields

$$\sigma_{\text{tilt}}^2 = 1.30 k_0^2 \int_0^\infty dz\, C_n^2(z) \int_0^\infty d\kappa\, \kappa^{-8/3} \left(\frac{8}{(k_0 D)^2} \right) \left[\frac{4 J_2(\kappa D/2)}{\kappa D/2} \right]^2 \left[2 - 2 J_0(\kappa \vartheta z)\right]. \tag{A-48}$$

Although the κ integration indicated in this equation can be performed directly using Mellin transforms that result in an expression containing generalized hypergeometric functions, for small displacement angles the correct result can be obtained by first expanding $\left[1 - J_0(\kappa \vartheta z)\right]$ in a Taylor's series. The integral for the first term of the expansion is then obtained using the Mellin transform for $J_2^2(x)$ given in Equation (A-35) for $s = -5/3$

$$\sigma_{\text{tilt}}^2 \approx 5.34 \sec^3(\zeta) D^{-7/3} \mu_2 \vartheta^2 \quad (\text{rad}^2 \text{ of single-axis tilt}) . \tag{A-49}$$

This approximation is reasonably accurate for $\vartheta < (D/4 \times 10^4 \text{ m})$. When normalized to the diffraction-limited beam diameter, the beam jitter is seen to be proportional to $\sec^{3/2}(\zeta) \lambda^{-1} D^{-1/6} \mu_2^{1/2} \vartheta$.

Figure Component of Focal Anisoplanatism. Laser guide stars are required to perform high-spatial-frequency compensation on objects that are too dim to provide phase information to the wavefront sensor of an adaptive-optics system. This compensation geometry results in an error known as focal anisoplanatism, and is one of the principal errors associated with guide-star imaging. As indicated in Figure A-6, the turbulence above the beacon is unsampled and therefore completely uncorrected. The residual figure error associated with this high-altitude component is taken from Equation (A-40):

$$\sigma_{\text{upper}}^2 = 0.0567 k_0^2 D^{5/3} \sec(\zeta) \mu_0^{\uparrow}(H) , \tag{A-50}$$

where the notation

$$\mu_n^{\uparrow}(H) \equiv \int_H^\infty dh\, h^n C_n^2(h) \tag{A-51}$$

has been introduced to represent the upper fractional moment computed from the beacon altitude, H, to the top of the atmosphere.

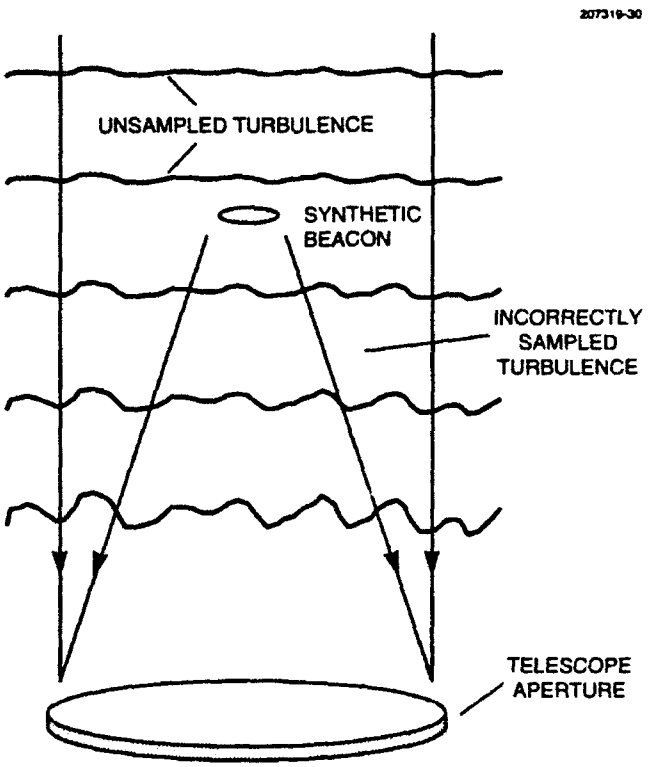

Figure A-6. The vertical rays represent light originating from a distant source that accumulate phase error in traveling through the atmosphere to the telescope. Radiation from the laser guide-star follows a slightly different path to the telescope and is therefore unable to sample turbulence distortions above the beacon altitude or to precisely sample the turbulence that lies below the beacon.

Below the beacon, the object and beacon rays that strike a point $\vec{\rho}$ in the collection aperture are displaced from one another by a distance

$$\vec{d}(\vec{\rho};z)=\frac{\vec{\rho}z}{L} \tag{A-52}$$

at a range z from the pupil plane. Therefore, from Equation (A-43), the total phase error due to the turbulence below the beacon is

$$\sigma_\phi^2 = 0.207 k_0^2 \int_0^L dz\, C_n^2(z) \int_0^{2\pi} d\varphi \int_0^\infty d\kappa\ \kappa^{-8/3} \frac{4}{\pi D^2} \int_0^{2\pi} d\theta \int_0^{D/2} d\rho\, \rho \left[2-2\cos\left(\frac{\kappa\rho z}{L}\cos(\theta)\right)\right]. \tag{A-53}$$

The integrals over θ and ρ can be performed by applying the Bessel function identities

$$J_n(x) \equiv \frac{1}{2\pi}\int_0^{2\pi} d\theta \cos[x\cos(\theta)+n\theta] \text{ and } \int dx\, x^{n+1} J_n(ax) \equiv \frac{x^{n+1}}{a} J_{n+1}(ax) \ , \quad \text{(A-54)}$$

with the result

$$\sigma_\phi^2 = 0.207 k_0^2 \int_0^L dz\, C_n^2(z) \int_0^{2\pi} d\varphi \int_0^\infty d\kappa\ \kappa^{-8/3}\left[2 - 4\frac{J_1(\kappa Dz/2L)}{\kappa Dz/2L}\right]. \quad \text{(A-55)}$$

The integration over κ is accomplished by applying the Mellin transform

$$\mathcal{M}\left[J_1(x) - \frac{x}{2}\right] = 2^{s-1}\frac{\Gamma[1/2+s/2]}{\Gamma[3/2-s/2]} \quad \text{(A-56)}$$

for $s = -8/3$. In the final expression, all the integrals have been performed analytically except for the fractional moment computed between the receiver and the beacon altitude

$$\sigma_\phi^2 = 0.5 D^{5/3} k_0^2 \sec(\zeta)\frac{\mu_{5/3}^{\downarrow}(H)}{H^{5/3}} \ . \quad \text{(A-57)}$$

Equation (A-57) represents the total error due to the turbulence below the beacon. To compute the figure component of this error, the piston and tilt terms must be removed. If the beacon is placed over the center of the receiving aperture, the amplitude ratio $A(\vec{\kappa};z)$ will be unity, but the values of γ for the object and beacon beams will be 1 and $1-z/L$, respectively. Thus, from the aperture filter functions given earlier in Equations (A-26) and (A-34),

$$\sigma_\phi^2 = 1.30 k_0^2 \int_0^L dz\, C_n^2(z) \int_0^\infty d\kappa\ \kappa^{-8/3} 4\nu^2\left[\frac{J_\nu(\kappa D/2)}{\kappa D/2} - \frac{J_\nu(\kappa D(1-z/L)/2)}{\kappa D(1-z/L)/2}\right]^2 \ , \quad \text{(A-58)}$$

where the value of ν is 1 for piston and 2 for tilt. A Taylor's series expansion of the second Bessel function and its denominator about the point $\kappa D/2$ yields an expression for which the leading term is quadratic in the expansion parameter z/L ;

$$\sigma_\phi^2 \approx 1.30 k_0^2 \int_0^L dz\, C_n^2(z) \int_0^\infty d\kappa\ \kappa^{-8/3} 4\nu^2\left(\frac{z}{L}\right)^2\left[\frac{-J_\nu(\kappa D/2)+(\kappa D/2)J_\nu'(\kappa D/2)}{\kappa D/2}\right]^2 \ . \quad \text{(A-59)}$$

This can be further simplified using the identity $nJ_n(x) - xJ_n'(x) \equiv xJ_{n+1}(x)$ to give

$$\sigma_\phi^2 \approx 1.30 k_0^2 \int_0^L dz\, C_n^2(z) \int_0^\infty d\kappa\ \kappa^{-8/3} 4\nu^2\left(\frac{z}{L}\right)^2\left[-J_{\nu+1}(\kappa D/2)+(\nu-1)\frac{J_\nu(\kappa D/2)}{\kappa D/2}\right]^2 \ . \quad \text{(A-60)}$$

The κ integration is performed using the Mellin transform identities found in Appendix B, from which the following two quantities are derived:

$$\sigma_\phi^2 \approx 0.0833\, D^{5/3}\, k_0^2 \sec(\zeta) \frac{\mu_2^{\downarrow}(H)}{H^2} \quad \text{for the piston component,} \tag{A-61}$$

and

$$\sigma_\phi^2 \approx 0.354\, D^{5/3}\, k_0^2 \sec(\zeta) \frac{\mu_2^{\downarrow}(H)}{H^2} \quad \text{for the tilt component.} \tag{A-62}$$

Combining these results with Equation (A-57) yields the figure variance due to turbulence that is improperly sampled below a laser guide star

$$\sigma_{\text{lower}}^2 \approx D^{5/3}\, k_0^2 \sec(\zeta) \left[0.500 \frac{\mu_{5/3}^{\downarrow}(H)}{H^{5/3}} - 0.437 \frac{\mu_2^{\downarrow}(H)}{H^2} \right] . \tag{A-63}$$

The net figure error that would result from a beacon placed at an altitude H over the center of the collection aperture is the sum of Equations (A-50) and (A-63);

$$\sigma_{\text{figure}}^2 \approx D^{5/3}\, k_0^2 \sec(\zeta) \left[0.0567 \mu_0^{\uparrow}(H) + 0.500 \frac{\mu_{5/3}^{\downarrow}(H)}{H^{5/3}} - 0.437 \frac{\mu_2^{\downarrow}(H)}{H^2} \right] . \tag{A-64}$$

APPENDIX B—RELATIONSHIPS APPLIED IN THE ANALYTICAL TREATMENT OF TURBULENCE

B.1 PROPERTIES OF THE MELLIN TRANSFORM

The Mellin transform $G(s)$ of the function $g(x)$ is defined as

$$G(s) \equiv \mathcal{M}[g(x)] \equiv \int_0^\infty dx\, x^{s-1} g(x) \ . \tag{B-1}$$

The structure of this relationship yields the following set of identities, which are frequently invoked in the application of Mellin transforms to turbulence problems:

$$\mathcal{M}[-g(x)] \equiv -\mathcal{M}[g(x)] \ , \tag{B-2}$$

$$\mathcal{M}[g(ax)] \equiv a^{-s}\, \mathcal{M}[g(x)] \ , \tag{B-3}$$

and

$$\mathcal{M}\left[\sum g_i(x)\right] \equiv \sum \mathcal{M}[g_i(x)] \ . \tag{B-4}$$

It can also be shown that the convolution of two functions can be derived from the product of their transforms;

$$\mathcal{M}\left[\int_0^\infty \frac{dy}{y} g_1(x) g_2(x/y)\right] \equiv \mathcal{M}[g_1(x)]\mathcal{M}[g_2(x)] \ . \tag{B-5}$$

The principal benefit of the Mellin transform for turbulence calculations derives from the ready availability of standard transform tables that encompass a wide range of interesting problems; see Table B-1. The solutions typically involve the ratio of the product of gamma functions, and as a result the following notation is adopted:

$$\Gamma\left[\begin{matrix}\alpha_1,\ldots,\alpha_m \\ \beta_1,\ldots,\beta_n\end{matrix}\right] \equiv \frac{\Gamma[\alpha_1]\cdots\Gamma[\alpha_m]}{\Gamma[\beta_1]\cdots\Gamma[\beta_n]} \ . \tag{B-6}$$

Because the only singularities of this ratio occur when the arguments of the gamma functions in the numerator are negative, pole-residue integration can be used to obtain a power-series expansion for all expressions of this form.

TABLE B-1

Partial List of Mellin Transforms

$g(x)$	$\mathcal{M}[g(x)] \equiv \int_0^\infty dx\, x^{s-1} g(x)$	
$\exp(-x)$	$\Gamma[s]$	$s > 0$
$\sin(x)$	$2^{s-1}\sqrt{\pi}\,\Gamma\begin{bmatrix}1/2+s/2\\1-s/2\end{bmatrix}$	$-1 < s < 1$
$\cos(x)$	$2^{s-1}\sqrt{\pi}\,\Gamma\begin{bmatrix}s/2\\1/2-s/2\end{bmatrix}$	$0 < s < 1$
$J_\nu(x)$	$2^{s-1}\Gamma\begin{bmatrix}s/2+\nu/2\\\nu/2+1-s/2\end{bmatrix}$	$-\nu < s < 3/2$
$J_\nu^2(x)$	$\frac{1}{2\sqrt{\pi}}\Gamma\begin{bmatrix}s/2+\nu, 1/2-s/2\\\nu+1-s/2, 1-s/2\end{bmatrix}$	$-2\nu < s < 1$
$J_\mu(x)J_\lambda(x)$	$\frac{1}{2\sqrt{\pi}}\Gamma\begin{bmatrix}s/2+\frac{\mu+\lambda}{2}, \frac{1}{2}-s/2, 1-s/2\\1-s/2+\frac{\mu+\lambda}{2}, 1-s/2+\frac{\mu-\lambda}{2}, 1-s/2+\frac{\lambda-\mu}{2}\end{bmatrix}$	$-\mu+\lambda < s < 1$
$J_\nu(x) - \frac{x^\nu}{2^\nu \nu!}$	$2^{s-1}\Gamma\begin{bmatrix}s/2+\nu/2\\\nu/2+1-s/2\end{bmatrix}$	$-\nu-2 < s < -\nu$
$J_\nu^2(x) - \frac{x^{2\nu}}{2^{2\nu}(\nu!)^2}$	$\frac{1}{2\sqrt{\pi}}\Gamma\begin{bmatrix}s/2+\nu, 1/2-s/2\\\nu+1-s/2, 1-s/2\end{bmatrix}$	$-2\nu-4 < s < -2\nu$
$J_\mu(x)J_\lambda(x) - \frac{x^{\mu+\lambda}}{2^{\mu+\lambda}\mu!\lambda!}$	$\frac{1}{2\sqrt{\pi}}\Gamma\begin{bmatrix}s/2+\frac{\mu+\lambda}{2}, \frac{1}{2}-s/2, 1-s/2\\1-s/2+\frac{\mu+\lambda}{2}, 1-s/2+\frac{\mu-\lambda}{2}, 1-s/2+\frac{\lambda-\mu}{2}\end{bmatrix}$	$-\mu-\lambda-4 < s < -\mu-\lambda$

B.2 APERTURE FILTER FUNCTIONS

The filter functions used to obtain the Zernike modes for a circular aperture are listed below. Also given are the filters for the second-moment quantities obtained with a finite receive aperture and a finite-size source.

B.2.1 Zernike Modes

The general formula for the filter function associated with a Zernike component on a circular aperture of diameter D derives from Noll [42];

$$\left.\begin{matrix} F_{m,n}(\vec{\kappa})_x \\ F_{m,n}(\vec{\kappa})_y \\ F_{0,n}(\vec{\kappa}) \end{matrix}\right\} = (n+1)\left[\frac{2J_{n+1}(\kappa D/2)}{\kappa D/2}\right]^2 \begin{cases} 2\cos^2(m\varphi) \\ 2\sin^2(m\varphi) \\ 1 \ (m=0) \end{cases} . \tag{B-7}$$

The piston phase-variance filter function is

$$F(\vec{\kappa}) = \left[\frac{2J_1(\kappa D/2)}{\kappa D/2}\right]^2 , \tag{B-8}$$

which must be multiplied by $(1/k_0)^2$ to obtain the mean-squared value. The function used to determine the x, y, and total phase variance associated with aperture tilt is

$$\left.\begin{matrix} F_x(\vec{\kappa}) \\ F_y(\vec{\kappa}) \\ F(\vec{\kappa}) \end{matrix}\right\} = \left[\frac{4J_2(\kappa D/2)}{\kappa D/2}\right]^2 \begin{cases} \cos^2(\varphi) \\ \sin^2(\varphi) \\ 1 \end{cases} , \tag{B-9}$$

from which the variance for the single-axis tilt angle can be obtained by multiplying by $8/(k_0 D)^2$.

In some problems the variance must be calculated with some of the Zernike modes removed. This is easily accomplished by subtracting the phase variance due to these components from the total variance. For instance, the filter function to remove piston and tilt variance from a single wave is

$$F(\vec{\kappa}) = 1 - \left[\frac{2J_1(\kappa D/2)}{\kappa D/2}\right]^2 - \left[\frac{4J_2(\kappa D/2)}{\kappa D/2}\right]^2 . \tag{B-10}$$

B.2.2 Gradient Tilt

The gradient, or G-tilt, is equal to the average phase gradient over the receiver aperture. The filter function for G-tilt variance over a circular aperture is

$$\left.\begin{matrix} F_x(\bar{\kappa}) \\ F_y(\bar{\kappa}) \\ F(\bar{\kappa}) \end{matrix}\right\} = J_1^2(\kappa D/2)\begin{Bmatrix} \cos^2(\varphi) \\ \sin^2(\varphi) \\ 1 \end{Bmatrix} . \tag{B-11}$$

The single-axis tilt-angle variance is obtained from the above by multiplying by $8/(k_0 D)$.

B.2.3 Filter Functions For Finite-Size Apertures And Distributed Sources

The coherent average of a quantity from a point source at a range L over a receive aperture is equal to the piston of the quantity, which is given by

$$F(\bar{\kappa}) = \left[2\frac{J_1(\kappa D(1-z/L)/2)}{\kappa D(1-z/L)/2}\right]^2 , \tag{B-12}$$

where z is the range variable. If the point source is at a very long range, this reduces to

$$F(\bar{\kappa}) = \left[2\frac{J_1(\kappa D/2)}{\kappa D/2}\right]^2 . \tag{B-13}$$

The filter function for an incoherent source of diameter D_s is

$$F(\bar{\kappa}) = \left[2\frac{J_1(\kappa D_s z/2L)}{\kappa D_s z/2L}\right]^2 . \tag{B-14}$$

The filter function for an incoherent source of diameter, D_s, received coherently by a receive aperture of diameter D, is the product of Equations (B-12) and (B-14);

$$F(\bar{\kappa}) = \left[2\frac{J_1(\kappa D(1-z/L)/2)}{\kappa D(1-z/L)/2}\right]^2\left[2\frac{J_1(\kappa D_s z/2L)}{\kappa D_s z/2L}\right]^2 . \tag{B-15}$$

B.2.4 Filter Functions For Focal Anisoplanatism

The filter function for the difference of two waves can be found by integrating the phase over the source and the aperture. The function for focal anisoplanatism with a uniform circular source offset $\bar{b}$ from boresight is

$$F(\bar{\kappa}) = 1 - 2\frac{2J_1(\kappa D_s z/2L)}{\kappa D_s z/2L}\frac{2J_1(\kappa D z/2L)}{\kappa D z/2L}J_0\left(\frac{\kappa b z}{L}\right) + \left[2\frac{J_1(\kappa D_s z/2L)}{\kappa D_s z/2L}\right]^2 . \tag{B-16}$$

The filter function for focal anisoplanatism with a uniform circular source on boresight is

$$F(\vec{\kappa}) = 1 - 2\frac{2J_1(\kappa D_s z/2L)}{\kappa D_s z/2L}\frac{2J_1(\kappa Dz/2L)}{\kappa Dz/2L} + \left[2\frac{J_1(\kappa D_s z/2L)}{\kappa D_s z/2L}\right]^2 . \quad \text{(B-17)}$$

If the source diameter is zero, then one obtains the filter function for focal anisoplanatism with circular symmetry for a point source with no offset

$$F(\vec{\kappa}) = 2\left[1 - 2\frac{J_1(\kappa Dz/2L)}{\kappa Dz/2L}\right] . \quad \text{(B-18)}$$

The filter function used to find the piston or tilt component of focal anisoplanatism with a uniform circular source offset $\vec{b}$ from boresight is

$$F(\vec{\kappa}) = \left|\frac{2\nu J_\nu(\kappa D/2)}{\kappa D/2} - \exp\left[i\vec{\kappa}\cdot\vec{b}\frac{z}{L}\right]\frac{2\nu J_\nu(\kappa D[1-z/L]/2)}{(\kappa D[1-z/L]/2)}\frac{2J_1(\kappa D_s z/2L)}{(\kappa D_s z/2L)}\right|^2 . \quad \text{(B-19)}$$

B.3 ERROR PROPAGATOR FUNCTION FOR SECTION STITCHING

The phase reconstruction process can be described by the matrix product

$$\vec{\phi} = \left\{\left(A^t A\right)^{-1} A\right\}\vec{g} = B\vec{g} , \quad \text{(B-20)}$$

in which $\vec{g}$ is a vector composed the x and y gradient measurements, $\vec{\phi}$ is the phase vector, and A is the matrix is defined as follows:

$$\vec{g} = A\vec{\phi} . \quad \text{(B-21)}$$

If the gradient errors are uncorrelated, the error propagator (defined as the relationship between the gradient error variance and the error variance of the reconstructed phase) is given by

$$\text{Error Propagator} = \frac{1}{N_\phi}\text{Trace}\left[\left(A^t A\right)^{-1}\right] , \quad \text{(B-22)}$$

where N_ϕ is the number of elements in the phase array. The error propagator is approximately unity for a two-dimensional system composed of 100 phase points [16].

The propagation of low spatial-frequency errors due to section-tilt fluctuations in a multiple-beacon system can be viewed as a reconstruction process in which the section tilts are viewed as local gradients having a non-zero correlation. In this case the error propagator function can be generalized in the following way:

$$\text{Error Propagator} = \frac{1}{N_\phi}\text{Trace}\left[\left(A^t C_t^{-1} A\right)^{-1}\right] , \tag{B-23}$$

where C_t is the correlation matrix and the A matrix is designed to produce a full-aperture tilt of zero. The correlation between orthogonal tilts is negligible, but for parallel tilts between sections of diameter, D_s separated by a distance, d, the correlation is [32]

$$C_t(d) = -4.873\cos(2\theta_d)\sum_{n=0}^{\infty}\frac{(-1)^n}{n!}\Gamma\begin{bmatrix} n+\frac{5}{2}, n+\frac{1}{6} \\ n+5, n+3, -n+\frac{11}{6}\end{bmatrix}\left(\frac{D_s}{d}\right)^{2n+1/3}$$

$$+9.746\cos^2(\theta_d)\sum_{n=0}^{\infty}\frac{(-1)^n}{n!}\Gamma\begin{bmatrix} n+\frac{5}{2}, n+\frac{1}{6} \\ n+5, n+3, -n+\frac{5}{6}\end{bmatrix}\left(\frac{D_s}{d}\right)^{2n+1/3} , \tag{B-24}$$

where θ_d is the angle between the tilt vector and the separation vector. This function is independent of the turbulence distribution.

The error propagator has been computed for a square matrix containing 4, 9, 16, and 25 aperture sections, with the results shown in Figure B-1. To a good approximation,

$$\text{Error Propagator} \approx 0.11\left(D/D_s\right)^{5/3} \tag{B-25}$$

over the range studied.

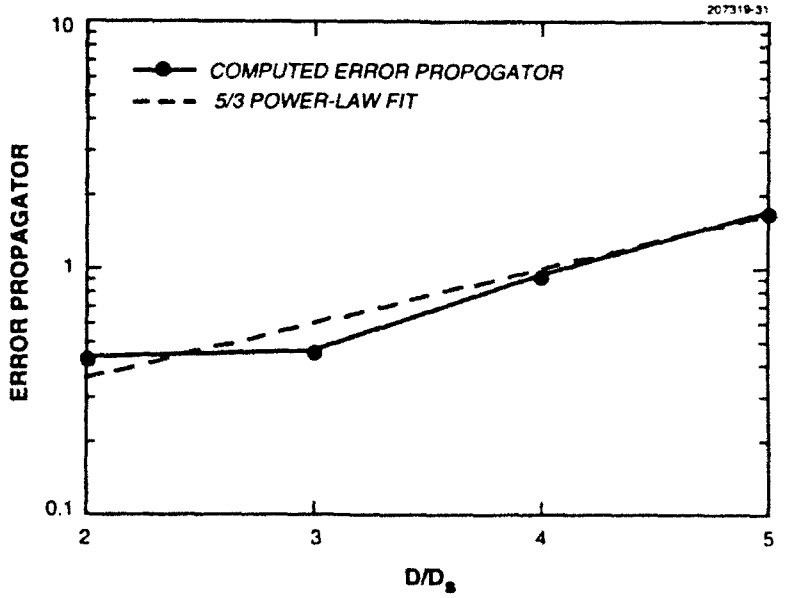

Figure B-1. Error propagator for section-tilts associated with a multiple-beacon system. The computed values can be approximated by the function $0.11(D/D_s)^{5/3}$.

APPENDIX C—RELATIONSHIPS APPLIED IN THE DERIVATION OF SYSTEM PERFORMANCE

C.1 TURBULENCE AND WIND PROFILES FOR PROPAGATION STUDIES

The following two models are frequently used by the laser-beam-control community to describe daytime turbulence conditions:

SLC-Day turbulence model

$$\begin{aligned} C_n^2(h) &= 0 && : 0\text{ m} < h < 19\text{ m} \\ &= 4.008 \times 10^{-13}\, h^{-1.054} && : 19\text{ m} < h < 230\text{ m} \\ &= 1.300 \times 10^{-15} && : 230\text{ m} < h < 850\text{ m} \\ &= 6.352 \times 10^{-7}\, h^{-2.966} && : 850\text{ m} < h < 7{,}000\text{ m} \\ &= 6.209 \times 10^{-16}\, h^{-0.6229} && : 7{,}000\text{ m} < h < 20{,}000\text{ m;} \end{aligned} \tag{C-1}$$

Hufnagel-Valley turbulence model [43]

$$\begin{aligned} C_n^2(h) &= 5.94 \times 10^{-53} (w/27)^2\, h^{10} \exp(-h/1000) + 2.7 \times 10^{-16} \exp(-h/1500) \\ &\quad + A \exp(-h/100) \end{aligned} \tag{C-2}$$

The Hufnagel-Valley model has two free parameters, A and w. The first is normally set to 1.7×10^{-14} $m^{-2/3}$, and the second, which represents the average wind speed, can be adjusted to achieve the desired high-altitude shape. The most common value for w is 21 m/sec, which yields an expression referred to as the HV-21 model.

The temporal characteristics of turbulence usually assumed to follow the form proposed by Bufton [44] are

$$v(h) = v_g + 30 \exp\left\{-\left[(h - 9400)/4800\right]^2\right\} , \tag{C-3}$$

where the ground wind speed parameter, v_g, is usually set to 5 m/sec.

C.2 HARTMANN SENSOR PERFORMANCE EQUATIONS FOR AN *n*-DETECTOR SUBARRAY

A Hartmann sensor having an arbitrarily large linear dynamic range can be constructed by devoting an $n \times n$ matrix of detectors to each subaperture subarray. This strategy is particularly useful for low-repetition-rate compensation systems for which the residual error at each correction cycle is likely to be large. For a fixed dynamic range, the linearity will improve as the number of detectors is increased, but a good trade-off is achieved when the beam diameter is approximately equal to the detector dimension. Under these conditions a phase change of one wave across the subaperture will move the Hartmann spot the length of one detector. Therefore,

$$\text{Linear Dynamic Range} \approx 2\pi(n-1) \quad (\text{rad / subaperture}) . \tag{C-4}$$

The requisite dynamic range for open-loop turbulence correction can be obtained from the phase structure function by replacing the displacement parameter r with the subaperture diameter d_s. From Equation (2-4),

$$D_\phi(d_s) = 6.88\left(d_s / r_0\right)^{5/3} , \tag{C-5}$$

which is approximately one wave for a d_s/r_0 value of unity. To accommodate peak-to-peak fluctuations that might be as much as a factor-of-3 stronger, a full range of order-3 waves would be needed; this requirement could be satisfied with a 4 × 4-element detector array.

Generalizing from Equation (2-16), the gradient expression for an $n \times n$ subarray illuminated by a Hartmann spot matched to the detector dimension is found to be

$$g = 2\pi\sqrt{1+\left(\frac{d_s}{r_0}\right)^2}\,\frac{\sum_{i=1}^{n}\left(i-\frac{n}{2}-\frac{1}{2}\right)\Gamma_i}{\sum_{i=1}^{n}\Gamma_i} \quad \text{(rad / subaperture)} , \tag{C-6}$$

where Γ_i represents the number of photoelectrons collected by the i^{th} pixel. The photon noise near null is identical to that given in Equation (2-17), but the sensor noise expression is

$$\sigma_g^2 \approx \sum_{i=1}^{n}\left(\frac{2\pi(2i-n-1)}{G_e N_{pe}}\sqrt{1+\left(\frac{d_s}{r_0}\right)^2}\right)^2 N_{\text{rms}}^2 , \tag{C-7}$$

where the substitution $N_{pe} = 2\sum_{i=1}^{n}\Gamma_i$ has been made. Applying the identity $\sum_{i=1}^{n}(2i-n-1)^2 = \frac{1}{3}n(n-1)(n+1)$ shows that

$$\sigma_g^2 = \frac{4\pi^2\, n(n-1)(n+1)}{3\left(G_e N_{pe}\right)^2}\left[1+\left(\frac{d_s}{r_0}\right)^2\right]N_{\text{rms}}^2 . \tag{C-8}$$

Combining this result with Equation (2-17) yields the total figure error due to the wavefront sensor;

$$\left(\sigma_{\text{figure}}^2\right)_{\text{noise}} \approx \underbrace{\frac{2\pi^2\left[1+\left(d_s/r_0\right)^2\right]}{N_{pe}}}_{\text{photon noise}} + \underbrace{\frac{4\pi^2\, n(n-1)(n+1)}{3\left(G_e N_{pe}\right)^2}\left[1+\left(\frac{d_s}{r_0}\right)^2\right]N_{\text{rms}}^2}_{\text{sensor noise}} . \tag{C-9}$$

C.3 THE POWER SPECTRUM OF THE FIGURE COMPONENT OF TURBULENCE

A method for computing the phase power spectrum has been described by Greenwood and Fried [21], who derive expressions as a function of aperture position for both tilt-included and tilt-removed cases. The equations are greatly simplified if one uses the tilt-included case, assumes that the phase is measured over a region of zero extent, and allows the point of measurement to lie at the center of a circular aperture. The combination of the first and third of these assumptions yields a result that is essentially equivalent to the tilt-removed case but with a greatly simplified mathematical structure.

The power spectrum developed by Greenwood and Fried is represented by the expression

$$F_\phi(f) = -\frac{1}{2}\int W_\phi(\vec{r},f)\, T_\phi(\vec{r})\, d\vec{r} \quad , \tag{C-10}$$

where $\vec{r}$ is the aperture-position vector and $W_\phi(\vec{r},f)$ is the phase-difference spectrum. For a circular aperture of diameter D,

$$W_\phi(r,f) = 2.079\left(f/f_0\right)^{-8/3} f_0^{-1}\left(D/r_0\right)^{5/3}\sin^2\left(fr/f_0 D\right) \quad , \tag{C-11}$$

where $f_0 = v/\pi D$ represents a characteristic turbulence frequency and v is a wind velocity averaged over the turbulence path

$$v = \left\{\frac{v_{5/3}}{\mu_0}\right\}^{3/5} \quad . \tag{C-12}$$

The transfer function, $T_\phi(\vec{r})$, comprises a set of 5 aperture-overlap integrals that are described in detail in Greenwood and Fried [21]. For the simplifying assumptions outlined above, only two of these integrals are non-zero, which yields the following representation of the figure (tilt-removed) transfer function:

$$T_f(r) = \frac{8}{\pi^2 D^2}\begin{cases}\cos^{-1}(r/D) - (r/D)\left[1-(r/D)^2\right]^{1/2} - \pi & : 0 \le r \le D \\ 0 & : D \le r\end{cases} \quad . \tag{C-13}$$

Equation (C-10) can now be evaluated by combining Equations (C-11) and (C-13) and employing the approximations $\sin^2(x) \approx x^2 - x^4/3$ for small values of $x = fr/f_0 D$ and $\sin^2(x) \approx 1/2$ for x large. The result is an integral over the scalar radius parameter, r, having the form

$$F_\varphi \propto f^{-8/3}\begin{cases}\dfrac{1}{\pi}\displaystyle\int_0^1 r\left(f^2r^2 - \frac{f^4r^4}{3}\right)\left\{\cos^{-1}(r) - r\left[1-r^2\right]^{1/2}\right\}dr - \int_0^{1/2} r\left(f^2r^2 - \frac{f^4r^4}{3}\right)dr & : f \text{ small} \\ \dfrac{1}{\pi}\displaystyle\int_0^1 r\left(\frac{1}{2}\right)\left\{\cos^{-1}(r) - r\left[1-r^2\right]^{1/2}\right\}dr - \int_0^{1/2} r\left(\frac{1}{2}\right)dr & : f \text{ large} \quad .\end{cases} \tag{C-14}$$

which can be solved with the aid of the following set of identities:

$$\int_0^1 r\cos^{-1}(r)dr = \frac{\pi}{8};\int_0^1 r^3\cos^{-1}(r)dr = \frac{3\pi}{64};\int_0^1 r^5\cos^{-1}(r)dr = \frac{5\pi}{192}$$
$$\int_0^1 r^2\left(1-r^2\right)^{1/2}dr = \frac{\pi}{16};\int_0^1 r^4\left(1-r^2\right)^{1/2}dr = \frac{\pi}{32};\int_0^1 r^6\left(1-r^2\right)^{1/2}dr = \frac{5\pi}{16} \qquad \text{(C-15)}$$

The final solution has a relatively simply form in the limit of very low and very high frequencies, and an approximation to the complete function is obtained by joining these two expressions at their point of intersection:

$$F_f(f) = \begin{cases} 0.132\sec(\zeta)k_p^2 D^4 \mu_0^{12/5} v_{5/3}^{-7/5} f^{4/3} & : f \le 0.705 D^{-1}\mu_0^{-3/5} v_{5/3}^{3/5} \\ 0.0326\sec(\zeta)k_p^2 v_{5/3} f^{-8/3} & : f \ge 0.705 D^{-1}\mu_0^{-3/5} v_{5/3}^{3/5} \end{cases} \qquad \text{(C-16)}$$

The units are rad^2 of phase error per Hz, and the integral of this function

$$\int_0^\infty F_f(f)df = 0.06\sec(\zeta)k_p^2 D^{5/3}\mu_0 = 0.14\left(D/r_0\right)^{5/3} \qquad \text{(C-17)}$$

is about 5 percent larger than the expected result for the piston and tilt-removed variance averaged over a circular aperture.

C.4 OPTIMIZATION OF THE SENSOR-NOISE EXPRESSION

The noise expressions for the phase and tracking sensors can usually be written in the form

$$\sigma^2 = ax^m + bx^{-n} \quad , \qquad \text{(C-18)}$$

where x an optimization parameter, and the variables a and b are independent of x. Differentiating with respect to x yields the solution

$$x = \left\{\frac{nb}{ma}\right\}^{(1/m+n)} \quad . \qquad \text{(C-19)}$$

By combining Equations (C-18) and (C-19), the total error for the optimal value of x is computed:

$$\sigma^2 = \left[\left(\frac{n}{m}\right)^{m/m+n} + \left(\frac{n}{m}\right)^{-n/m+n}\right] a^{(n/m+n)} b^{(m/m+n)} \quad . \qquad \text{(C-20)}$$

The relative contributions of the two terms is as follows:

$$\sigma^2 = \left(\frac{n}{m+n}\right)\sigma^2 + \left(\frac{m}{m+n}\right)\sigma^2 \quad . \tag{C-21}$$

Therefore,

$$ax^m = \left(\frac{n}{m+n}\right)\sigma^2 \quad \text{and} \quad bx^{-n} = \left(\frac{m}{m+n}\right)\sigma^2 \tag{C-22}$$

when x has been optimized.

REFERENCES

1. J. Feinleib, AOA Proposal No. 82-P4 (4 March 1982).
2. R. Foy and A. Labeyrie, "Feasibility of Adaptive Telescope with Laser Probe," *Ast. Astrophys* 152, 129–131 (1985).
3. R.A. Humphreys, C.A. Primmerman, L.C. Bradley, and J. Herrmann, "Atmospheric-Turbulence Measurements using a Synthetic Beacon in the Mesospheric Sodium Layer," *Opt. Lett.* 16, 1367–1369 (1991).
4. C.A. Primmerman, D.V. Murphy, D.A. Page, B.G. Zollars, and H.T. Barclay, "Compensation of Atmospheric Optical Distortion using a Synthetic Beacon," *Nature* 353, 141–143 (1991).
5. D.V. Murphy, C.A. Primmerman, D.A. Page, B.G. Zollars, and H.T. Barclay, "Experimental Demonstration of Atmospheric Compensation using Multiple Synthetic Beacons," *Opt. Lett.* 16, 1797–1799 (1991).
6. F. Roddier, M. Northcott, and J. Graves, "A Simple Low-Order Adaptive Optics System for Near-Infrared Applications," *Pub. Astr. Soc. Pac.* 103, 131–149 (1991).
7. A. Kolmogorov, "The Local Structure of Turbulence in Incompressible Viscous Fluid for Very Large Reynolds' Numbers," in *Turbulence, Classic Papers on Statistical Theory*, eds. S.K. Friedlander and L. Topper, Interscience Publishers, 1961, pp. 151–155.
8. D.L. Fried, "Limiting Resolution Looking Down Through the Atmosphere," *J. Opt. Soc. Amer.* 56, 1380–1384 (1966).
9. D.P. Greenwood, "Bandwidth Specification for Adaptive Optics Systems," *J. Opt. Soc. Amer.* 67, 390–393 (1977).
10. F. Roddier, L. Cowie, J.E. Graves, A. Songaila, D. McKenna, V. Vernin, M. Azouit, J.L. Caccia, E. Limburg, C. Roddier, D. Salmon, S. Beland, D. Cowley, and S. Hill, "Seeing at Mauna Kea: a Joint UH-UN-NOAO-CFHT Study," *Proc. SPIE* 1236, 485–491 (1990).
11. J. Hardy, "Active Optics: A New Technology for the Control of Light," *Proc. IEEE* 66, 651–697 (1978).
12. F. Roddier, "Curvature Sensing and Compensation: A New Concept in Adaptive Optics," *Appl. Opt.* 27, 1223–1225 (1988).
13. J.C. Twichell, B.E. Burke, R.K. Reich, W.H. McGonagle, C.M. Huang, M.W. Bautz, J.P. Doty, G.R. Ricker, R.W. Mountain, and V.S. Dolat, "Advanced CCD Imager Technology for use from 1 to 10000 Å," *Rev. Sci. Instrum.* 61, 2744–2746 (1990).
14. H.T. Yura, "Short-Term Average Optical-Beam Spread in a Turbulent Medium," *J. Opt. Soc. Amer.* 63, 567–572 (1973).
15. R.J. Sasiela and J.G. Mooney, "An Optical Phase Reconstructor Based on using a Multiplier-Accumulator Approach," *Proc. SPIE* 551, 170–176 (1985).

16. J. Herrmann, "Least-Squares Wave Front Errors of Minimum Norm," *J. Opt. Soc. Amer.*, 70, 28–35 (1980).

17. J.H. Everson, "New Developments in Deformable Mirror Surface Devices," *Proc. SPIE* 141, Adaptive Optical Components (1978).

18. J.E. Harvey and G.M. Gallahan, "Wavefront Error Compensation Capabilities of Multi-Actuator Deformable Mirrors," *Proc. SPIE* 141, 50–57 (1978).

19. D.P. Greenwood, "Mutual Coherence Function of a Wavefront Corrected by Zonal Adaptive Optics," *J. Opt. Soc. Amer.* 69, 549–553 (1979).

20. A.D. Poularikas and S. Seely, *Signals and Systems*, PSW Publishers, 1985, Chap. 6.

21. D.P. Greenwood and D.L. Fried, "Power Spectra Requirements for Wave-Front-Compensation Systems," *J. Opt. Soc. Amer.* 66, 193–206 (1976).

22. G.A. Tyler, "Bandwidth Considerations for Tracking Through Turbulence," the Optical Sciences Company, Report No. TR-887 (March 1988).

23. L.A. Thompson and C.S. Gardner, "Experiments on Laser Guide Stars at Mauna Kea Observatory for Adaptive Imaging in Astronomy," *Nature* 328, 229–231 (1987).

24. R. Foy and M. Tallon, "ATLAS Experiment to Test the Laser Probe technique for Wavefront Measurements," *Proc. SPIE* 1114, 174–183 (1989).

25. L.A. Thompson and C.S. Gardner, "Excimer Laser Guide Star Techniques for Adaptive Imaging in Astronomy," *Proc. SPIE* 1114, 184–190 (1989).

26. C.S. Gardner, B.M. Welsh, and L.A. Thompson, "Sodium Laser Guide Star Technique for Adaptive Imaging in Astronomy," *Proc. SPIE* 1114, 191–202 (1989).

27. B.M. Welsh, C.S. Gardner, and L.A. Thompson, "Effects of Nonlinear Resonant Absorption on Sodium Laser Guide Stars," *Proc. SPIE* 1114, 203–214 (1989).

28. B.M. Welsh and C.S. Gardner, "Nonlinear Resonant Absorption Effects on the Design of Resonance Fluorescence Lidars and Laser Guide Stars," *Appl. Opt.* 28, 4141–4153 (1989).

29. B.M. Welsh and C.S. Gardner, "Performance Analysis of Adaptive-Optics Systems using Laser Guide Stars and Slope Sensors," *J. Opt. Soc. Amer.* 6, 1913–1923 (1989).

30. C.S. Gardner, B.M. Welsh, and L.A. Thompson, "Design and Performance Analysis of Adaptive Optical Telescopes Using Laser Guide Stars," *Proc. IEEE* 78, 1721–1743 (1990).

31. B.M. Welsh and L.A. Thompson, "Effects of Turbulence-Induced Anisoplanatism on the Imaging Performance of Adaptive-Astronomical Telescopes using Laser Guide Stars," *J. Opt. Soc. Amer. A* 8, 69–80 (1991).

32. R.J. Sasiela, "A Unified Approach to Electromagnetic Wave Propagation in Turbulence and the Evaluation of Multiparameter Integrals," MIT Lincoln Laboratory Technical Report 807 (1 July 1988). AD-A198062.

33. W.L. Wolfe and G.J. Zissis, Eds., *The Infrared Handbook*, (Environmental Research Institute of Michigan, 1985), Chap. 3, pp. 20–22.

34. E.D. Hinkley, ed., *Laser Monitoring of the Atmosphere*, Springer-Verlag, 1976, Chap. 4, p.76.

35. R.M. Measures, *Laser Remote Sensing: Fundamentals and Applications*, John Wiley and Sons, 1984, Chap. 7, p. 241.

36. T.H. Jeys, A.A. Brailove, and A. Mooradian, "Sum Frequency Generation of Sodium Resonance Radiation," *Appl. Opt.* 28, 2588–2591 (1989).

37. V.I. Tatarski, *Wave Propagation in a Turbulent Medium*, McGraw-Hill Book Company, New York (1961), Chap. 7.

38. J.W. Goodman, *Statistical Optics*, John Wiley and Sons, New York (1985), Chap. 8, pp. 415-427.

39. R.J. Hill and S.F. Clifford, "Modified spectrum of atmospheric temperature fluctuations and its application to optical propagation," *J. Opt. Soc. Am.* 68, 892–899 (1978).

40. R. Frehlich, "Laser Scintillation Measurements of the Temperature Spectrum in the Atmospheric Surface Layer," *Journal of the Atmospheric Sciences* (1992).

41. O.I. Marichev, *Integral Transforms of Higher Transcendental Functions*, Ellis Horwood Limited, Chichester, England (1983).

42. R.J. Noll, "Zernike Polynomials and Atmospheric Turbulence," *J. Opt. Soc. Am.* 66, 207–211 (1976).

43. R.E. Hufnagel, "Variations of Atmospheric Turbulence," in *Digest of Technical Papers, Topical Meeting on Optical Propagation Through Turbulence*, Optical Society of America, Washington, DC, July 9–11 (1974).

44. J.L. Bufton, "Comparison of Vertical Profile Turbulence Structure with Stellar Observations," *Appl. Opt.* 12, 1785–1793 (1973).

REPORT DOCUMENTATION PAGE

Form Approved
OMB No. 0704-0188

1. AGENCY USE ONLY (*Leave blank*)	2. REPORT DATE	3. REPORT TYPE AND DATES COVERED
	17 March 1993	Technical Report

4. TITLE AND SUBTITLE

The Application of Synthetic-Beacon Technology to Astronomy

5. FUNDING NUMBERS

C — F19628-90-0002
PE — 63217C, 63221C
PR — 33

6. AUTHOR(S)

Ronald R. Parenti and Richard J. Sasiela

7. PERFORMING ORGANIZATION NAME(S) AND ADDRESS(ES)

Lincoln Laboratory, MIT
P.O. Box 73
Lexington, MA 02173-9108

8. PERFORMING ORGANIZATION REPORT NUMBER

TR-966

9. SPONSORING/MONITORING AGENCY NAME(S) AND ADDRESS(ES)

Air Force Phillips Laboratory
Kirtland AFB, NM 87117-6008

10. SPONSORING/MONITORING AGENCY REPORT NUMBER

ESC-TR-92-132

11. SUPPLEMENTARY NOTES

None

12a. DISTRIBUTION/AVAILABILITY STATEMENT

Approved for public release; distribution is unlimited.

12b. DISTRIBUTION CODE

13. ABSTRACT (*Maximum 200 words*)

The application of adaptive optics technology to laser-beam control has been under investigation within the military community since the early 1970s. This work has encompassed a wide range of theoretical investigations as well as an impressive suite of laboratory and field experiments. During this period a number of real-time systems incorporating several hundred degrees of freedom have been built and tested, and the technology to extend this number by at least an order of magnitude is now under development.

To exploit adaptive-optics concepts in the construction of astronomical telescopes, the budgetary restrictions under which this field of research operates must be considered and improvements in system performance must be carefully balanced against equipment complexity, reliability, and cost. To accomplish this design trade-off, a set of concise analytic models describing the essential properties of a laser guide-star phase-conjugation system has been assembled. With the aid of these models, an optimization strategy for mating adaptive optics to a 4-m-class optical telescope has been developed; research shows that such a system might be expected to improve the effective atmospheric seeing conditions by nearly a factor of 10 within the isoplanatic patch of the turbulence probe.

14. SUBJECT TERMS

astronomy
adaptive optics
atmospheric turbulence
compensated imaging
laser guide star
phase conjugation
synthetic beacon

15. NUMBER OF PAGES
100

16. PRICE CODE

17. SECURITY CLASSIFICATION OF REPORT	18. SECURITY CLASSIFICATION OF THIS PAGE	19. SECURITY CLASSIFICATION OF ABSTRACT	20. LIMITATION OF ABSTRACT
Unclassified	Unclassified	Unclassified	Same as Report